

# **Strength, Deformation and Fracture in Metallic Nanostructures**

Thesis by  
Xun Wendy Gu

In Partial Fulfillment of the Requirements  
for the Degree of  
Doctor of Philosophy



CALIFORNIA INSTITUTE OF TECHNOLOGY

Pasadena, California

2015

(Defended August 14, 2014)

© 2015  
Xun Wendy Gu  
All Rights Reserved

## Acknowledgements

I would like to thank my academic advisor, Professor Julia Greer, for her endless support and boundless enthusiasm. She has been role model, capable supervisor, counselor, and scientific cheerleader rolled into one in the last four years that I have had the pleasure to work with her. I will aspire to be as fearless as Julia in my professional and personal life in the future. I also appreciate the many opportunities to attend conferences and the career counseling Julia has provided.

I am extremely grateful to long time collaborators, Professor Dave Srolovitz, Professor Yong-Wei Zhang, and Dr. Zhaoxuan Wu. Although halfway around the world, these scientists are willing to discuss details of our work on Google+ at all hours of the day and night. They have taught me everything I know about molecular dynamics simulations, and shown by example the value of thinking deeply about scientific problems.

Professors Sossina Haile, Julie Kornfield, Dennis Kochmann, Zhen-Gang Wang, and Guruswami Ravichandran deserve my gratitude for taking the time to be a part of my thesis and/or candidacy committees.

I would like to thank Prof. Dongchan and Carol Garland for TEM training and assistance over the years. Dr. Warren Oliver and Mike Drake from Nanomechanics, Inc. have been instrumental to my progress in graduate school by sharing their considerable expertise in nano-mechanical testing and being incredibly patient when troubleshooting InSEM problems. Thanks to Dr. Matt McDowell and Dr. Betar Gallant for teaching me about batteries. I thank the KNI for providing cleanroom facilities essential to my research, especially KNI staff members Bophan Chhim and Melissa Melendes for above-and-beyond level of help. Thanks to Rachel, David and

Xiaoxing for working closely with me on research projects in the last two years. Thanks to my SURF students Jarvis, Colleen and Alex for their enthusiasm, work ethic and intelligence.

Carissa, thank you for making me laugh, being an unofficial bridesmaid, and having the coolest hair ever. Rachel, Lauren, Viki, Lucas, Robert, Renske, Nick, Andreas, Kat, Bilin, Charlie, the Matts, other Greer group members, members of the RA and CCA programs: thanks for making graduate school fun.

I would like to thank my parents and my sister for showing me their love through actions more than words. My mother-in-law, father-in-law and Randall, are simply put, wonderful people who I know I can always count on in the future.

Lastly, I thank my husband, Jerry Cheung, for being my best friend and for having the biggest heart out of anyone I know. He has been integral to my graduate school experience in countless ways, not least of which were feeding me during crunch time, bearing with terrible jokes about “mass balance”, and believing in me at every turn. It fills me with joy to think of spending the rest of our life together, and I can’t wait to see how the family we are starting turns out.

I would like to acknowledge financial support during my graduate studies from the National Defense Science and Engineering Graduate Fellowship, the National Science Foundation, and the Caltech Innovation Initiative.

## Abstract

An understanding of the mechanics of nanoscale metals and semiconductors is necessary for the safe and prolonged operation of nanostructured devices from transistors to nanowire-based solar cells to miniaturized electrodes. This is a fascinating but challenging pursuit because mechanical properties that are size-invariant in conventional materials, such as strength, ductility and fracture behavior, can depend critically on sample size when materials are reduced to sub-micron dimensions. In this thesis, the effect of nanoscale sample size, microstructure and structural geometry on mechanical strength, deformation and fracture are explored for several classes of solid materials. Nanocrystalline platinum nano-cylinders with diameters of 60 nm to 1  $\mu\text{m}$  and 12 nm sized grains are fabricated and tested in compression. We find that nano-sized metals containing few grains weaken as sample diameter is reduced relative to grain size due to a change from deformation governed by internal grains to surface grain governed deformation. Fracture at the nanoscale is explored by performing *in-situ* SEM tension tests on nanocrystalline platinum and amorphous, metallic glass nano-cylinders containing purposely introduced structural flaws. It is found that failure location, mechanism and strength are determined by the stress concentration with the highest local stress whether this is at the structural flaw or a microstructural feature. Principles of nano-mechanics are used to design and test mechanically robust hierarchical nanostructures with structural and electrochemical applications. 2-photon lithography and electroplating are used to fabricate 3D solid Cu octet meso-lattices with micron-scale features that exhibit strength higher than that of bulk Cu. An *in-situ* SEM lithiation stage is developed and used to simultaneously examine morphological and electrochemical changes in Si-coated Cu meso-lattices that are of interest as high energy capacity electrodes for Li-ion batteries.

# Table of Contents

Acknowledgements .....	iii
Abstract .....	v
Table of Contents .....	vi
List of Figures and Tables .....	viii
Chapter 1. Introduction .....	10
1.1 Mechanics of metals .....	10
1.2 Size effects in metals .....	12
1.3 Outlook for small scale mechanical testing .....	14
1.3 Objectives of this thesis .....	16
Chapter 2. Size Dependent Deformation of Nanocrystalline Platinum Nanostructures .....	19
2.2 Fabrication, characterization and mechanical testing .....	22
2.3 Effect of surface roughness on measured mechanical response .....	25
2.4 Mechanical properties of nanocrystalline Pt nanopillars .....	30
2.5 Molecular dynamics simulations .....	34
2.6 Analysis .....	39
2.7 Summary .....	42
Chapter 3. Mechanisms of Failure in Nanoscale Nanocrystalline Platinum .....	43
3.1 Introduction .....	43
3.2 Fabrication, characterization and mechanical testing .....	45
3.3 Mechanical behavior in tension .....	50
3.5 Finite element modeling .....	51
3.6 Molecular dynamics simulations .....	54
3.7 Summary .....	59
Chapter 4. Mechanisms of Failure in Nanoscale Metallic Glass .....	63
4.1 Introduction .....	63
3.2 Fabrication, characterization and mechanical testing .....	65
4.3 Mechanical behavior in tension .....	68
4.4 Molecular dynamics simulations .....	70
4.5 Stress triaxiality at structural flaw .....	75

	vii
4.6 Summary.....	76
Chapter 5. Strong and Light Architected Cu Meso-lattices .....	78
5.1 Introduction .....	78
5.2 Fabrication and characterization.....	80
5.3 Uniaxial compression .....	84
5.4 Structural vs. material size effects.....	89
5.5 Ni meso-lattices .....	94
5.6 Summary.....	96
Chapter 6. <i>In-situ</i> SEM Lithiation of 3D Architected Si Nano-Electrodes.....	98
6.1 Introduction .....	98
6.2 Fabrication, characterization and electrochemical testing .....	100
6.3 Results.....	103
6.4 Ongoing work.....	105
Bibliography.....	107

## List of Figures and Tables

<b>Figure 2.1:</b> Electroplating setup for fabrication of nanocrystalline Pt nanopillars.....	23
<b>Table 2.1:</b> Electroplating conditions for fabrication of nanocrystalline Pt nanopillars.....	23
<b>Figure 2.2:</b> SEM images of electroplated Pt nanopillars and thin film .....	23
<b>Figure 2.3:</b> Bright field and dark field TEM images of 50 nm wide Pt pillar .....	24
<b>Figure 2.4:</b> SEM images and stress-strain curves showing effect of surface roughness on mechanical behavior of 1 $\mu\text{m}$ sized pillars.....	27
<b>Figure 2.5:</b> SEM images and stress-strain curves showing effect of surface roughness on mechanical behavior of 100 nm sized pillars .....	28
<b>Figure 2.6:</b> Comparison of loading moduli for pillars with and without FIB-polished tops.....	30
<b>Figure 2.7:</b> True stress-strain data for experimentally compressed nanocrystalline Pt nanopillars .....	31
<b>Figure 2.8:</b> SEM images of pre-deformation and post-deformation Pt nanopillars .....	31
<b>Figure 2.9:</b> 0.2% offset yield strengths for nanocrystalline Pt nanopillars .....	33
<b>Figure 2.10:</b> Yield strength of Pt pillars compared against Cu and Ni pillars with few grains .....	33
<b>Figure 2.11:</b> Mechanical behavior of Pt nanocrystalline nanopillars in MD simulations.....	36
<b>Figure 2.12:</b> Snapshots from MD simulation showing pillars at progressively higher strain. ....	38
<b>Figure 2.13:</b> Grain boundary sliding and partial dislocation activity in MD simulations.....	39
<b>Figure 2.14:</b> Schematic showing yield stress in cylindrical sample with few grains. ....	40
<b>Figure 3.1:</b> SEM images of nanocrystalline Pt nanocylinders with intentionally introduced notches...	46
<b>Figure 3.2:</b> Schematic of notch geometries in sidewall of cylindrical samples. ....	47
<b>Figure 3.3:</b> TEM images of notched nanocrystalline Pt nanocylinder.....	49
<b>Figure 3.4:</b> Tensile stress-strain curves and pre- and post-deformation SEM images for nanocrystalline Pt nanocylinders.....	50
<b>Figure 3.5:</b> SEM image of a typical nanocylinder fracture surface. ....	51
<b>Figure 3.6:</b> Simulated finite element nanocylinder with a notch on the side wall.....	52
<b>Figure 3.7:</b> Stress contours at the notch for FEM simulated nc-Pt nanocylinder.....	52
<b>Figure 3.8:</b> Experimentally measured ultimate tensile stress (UTS) versus FEM calculated stress concentration factors for experimental flaw geometries.....	53
<b>Figure 3.9:</b> Stress-strain curves for MD simulation notched nc-Pt samples.....	55
<b>Figure 3.10:</b> Cross-sectional view of tensile stress ( $\sigma_{yy}$ ) at 2.5% applied strain in MD notched nc-Pt samples .....	56
<b>Figure 3.11:</b> Cross-sectional view of intergranular fracture at the notch tip in an MD simulation notched nc-Pt sample .....	58
<b>Figure 4.1:</b> Schematic of templated electroplating of notched Ni-P nanocylinders using a “paused” electroplating method .....	65
<b>Figure 4.2:</b> (A) TEM images of the notched region in a notched Ni-P nanocylinder .....	67
<b>Figure 4.3:</b> SEM images of unnotched and notched Ni-P nanocylinder before and after tensile testing and corresponding mechanical data.....	70
<b>Figure 4.4:</b> Cross-sections of MD simulation unnotched and notched Fe-P nanocylinders showing von Mises stress at varying strains and corresponding stress-strain data.....	73
<b>Figure 4.5:</b> Detailed view of the deformation in an MD simulation notched Fe-P nanocylinder showing activity of atom-scale voids.....	74
<b>Figure 4.6:</b> Evolution of stress triaxiality in a notched Fe-P nanocylinder during tensile testing.....	76

<b>Figure 5.1:</b> Schematic of solid mesostructured lattice fabrication method .....	81
<b>Figure 5.2:</b> SEM images of Cu meso-lattices with octet geometry.....	82
<b>Figure 5.3:</b> TEM images of focus ion beam thinned meso-lattice beam.....	83
<b>Figure 5.4:</b> Ion channeling of FIB milled cross-section of Cu thin film electroplated at identical conditions to the meso-lattices.....	83
<b>Figure 5.5:</b> Stress-strain response from uniaxial compression of meso-lattices with a 6 $\mu\text{m}$ unit cell.	84
<b>Figure 5.6:</b> Loading moduli for Cu meso-lattices as a function of relative density. ....	85
<b>Figure 5.7:</b> Post-deformation SEM images of Cu meso-lattices.....	86
<b>Figure 5.8:</b> Yield strength of meso-lattices as a function of relative density compared against bulk yield strength of Cu thin film .....	87
<b>Figure 5.9:</b> Yield strengths of meso-lattices compared to theoretically predicted yield strengths.....	93
<b>Figure 5.10:</b> SEM images of Ni meso-lattices.....	94
<b>Figure 5.11:</b> TEM images of Ni meso-lattice beam. ....	95
<b>Figure 5.12:</b> Compressive stress-strain response of Ni meso-lattices .....	95
<b>Figure 6.1</b> Schematic and SEM images of Si-Ni meso-lattices .....	101
<b>Figure 6.2</b> <i>in-situ</i> SEM lithiation setup.....	102
<b>Figure 6.3</b> SEM image of Si electrode/ionic liquid electrolyte/Li electrode .....	103
<b>Figure 6.4</b> SEM images of Ni-Si meso-lattice electrode before and after lithiation.....	104
<b>Figure 6.5</b> Cyclic voltammogram of Si thin film versus Li metal in ionic liquid electrolyte .....	104
<b>Figure 6.6</b> SEM images of meso-lattice fabricated using sputtering and PECVD.....	106

# Chapter 1. Introduction

## 1.1 Mechanics of metals

Strength and ductility in metals depends on defects, or irregularities in the arrangement of metal atoms. In crystalline metals, the defects that have the largest influence on mechanical behavior are dislocations and grain boundaries. Dislocations are line defects that can be visualized as an extra half-plane of atoms jammed into an otherwise perfect array of atoms (edge dislocation), or a displacement of all atoms in a plane by half the distance between atoms in the direction of the dislocation such that a helix is formed by atomic planes around the dislocation line (screw dislocation).<sup>1,2</sup> Not only are the atoms at the dislocation line affected by the dislocation, but atoms located near the dislocation are also displaced from their ideal locations by the stress field generated by the dislocation. Plastic deformation in crystalline metals occurs when an applied force is high enough to move dislocations through a plane of close-packed atoms in the metal. The motion of dislocations allows stress to be relieved by local rearrangement of atoms rather than through irreversible breaking of the bonds between atoms as in the case of brittle fracture. The motion of one dislocation can also be impeded by other dislocations in its path with repulsive stress fields. This is the mechanism behind Taylor hardening, a process in which the strength of a metal increases as it is plastically deformed because its dislocations become entangled and require progressively higher stresses to break through the entanglement and move through the metal.<sup>2,3</sup>

Dislocations in metals are active in crystalline domains, grains, which are separated from each other by a disordered region called the grain boundary. Grain boundaries can be characterized as high angle or low angle depending on the degree of misorientation between the adjacent crystalline grains that are separated by the grain boundary, and typically have widths of few atomic lengths.<sup>4</sup> Grain boundaries are sometimes describes as a planar collection of dislocations.<sup>5</sup> As such, the stress field of grain boundaries can repel mobile dislocations within grains, and serve as obstacles to dislocation motion.<sup>2</sup> Thus, grain boundaries strengthen metals by increasing the applied stress required to cause deformation, but can also embrittle metals by limiting dislocation motion and crystal plasticity. Grain boundaries are often assumed to be immobile in dislocation theory, but recent studies show that grain boundary sliding and fracture along grain boundaries can occur in metals with nanoscale grains.<sup>4,6</sup>

Amorphous metallic glass is a class of metal that does not deform through the action of dislocations or grain boundaries. Metallic glasses are made up of two or more types of metal atoms that are spatially arranged such that they do not have long-range translational symmetry.<sup>7</sup> Metallic glasses are not at thermodynamic equilibrium, but instead have kinetically arrested atomic structures that are typically formed by rapid quenching from a molten state. Deformation in metallic glasses is postulated to proceed through action of a shear transformation zone (STZ), in which a cluster of atoms (up to ~100 atoms in size) responds to a shear strain by undergoing an inelastic rearrangement from a configuration at one local energy minimum to a configuration that corresponds to a different local energy minimum.<sup>8,9</sup> The collective action of STZs gives rise to common deformation modes of metallic glasses such as unstable propagation of localized shear bands which can lead to structural failure.<sup>10,11</sup> Metallic glasses tend to have extremely high

strengths, but low fracture toughness relative to many crystalline metallic alloys because of their tendency to fail catastrophically through shear banding.

Metals used for engineering applications require high fracture toughness as well as mechanical strength. Fracture toughness describes the ability of a material to resist the propagation of a crack. Fracture mechanics for metals has its basis in Griffith theory, which describes the conditions required for crack propagation in a brittle solid.<sup>12,13</sup> Griffith theory states that a crack will spontaneously propagate if the energy of the cracked specimen is reduced by increasing the length of the crack. The energy of the specimen is a balance between the surface energy gained when new fracture surfaces are formed, and the loss in elastic or internal energy of the material due to stress relaxation from the growing crack. Griffith theory is not directly applicable to ductile materials such as metals because high stress at the crack tip will induce plastic deformation near this location (within the plastic zone). A correction first described by Irwin uses an effective crack length rather than the actual crack length to account for the plastic zone and the subsequently higher energy required to cause fracture in ductile metals.

## 1.2 Size effects in metals

Perhaps the most well-known size effect in metals is described by the semi-empirical Hall-Petch equation:<sup>14,15</sup>

$$\sigma = \sigma_o + kd^{-0.5} \quad (1.1)$$

where  $\sigma$  is strength,  $\sigma_o$  is the friction stress for dislocation motion for a given material,  $k$  is a material-dependent constant, and  $d$  is grain size. According to this equation, a reduction in grain size leads to an increase in strength in metals. The accepted explanation for this effect is that

plastic flow is more difficult in small grains because of enhanced resistance to dislocation motion due to pile-up at grain boundaries. The Hall-Petch relationship applies to grains larger than 10-25 nm. Below this grain size, grain boundary sliding may govern plastic deformation, and strength is observed to decrease with reduction in grain size (this has been termed the inverse Hall-Petch regime).<sup>4</sup> This intrinsic size effect can be used to control the strength of metals by varying its internal length scale.

An extrinsic size effect also exists in certain classes of metals, in which strength scales with external sample size when sample size is reduced to the micron scale.<sup>16,17</sup> As early as 1956, it was observed that smaller samples were stronger than their larger counterparts in single crystalline Cu, Fe and Ag nanowires with diameters from 1 to 15  $\mu\text{m}$ .<sup>18</sup> Recent advances in fabrication and testing of nano-mechanical samples has led to a new wave of activity exploring the universality of this extrinsic size effect and its mechanistic origins. Nanopillars with cylindrical or square geometries with dimensions from microns to tens of nanometers can now be fabricated through top-down methods such as focused ion beam milling, and through bottom-up processes such as electroplating into a template. These nanopillars can be tested in uniaxial compression and tension to obtain material response in the absence of a large strain gradient and substrate effects.

The mechanical deformation of single crystalline face-centered cubic (fcc) nanopillars has now been extensively studied through uniaxial testing, and the presence of free surfaces in the nanoscale sample is understood to have a dominating effect on mechanical behavior.<sup>17</sup> Single crystalline micro- and nanopillars experience an order of magnitude increase in strength compared to the bulk when sample dimensions are reduced to sub-micron levels, and crystal plasticity within nanopillars occurs by intermittent flow.<sup>19-21</sup> The relation between normalized

shear strength,  $\tau$ , and sample diameter,  $D$ , in single crystalline fcc nanopillars with nonzero initial dislocation density can be described by the following:

$$\frac{\tau}{\mu} = A \left( \frac{D}{b} \right)^m \quad (1.2)$$

where  $\mu$  is the shear modulus,  $b$  is the Burgers vector, and  $A$  and  $m$  are material-dependent constants. The exact value of the scaling constants vary slightly depending on factors such as initial dislocation density, sample fabrication and sample aspect ratio, but  $m$  is generally around -0.6. This size-dependent strengthening is commonly called the “smaller is stronger” size effect. Experimental and computer simulation efforts have established that the sample size effect arises because plasticity in nanopillars does not occur solely through dislocation multiplication and entanglement as is common with bulk metals, but is also carried out via nucleation of dislocations from single-arm sources and free surfaces.<sup>20,22</sup>

### 1.3 Outlook for small scale mechanical testing

Thus far, uniaxial nano-mechanical testing has focused on single crystalline metals. Single crystalline metals are model materials for analysis using dislocation theory because dislocations within single crystalline pillars can only interact with each other and free surfaces, but single crystalline metals lack the microstructural and structural diversity of real engineering materials. Current research directions involve the small scale testing of ever more exotic materials such as shape memory alloys<sup>23</sup>, metallic glasses<sup>24,25</sup>, semiconductors<sup>26</sup> and bone<sup>27</sup> and complex crystal systems such as body-centered cubic (bcc)<sup>28</sup> and hexagonal close packed (hcp).<sup>29</sup> Within the family of crystalline metals, rich mechanical behavior can be expected when internal length scales (e.g. grain boundaries or twin boundaries) are introduced into samples that

exhibit the extrinsic size effect. Experimental exploration of the interplay of these different length scales remains scarce. Another area that deserves attention is fracture toughness at the nanoscale. Small scale testing has focused on mechanical strength, but fracture toughness is possibly more valuable for the prolonged operation of engineering materials. Fracture testing is commonly performed by deforming samples with pre-fabricated notches or cracks and correlating failure strength with crack size and geometry. It is an ongoing challenge to fabricate pre-notched samples at the nanoscale, and to observe the fracture process using available nano-mechanical testing instrumentation.

Knowledge of crystal plasticity and size-dependent mechanical behavior obtained using nano-mechanical testing can be used to improve the mechanics of devices and structural materials formed with nanoscale building blocks. Single crystalline nanopillars could be connected end-to-end in a porous network or embedded in a matrix such that a high ratio of free surface to internal volume is preserved. This would lead to an enhancement of the overall strength of the structure due to the “smaller is stronger” effect in the nanoscale structural components. This strategy has been used to create strong and lightweight porous metallic foams with nanoscale ligaments.<sup>30</sup> The extrinsic size effect has also been used to improve the cycleability of Si nanowire electrodes for Li-ion batteries. These nanowire electrodes have diameters on the order of 100 nm, which causes them to undergo ductile deformation during lithiation and delithiation rather than failing through brittle fracture as is common with macroscale Si electrodes.<sup>31</sup> Traditional material processing strategies can be combined with choice of appropriate external and internal length scales in order to achieve new functionalities and levels of performance.

### 1.3 Objectives of this thesis

This thesis attempts to address several of the open questions in the field of nanomechanics. The first part of this thesis examines the mechanics of crystalline and amorphous nanoscale metals using the nano-cylinder geometry. Chapter 2 describes the fabrication, mechanical properties and deformation mechanisms of polycrystalline, platinum nano-cylinders with 12 nm diameter grains ( $d$ ). The number of grains across the diameter,  $D/d$ , was varied from 5 to 80 by examining samples with  $D$  ranging from 60 nm to 1  $\mu\text{m}$  in size. An abrupt weakening is observed at a small  $D/d$ , while the strengths of large nanopillars are similar to bulk. This “smaller is weaker” trend in few-grained nanopillars is opposite to the “smaller is stronger” size effect in single crystalline nanostructures. Molecular dynamics simulations demonstrate that the size-dependent behavior is associated with the distinct deformation mechanisms operative in interior vs. surface grains.

Chapter 3 explores fracture in nanomaterials using nanocrystalline Pt nanocylinders with pre-fabricated surface notches created using a “paused” electroplating method. *In-situ* scanning electron microscope (SEM) tension tests demonstrate that the majority of these samples failed at the notches, but that tensile failure strength is independent of whether failure occurred at or away from the flaw. Molecular dynamics simulations verify these findings and show that local plasticity is able to reduce the stress concentration ahead of the notch to levels comparable with the strengths of microstructural features (e.g. grain boundaries). Thus, failure occurs at the stress concentration with the highest local stress whether this is at the notch or a microstructural feature. This finding prompts the question: What governs the failure mechanism in a nanoscale sample without microstructural stress concentrations? Chapter 4 reports the fabrication and *in-situ* fracture testing of  $\sim 70$  nm-diameter Ni-P metallic glass samples with a structural flaw, that

are otherwise featureless down to the atomic scale and do not contain any microstructural stress concentrations. Failure occurs at the structural flaw in all cases, and the failure strength of flawed samples was reduced by 40% compared to unflawed samples. Molecular dynamics simulations corroborate sensitivity to flaws in nanoscale metallic glass and reveal that the structural flaw shifts the failure mechanism from shear banding to cavitation. These results show that failure strength and deformation in amorphous nano-solids depend critically on the presence of flaws.

The second part of this thesis, Chapter 5, describes the fabrication and mechanical testing of 3D solid Cu octet meso-lattices with characteristic features on the micron-scale which exhibit size-dependent strengthening. These architected cellular meta-materials were fabricated by a three-step process: (1) direct laser writing of the lattice pattern into a polymer template, (2) electroplating of Cu into the template, and (3) removal of the polymer matrix. The microstructure of the electroplated Cu mainly consists of polycrystalline grains with average diameters of 2  $\mu\text{m}$  such that cross-sections of lattice beams mostly consist of a single grain. Uniaxial compression tests showed that the yield strengths of the open-cell Cu meso-lattices can exceed the yield strength of monolithic bulk Cu: meso-lattices with a relative density of 0.8 had a strength of 332 MPa, which surpassed the bulk yield strength by 80%. This is diametrically opposite to the prediction from structural mechanics theory, which states that strength scales linearly with relative density for the octet structure. We attribute the ability of solid Cu meso-lattices to attain such high strengths to the “smaller is stronger” size effect present in single crystalline metals with sub-micron dimensions. This work demonstrates the use and proliferation of the size-dependent strengthening unique to nanostructures in an architected structural meta-material.

The last part of this thesis, Chapter 6, explores coupled mechanical and electrochemical phenomena in Si meso-lattice electrodes using *in-situ* SEM. Si is of great interest as an anode

material in Li-ion batteries because of its high storage capacity for Li (up to 3600 mAh/g), but suffers from severe mechanical degradation during battery operation. We explore the use of structural topology and the effect of “nano-sizing” electrode features in improving the mechanical and electrochemical properties of Si electrodes. RF magnetron sputtering is used to coat Ni meso-lattices with amorphous Si. An electrochemical cell was built inside of an SEM using a lithium electrode, either a solid Li oxide electrolyte or an ionic liquid electrolyte and the Si meso-lattice electrode. This instrument allowed us to directly observe volume changes, mechanical deformation and failure in the Si anode during lithiation and delithiation.

# Chapter 2. Size Dependent Deformation of Nanocrystalline Platinum Nanostructures

## 2.1 Introduction

The control of material properties through manipulation of microstructural length scales is standard practice amongst material scientists and engineers. Grain refinement generally leads to improved material strength, as described, for example, by the Hall-Petch relation.<sup>14,15</sup> Recently, sample size (an extrinsic length scale) has emerged as another controlling factor in the mechanical behavior of metals when the sample size is reduced to the micron-scale and below.<sup>19,20</sup> Monolithic single crystalline pillars with diameters spanning tens of nanometers to tens of microns have been shown to exhibit an order of magnitude increase in strength over bulk in uniaxial compression and tension testing. This “smaller is stronger” trend has been reported for a wide variety of metals (e.g., Ni, Au, Cu, Mo, W, Nb, V, and Ta) and in samples fabricated by techniques ranging from focused ion beam (FIB) milling of individual pillars to top-down techniques such as electroplating into a template and embossing using a mold.<sup>16,17,19,20,32,33</sup> The deformation mechanisms in these small-scale samples have been demonstrated to fundamentally differ from those in the same metals with macroscopic dimensions because of the influence of free surfaces on dislocation behavior. For example, in fcc single crystalline metals, dislocations are generated by the operation of the so-called single arm dislocation sources in micron-sized structures and via dislocation nucleation at surfaces in nanometer-sized structures.<sup>22,34</sup> Another

unique aspect of small-scale deformation of single crystals is that the stress-strain curves are punctuated by discrete bursts, corresponding to dislocation avalanches.<sup>21</sup>

Most research efforts on small-scale mechanical behavior to date have focused on single crystalline nanopillars; however, some ongoing and recent investigations have focused on the effects of interfaces within nanostructures (grain boundaries, twin boundaries, and bimaterial interfaces) on the mechanical response.<sup>35-43</sup> Understanding the fracture and yield strengths of nanostructures containing multiple grain boundaries as a function of sample dimensions is particularly important for the design of reliable nano- and microelectromechanical (NEMS and MEMS) devices, in which nanometer feature sizes are common constituents of more heterogeneous microstructures. Some studies on the strengths of nanocrystalline fcc nanostructures have been conducted, for example, the effects of size on the deformation of 7-, 30-, and 60-nm grained Ni and Ni-W have been reported.<sup>39,40,44</sup> Jang *et al.* observed a “smaller is weaker” trend in the grain boundary-mediated deformation of an Ni-4%W alloy with grain size  $d=60$  nm and sample dimensions spanning two orders of magnitude.<sup>39</sup> Rinaldi *et al.* observed a marginal increase in the compressive strengths of  $d=30$ nm Ni pillars with increasing pillar diameter,  $D$ , from  $\sim 160$  -272 nm.<sup>40</sup> All of those samples contained 2-40 grains across the nanopillar diameter. It is apparent that a wider range of materials, sample-to-grain size ratios  $D/d$ , and sample geometries should be systematically investigated in order to gain a clear understanding of the transition from the internal length-scale dominated deformation of larger samples to the smaller length-scale regime where intrinsic (microstructure) and extrinsic (sample size) length-scales compete.

Specimens with few grains across the diameter have previously been studied at the macro and the micro scale. It was reported that weakening occurs below a critical sample size to grain

size ratio due to the lower resistance to dislocation activity within grains at free surfaces.<sup>45-48</sup> It is unclear whether this size-induced weakening extends to the nanoscale because dislocations may not be the main carriers of plastic deformation in nano-grained metals.<sup>4,49,50</sup> Bulk nanocrystalline metals with grain sizes below  $\sim 30$  nm have been shown to exhibit reduced strength with decreased grain size.<sup>4</sup> The precise mechanistic source of this so-called inverse Hall-Petch effect is a matter of ongoing discussion. The candidate mechanisms include grain boundary rotation, sliding, migration and the operation of partial dislocations nucleated at grain boundaries.<sup>49-52</sup> The study of nanocrystalline metals of composition and size beyond the most widely studied (Ni, Cu, and Co) will help sort out the origins of this widely observed inverse Hall-Petch regime. Nanostructured Pt is of particular interest because of its wide use in technological devices and catalysis for energy generation and pollution reduction, and is especially suitable for nanomechanical testing because of its minimal oxide formation.<sup>53</sup>

This work was first published in Gu et al., *Nano Letters* (2012).<sup>54</sup> In this work, we explored the effect of external sample size on the deformation of platinum nanopillars of fixed grain size,  $d=12$  nm. The nanopillars contained, on average, 5-80 grains across the 60-1000 nm cylindrical sample diameters. Molecular dynamics simulations were performed by Dr. Zhaoxuan Wu (now at ETH Zurich) in collaboration with Dr. Yong-Wei Zhang and Prof. Dave Srolovitz (now at University of Pennsylvania) from the Institute of High Performance Computing, Singapore, on an overlapping range of sample diameters,  $22 \leq D \leq 64$  nm (i.e.,  $1.5 \leq D/d \leq 5$ ), and for similar height-to-width nanopillar aspect ratios.

## 2.2 Fabrication, characterization and mechanical testing

Nanocrystalline Pt nanopillars with diameters from approx. 60 nm to 1  $\mu\text{m}$  were formed by electroplating into an electron-beam lithography patterned poly(methyl methacrylate) (PMMA) template, fabricated following the methodology of Burek, *et al.*<sup>55</sup> In addition, 1.5  $\mu\text{m}$  thick nanocrystalline Pt films were electroplated onto 100 x 100  $\mu\text{m}^2$  rectangular electrodes formed using a nanometer pattern generator system (FEI Quanta 600F) to create openings in the PMMA layer on an Au-covered silicon wafer. The films were produced for measurement of the yield stress of bulk nanocrystalline Pt with grain sizes identical to that of the nanopillars. The electroplating was performed using a three-electrode electrochemical cell with an Ag/AgCl pseudo-reference electrode, a gold counter electrode, the patterned template as the working electrode and walls made of cured polydimethylsiloxane (see Fig. 2.1a and b).<sup>56</sup> This process was developed specifically for the fabrication of nanocrystalline Pt and is distinct from the commonly used electroplating methodology.<sup>32,55</sup> The electrochemical cell was designed to use only 0.1 mL of the electroplating bath for safety and economy. The Pt electroplating solution consisted of 10 mM chloroplatinic acid (Alfa Aesar) and 0.5 M sulfuric acid (Mallinckrodt Chemicals) in deionized water.<sup>57</sup> Plating process development and optimization revealed that a sawtoothed electrodeposition scheme produced void-free, uniform structures (see Fig. 2.1c and Table 2.1). Voltage is repeatedly increased linearly from the initial to final voltage at a set rate according to the conditions in Table 2.1 until structures of a desired height and geometry are achieved (see Figs. 2.2).

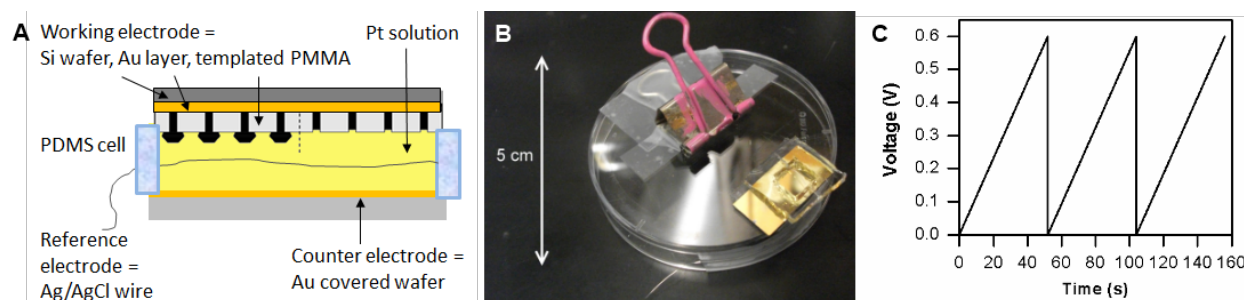


**Figure 2.1:** The electroplating setup employed to deposit the samples: (A) a schematic of the three-electrode electrochemical cell and (B) a photograph of electrochemical cell mounted on a petri dish. (C) Representative electroplating sawtooth voltage-time plot where the voltage is repeatedly cycled from 0 V to 0.6 V.

**Table 2.1:** Electroplating conditions

Diameter/Thickness (nm)	Initial voltage (V)	Final voltage (V)	Ramp rate (mV/s)
$60 \pm 2$	0	0.4	57
$113 \pm 1, 261 \pm 7$	0	0.6	86
$472 \pm 10, 986 \pm 18$ , thin film	0	0.5	36

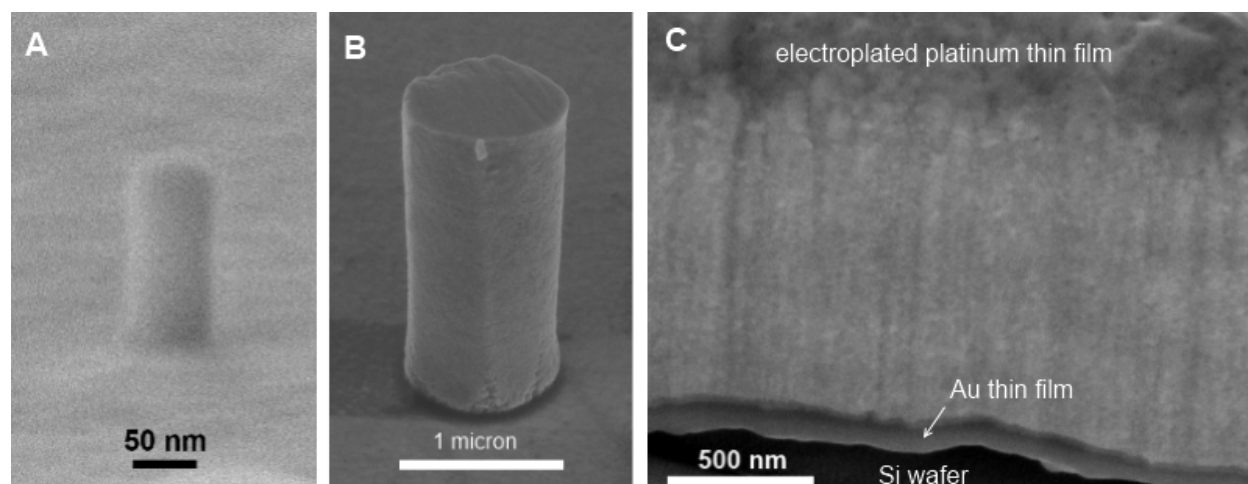


**Figure 2.2:** Electroplated nanocrystalline Pt nanostructures. SEM images of (A) 50 nm wide pillar (image taken at  $86^\circ$  tilt), (B) 1 micron wide pillar with top surface smoothed by FIB ( $52^\circ$  tilt) and (C) a cross-section of a  $1.5 \mu\text{m}$  thick film ( $52^\circ$  tilt).

The microstructure was examined using transmission electron microscopy (TEM) (TF20, FEI Co.) operating at 200 kV, as shown in Figure 2.3. 60 nm thick samples with over-electroplated “heads” were transferred from the growth substrate to a Cu TEM grid by attaching an Omniprobe micromanipulator to the head with electrostatic forces. This TEM sample preparation method did not require additional thinning and avoided exposure to focused ion beam (FIB) and the ensuing radiation damage. The larger diameter pillars (and the underlying silicon) were milled from the substrate using FIB and transferred onto a Cu TEM grid using an Omniprobe micromanipulator to prepare for TEM analysis. Once on the grid, these larger nanopillars were thinned to an electron-transparent thickness (less than 100 nm) using the FIB at the lowest available current setting (10 pA and 30 kV accelerating voltage). The average grain size was identified to be  $12 \pm 4$  nm based on TEM dark field images (Fig. 2.3b). TEM analysis revealed well-formed grains, grain boundaries, and triple-junctions (the lines along which three grains meet).

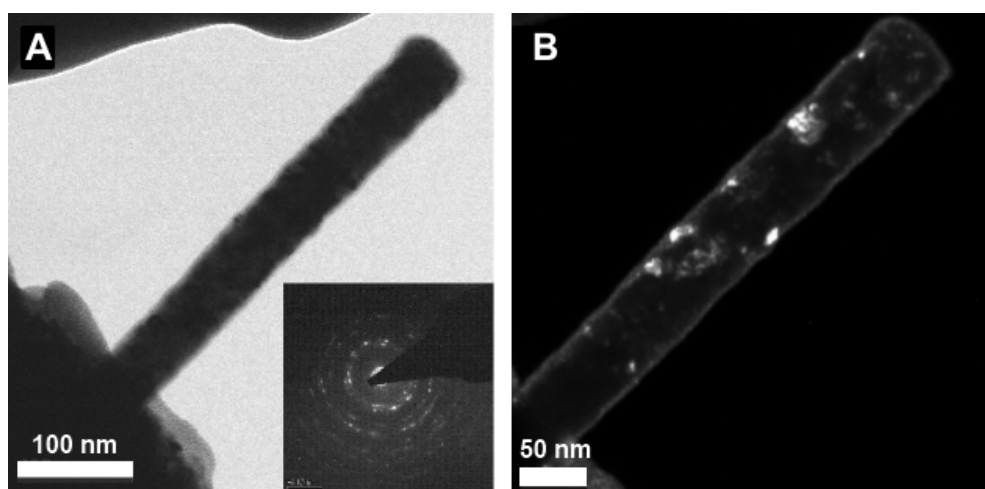


**Figure 2.3.** TEM images of 50 nm wide pillar in (D) bright field with corresponding diffraction pattern as inset, and (E) dark field image used to determine grain sizes.

Uniaxial compression testing of the 60 nm diameter pillars was conducted in the SEMentor, a combined scanning electron microscope (SEM) and nanoindenter (Nanomechanics, Inc.) using a custom-made flat punch tip at a nominal strain rate of 0.001/s. The small pillar required the determination of the precise location of the pillar using SEM in order to assure alignment of the pillar and the nanoindenter tip. All other samples were tested in the G200 nanoindenter (Agilent Technologies). The elastic deformation of the substrate underneath the loaded pillar was accounted for by applying the Sneddon correction<sup>20</sup>. The yield stress of bulk nanocrystalline Pt was obtained from nanoindentation into the electrodeposited nanocrystalline film using a sharp Berkovich tip (G200, Agilent Technologies; Synton-MDP). Seven indents, separated by at least 15  $\mu\text{m}$ , were performed to a depth of  $\sim 150$  nm ( $<10\%$  of the film thickness in order to minimize substrate effects), and at a constant strain rate of 0.001/s.<sup>58</sup> Hardness and modulus were determined based upon the Oliver-Pharr method<sup>58</sup>. The substrate consisted of a 100 nm thick gold film (which served as the conducting seed layer for electroplating) on a silicon wafer. The elastic mismatch between Pt and Au was accounted for by removing the additional compliance of the gold film. This compliance was determined by assuming uniaxial compression of a gold slab with a circular contact area with a radius equivalent to the thickness of the Pt thin film.<sup>59</sup>

### **2.3 Effect of surface roughness on measured mechanical response**

The top surfaces of the 472 and 986 nm diameter nanopillars were gently polished by the ion beam prior to mechanical testing in order to minimize the roughness of the top surface. This was necessary because in the course of this work we discovered that the surface roughness in the

larger diameter nanopillars led to anomalously low stiffnesses which, in turn, could cause an underestimate of the flow stress. One major benefit of micro- and nanopillar compression testing is that the pillar sample geometry lends itself to easy analysis and allows intrinsic material properties to be decoupled from geometric effects such as strain-gradients.<sup>19,20</sup> Geometric imperfections such as taper of the pillar walls and misalignment between pillar and tip must be minimized to create a uniaxial stress state.<sup>60</sup> This work revealed that the morphology of the cylinder top, which makes the initial contact with the indenter tip upon compression, should also be carefully controlled.

We analyzed the stress-strain signatures of pillars whose top surface roughness was systematically varied. Between 5 and 14 measurements were made for each of the data points discussed here. Linear regression was performed on the loading and unloading portions of the stress-strain curves to find the loading and unloading moduli. Pillars with unloading moduli less than 65 GPa were not included because such a low unloading modulus was most likely due to poor alignment between pillar and tip, which resulted in pillar bending rather than compression.

We used FIB to smooth the top surface of the pillar. Figure 2.4a shows an as-electroplated nanopillar with a diameter of approximately 1  $\mu\text{m}$ . The top surface of the nanopillar shows typical fractal-like surface roughness. Figure 2.4b shows a 1  $\mu\text{m}$  sized nanopillar with the top surface gently polished with a low current FIB beam directed perpendicular to the pillar z-axis. The surface of this pillar is much smoother than the pillar in Figure 2.4a (a quantitative determination of surface roughness is difficult to obtain from SEM images or via any other technique that we have attempted). Figure 2.4c shows a set of characteristic stress-strain curves for two representative as-electroplated (rough top) and polished (flat top) 1  $\mu\text{m}$ -diameter pillars. The slope of the elastic loading portion in the stress-strain curve (loading modulus) was 60%

lower for the pillars with rough surfaces. Compressing the as-fabricated samples, therefore, would lead to a 20% underestimation in the plastic flow stresses.

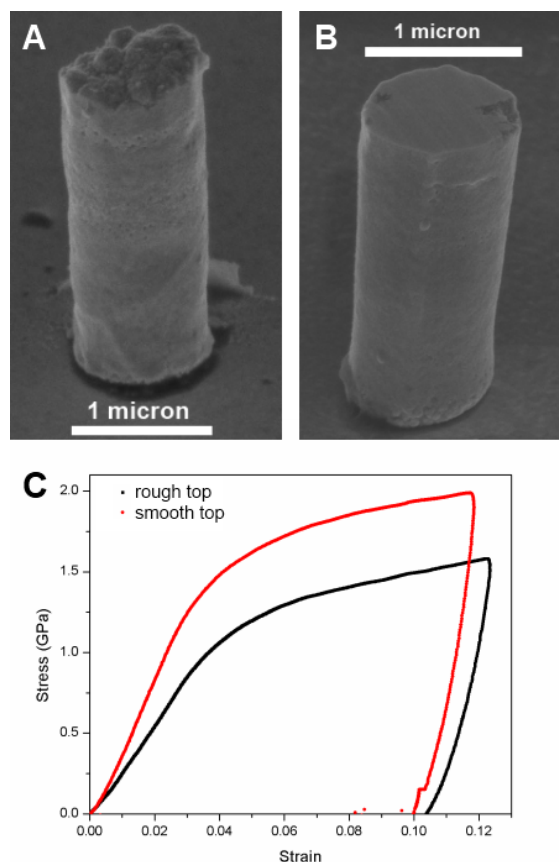


**Figure 2.4:** Effect of surface roughness on mechanical behavior of 1  $\mu\text{m}$  sized pillars. SEM images of (A) a typical as-electroplated pillar (rough top) and (B) a pillar whose top surface was polished with FIB (smooth top). (C) Typical stress-strain data for 1  $\mu\text{m}$  sized samples with rough and smooth tops.

The influence of surface roughness can also be seen in pillars that are approximately 100 nm in diameter, albeit to a smaller degree. Figure 2.5a shows an as-electroplated 100 nm wide nanopillar, which had a naturally smooth and flat pillar top from the growth process. Applying a similar FIB-based methodology to these much smaller samples resulted in the hemispherical rather than flat top shapes because of the preferential milling at the edge of the cylinder (thinner

area) compared to the center of the cylinder (thicker area) (Fig. 2.5b). The stress-strain curves for 100 nm pillar compressions are shown in Figure 2.5c. The loading modulus of the polished pillar was marginally lower than that of the as-fabricated 100nm-diameter pillar. The stress-strain data for both top geometries is characterized by the serrated plastic flow, commonly observed in the deformation of small-scale metals. It is presently unclear why the degree of surface roughness varies with sample size, although we can speculate that the kinetics of the electroplating process changes with the size of the electroplating templates. We observed that the surface roughness increases with the increasing pillar size across the diameters from 100 to 1000 nm.

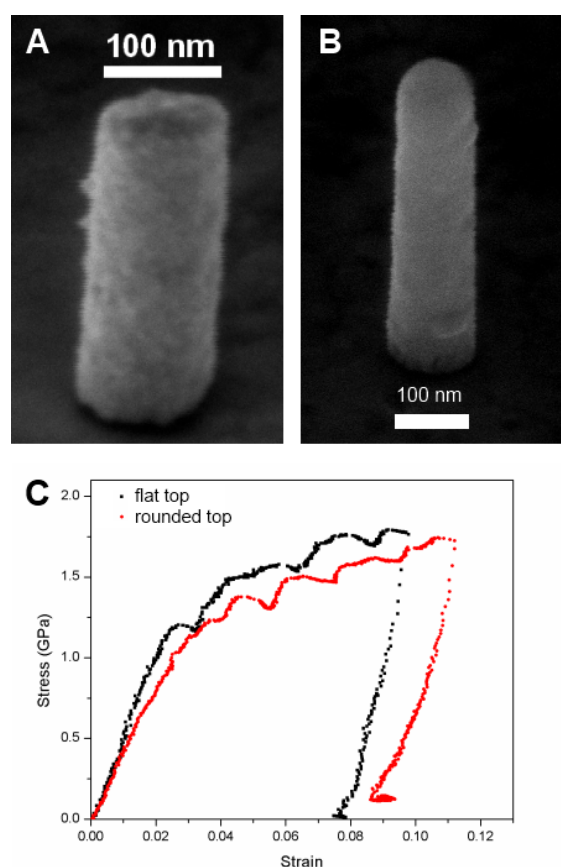


**Figure 2.5:** Effect of surface roughness on mechanical behavior of 100 nm sized pillars. SEM images of (A) a typical as-electroplated pillar with naturally smooth and flat top and (B) a pillar whose top surface was polished with FIB (hemispherical top). (C) Typical stress-strain data for 100 nm sized samples with flat and rounded tops.

The influence of surface roughness is most apparent in the slope of the loading region in the stress-strain curve. The loading slopes were calculated by performing an iterative linear regression process on the initial rise of the stress-strain curves, in which the amount of strain included in the calculation is reduced until the linear correlation coefficient,  $R$ , between the fitted slope and experimental slope is greater than 0.95. A 0.2% offset is added to the maximum strain included in the loading slope calculation in order to define the yield point. The plot in Figure 2.6 compares the loading slopes between the pillars with smoothed tops vs. as-electroplated ones for a range of pillar sizes. Flattened samples with diameters between 500 nm and 1  $\mu\text{m}$  consistently had ~40-50% higher loading slopes than their as-fabricated counterparts of equivalent diameters. 100 nm sized pillars were the only samples, for which the loading modulus decreased by ~ 10% as a result of polishing. These trends can be explained in terms of the contact area between the pillar and indenter tip. The presence of surface roughness in a 1  $\mu\text{m}$ -diameter pillar would lead to a reduced contact area and, hence, a lower apparent stress than in a sample with a flat top. FIB-polishing of the smallest, 100nm-diameter samples generated a smaller contact area because of the high degree of curvature, which led to a lower loading slope. There is a negligible difference in the loading modulus of FIBbed and as-electroplated 250 nm pillars because of the competing and comparable effects of surface roughness from the electroplating growth process and pillar top curvature induced by the polishing process. The greater degree of strain hardening in the non-flat (i.e. rougher and more curved) pillars can be explained by recognizing that the deformation commenced by means of the indenter first coming into contact and flattening the raised parts of the pillar surface into the rest of the sample. Once the raised parts of the pillar surface have been compressed, the rest of the test proceeds as compression of a right cylinder.

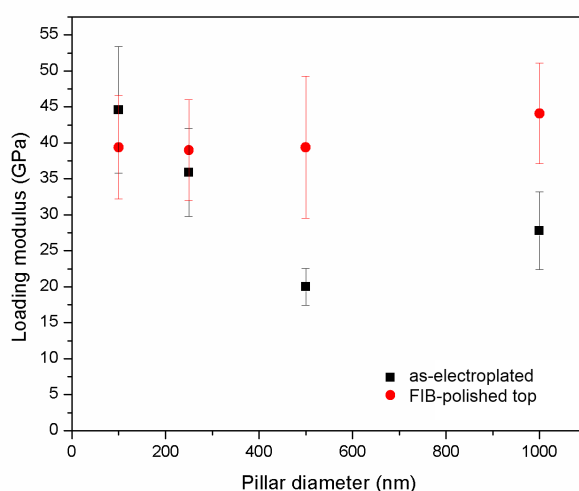


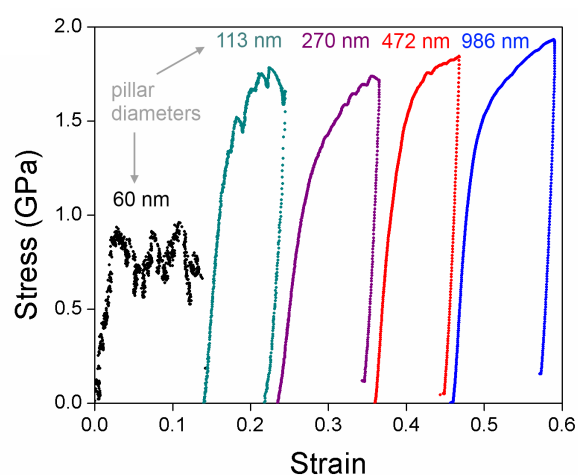
**Figure 2.6:** Comparison of loading moduli for pillars with FIB-polished tops and unFIBbed (as-electroplated) pillars for a range of pillar diameters from 100 nm to 1  $\mu$ m.

This analysis shows that the effect of surface roughness cannot be neglected when performing nanomechanical experiments.<sup>40,41</sup> This is especially important for materials with complex microstructures, where the internal microstructural inhomogeneities may be reflected in the surface roughness, whereas single crystalline nanopillars are more likely to have a smooth crystal plane along the surface of the pillar. Care must be taken when interpreting data obtained during these types of experiments.

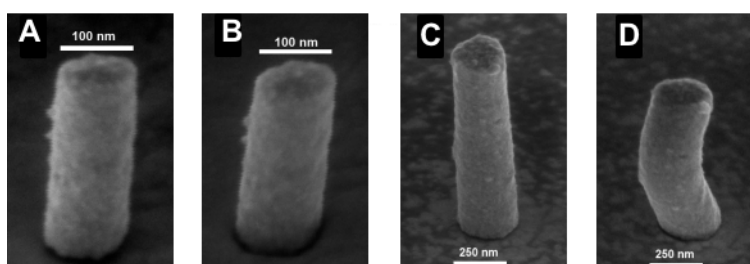
## 2.4 Mechanical properties of nanocrystalline Pt nanopillars

Figure 2.7 shows several representative stress-strain curves for nanopillars with  $60 \leq D \leq 986$  nm. Plastic flow in the  $D=60 \pm 2$  nm and  $113 \pm 1$  nm nanopillars appears as a series of small, convex undulations in the monotonically increasing stress-strain curve envelope. Similar convex segments, albeit with smaller amplitudes, were also observed in the stress-strain curves of the  $D=270 \pm 7$  nm and  $472 \pm 10$  nm nanopillars. Such stochastic, non-smooth behavior

was not visible in the largest diameter ( $986 \pm 18$  nm) samples; the behavior of which closely resembles that of bulk nanocrystalline metals.<sup>61,62</sup> The described stress-strain signatures were consistently reproduced by each of the 6 - 14 samples tested for each diameter. This type of a discrete-to-smooth transition was previously observed in the compressive response of nanocrystalline Ni-4%W nanopillars of similar diameters with 60 nm grains.<sup>39</sup> The pillar morphology remained nearly cylindrical up to compressive strains of 10-15% (Figs. 2.8), after which failure occurred via buckling, similar to that observed by Jahed *et al.*<sup>41</sup>



**Figure 2.7:** Representative true stress-true strain data for experimentally compressed nanocrystalline Pt pillars for range of pillar sizes.



**Figure 2.8:** SEM images of a 113 nm pillar at (A) 0% strain (undeformed) and (B) ~10% strain (plastic deformation); a 270 nm pillar at (C) 0% strain (undeformed) and (D) ~25% strain (plastic bending). SEM images were taken at a 52° tilt.

A dramatic 36% weakening in the 60 nm sized samples was observed, whereas larger samples exhibited flow stresses indistinguishable (within the uncertainty of the measurements) from the bulk. The dependence of strength on nanopillar diameter was quantified by identifying yield from the stress-strain curve using the 0.2% offset method. These yield stresses are plotted in Figure 2.9 as a function of pillar diameter. In all cases, yield occurred before the onset of buckling but after establishing full contact between the pillar and the indenter, as identified by the harmonic continuous stiffness measurement (CSM) for every compression test.<sup>20</sup> The bulk yield strength was obtained via nanoindentation of an electrodeposited nanocrystalline Pt film using

$$H = C \times \sigma_y \quad (2.1)$$

where  $H$  is the measured indentation hardness and  $C$  is the Tabor factor with a value of 3. Bulk yield stress ( $\sigma_y$ ) was determined to be  $1.3 \pm 0.1$  GPa. The yield strength of a Pt thin film with grain size  $d=25$  nm loaded in tension was reported to be  $\sim 1.6$  GPa; i.e., a value 40% higher than the yield strengths measured in this work.<sup>63</sup> The lower strengths of the 12nm-grained samples found in this work as compared with those from the larger-grained Pt films provide further evidence of the inverse Hall-Petch effect and are consistent with reports on similar nanoscale grain sizes in Ni and Cu.<sup>62,64</sup> Figure 2.10 shows the yield strengths, normalized by the measured bulk yield strength, plotted against  $D/d$ . All of the samples other than those with a 60 nm diameter showed normalized strengths within 9% of bulk yield strength. This suggests that a transition from a size-independent to a size-dependent, “smaller is weaker” regime occurs with decreasing  $D/d$ .

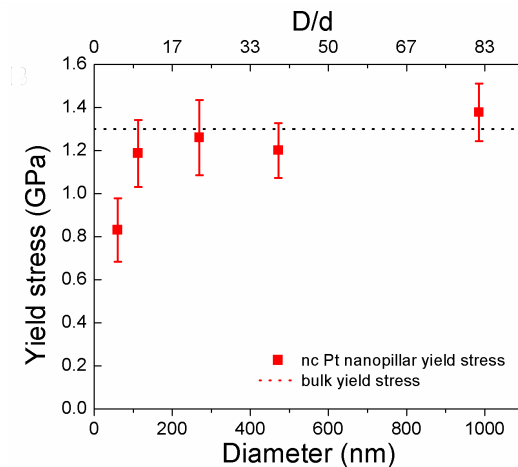


**Figure 2.9:** 0.2% offset yield strengths for experimentally compressed nanocrystalline Pt pillars for a range of pillar sizes.

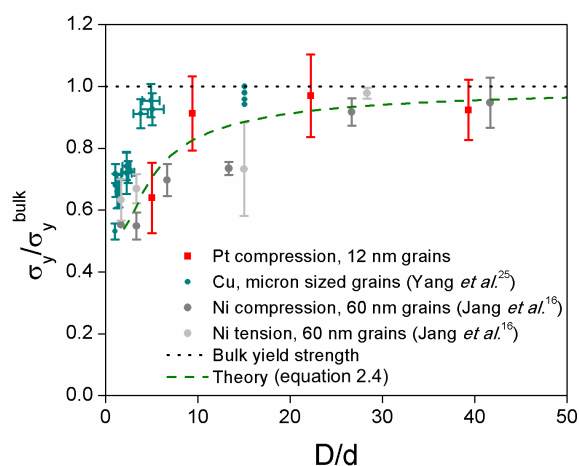


**Figure 2.10:** The yield strength of the Pt pillars as normalized by the bulk nanocrystalline yield strength compared with that for nanocrystalline Ni pillars with 60 nm grains and polycrystalline Cu wires with micron scale grains near the “smaller is weaker” transition. Theoretical yield strength, equation 2.4, is described on page 42.

Figure 2.10 compares the observed size-dependence in nanocrystalline Pt nanopillars to that of nanocrystalline Ni and microcrystalline Cu.<sup>39,48</sup> In all three cases, the yield stress asymptotically approaches the bulk value with increasing  $D/d$  and shows pronounced weakening with decreasing  $D/d$  below some material-dependent value. Nanocrystalline Ni data for  $d=60$  nm showed size dependent weakening at  $D/d$  of 15-30, nanocrystalline Pt with  $d=12$ nm grains

(present work) weakened at  $D/d$  between 5 and 10, and microcrystalline Cu with  $d=2-24$  micron grains weakened at  $D/d$  of  $\sim 2$ . The observed 37% weakening in the strength of nanocrystalline Ni occurred over a  $D/d$  range of about 25, while a similar degree of weakening occurred in nanocrystalline Pt and microcrystalline Cu over a much smaller  $D/d$  range of  $\sim 4$ . This implies that  $D/d$  does not completely define where the transition to “smaller is weaker” occurs; additional factors such as the intrinsic materials properties of the metals and the absolute grain size may play important roles as well. This result agrees well with previous studies of macroscopic polycrystals with few grains, where weakening was observed below  $D/d$  of 3-20 and where both the critical value of  $D/d$  and the weakening rate were functions of the material, grain size and geometry, and sample geometry.<sup>45-47</sup>

## 2.5 Molecular dynamics simulations

A series of molecular dynamics (MD) simulations were performed to gain further insight into the observed compressive behavior of nanocrystalline Pt nanopillars. Simulation samples were constructed by first forming a rectangular prism with dimensions of 64 x 64 x 206 nm, containing 648 grains with an average grain diameter of  $d=14$  nm and random crystallographic orientations. The polycrystalline nanopillar samples were created using the Voronoi procedure on the periodic prism unit cell, as described in Wu *et al.*<sup>65</sup> Two cylindrical nanopillars of diameters  $D = 43$  and 64 nm and lengths of 206 nm were cut from the rectangular prism. Following the same procedure, two smaller cylindrical nanopillars ( $D = 22$  and 32 nm and length of 103 nm) were cut from a shorter rectangular prism (64 x 64 x 103 nm). These nanopillars contained  $\sim 2.5-44$  million atoms and had  $D/d$  between 1.5 and 4.6, with aspect ratios comparable

to those in the experiment. The Pt grain structures in the simulated nanopillars were constructed to mimic those used in the experiments. Microstructural TEM analysis revealed that the experimental Pt nanostructures contained few or no initial dislocations, so dislocations were not introduced into the as-constructed polycrystalline nanopillars used in the simulations.

The MD simulations were performed using the Large-scale Atomic/Molecular Massively Parallel Simulator<sup>66</sup> (LAMMPS) and a Pt embedded atom method (EAM) interatomic potential.<sup>67</sup> Periodic boundary conditions were imposed along the pillar in the axial direction. The simulation samples were equilibrated at 300 K.<sup>68</sup> Subsequently, a uniaxial compressive displacement was applied parallel to the nanopillar axis at the same temperature and at a constant true strain rate of 0.1/ns. The compressive strength of the corresponding bulk nanocrystalline Pt was determined by compressing the rectangular prism (with periodic boundary conditions) in its long axis direction. During compression, constant temperature and zero lateral normal stresses (in the periodic rectangular prism) were maintained using the Nose-Hoover temperature thermo/barostat.<sup>69-72</sup>

The engineering stress-engineering strain curves for the Pt nanopillars from the MD simulations are shown in Figure 2.11a. Figure 2.11b shows the yield stresses normalized by the bulk yield strength as a function of  $D/d$ . These yield stresses were extracted from the stress-strain data at a 1% strain offset (the MD samples were non-linear elastic at 0.2% strain). The yield stresses, normalized by their bulk nanocrystalline counterparts, were 75% ( $D/d = 1.5$ ), 81% ( $D/d = 2.3$ ), 85% ( $D/d=3.1$ ) and 90% ( $D/d=4.6$ ) of the corresponding bulk value. For  $2.3 \leq D/d \leq 4.6$ , a 50% increase in pillar diameter was accompanied by only a 9% increase in the yield strength, indicating that the yield strength became insensitive to  $D/d$  above 5. Oscillations were apparent in the plastic region of the stress-strain curves for  $D/d = 1.5$  and 2.3 samples. Similarly to the experiments, these oscillations became increasingly muted with increasing sample size.

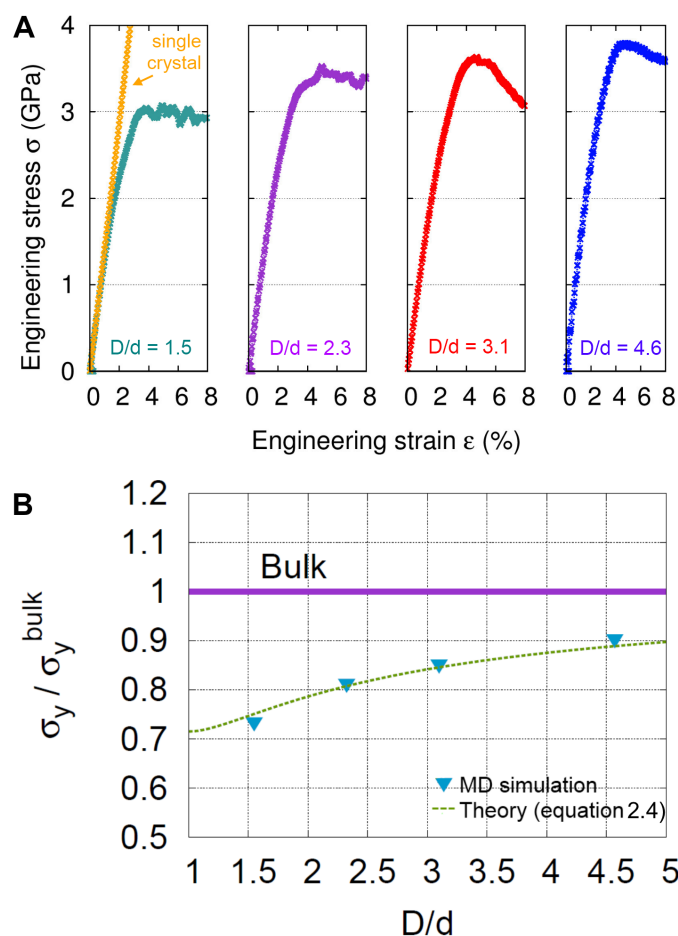


**Figure 2.11:** Yield behavior of Pt nanocrystalline nanopillars with a grain size of 12 nm as determined from the MD simulations. (A) Stress-strain curves and (B) 1% offset yield stress normalized by the bulk nanocrystalline sample yield stress.

These findings show excellent qualitative agreement between experiments and simulations. Quantitatively, however, there are differences. At  $D/d \sim 5$ , the nanopillars in the experiments showed a large and abrupt decrease in yield strength compared with the bulk value, while the nanopillars in the simulations showed a more gradual decrease with decreasing pillar diameter. The difference between the experiment and simulation may be attributed to one or more of the following reasons. First, when the average  $D/d \sim 5$ , the variation in grain size within the experimental polycrystal may result in regions where the local  $D/d$  is significantly less than 5, leading to early yield at these locations. Hence, at small  $D/d$ , the use of an average  $D/d$  may be

insufficient to interpret the yield strength. Second, the quality of artificially constructed grain boundaries in MD simulation may differ from experimental grain boundaries. Electroplated metals may contain a small amount of inorganic impurities from the chemical bath that segregate to grain boundaries and cause embrittlement. MD simulation grain boundaries are only a few atomic lengths wide, and have ideal geometries (straight grain boundaries joined to other grain boundaries at triple junctions) resulting from the Voronoi tessellation used to create the simulations. Experimental grain boundaries may be wider and more disordered. High resolution TEM analysis is needed to experimentally examine the nature of grain boundaries in nanocrystalline Pt nanopillars before comparison with grain boundaries in MD simulation.

Perennial issues with MD simulation include the use of inaccurate interatomic potentials, and strain rate and thermal effects. MD simulations are only as accurate as the interatomic potential used in the simulations, so it is of great importance to develop potentials that are validated using experimental data. The potential used in this study (Ref. 67) has previously proven to accurately reproduce the mechanical properties of Pt. The MD simulations were also performed at a much higher strain rate and a different temperature than used in the experiments, which may shift the balance between the different deformation mechanisms. The use of realistic strain rates and temperatures during MD simulations is unfeasible because these conditions are too computationally expensive. The higher strain rate resulted in a higher flow stress in the simulations as compared with the experiments, but the lower temperature tends to result in lower flow stresses.

Our simulations show that the nanopillars initially underwent non-linear elastic compression, followed by plastic deformation and, subsequently, plastic bending/buckling. Figure 2.12 shows a series of images from the compression of the  $D = 64$  nm nanopillar. The

buckling occurred at a compressive strain of  $\sim 8\%$ , and is clearly visible at 10% and 15%, consistent with the experimental observations (Fig. 2.8).

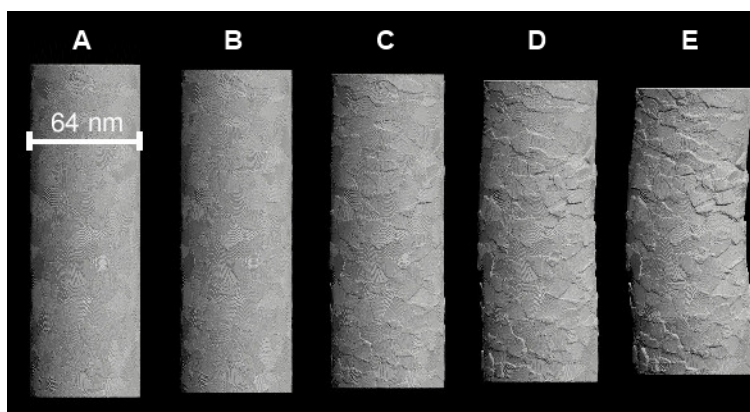


**Figure 2.12:** Snapshots from MD simulation showing the progression from (A) 0% strain (undeformed pillar), (B) 3% strain (elastically deformed), (C) 6% strain (plastically deformed), (D) 10% strain (further plastically deformed) to (E) 15% strain (plastically bending).

Detailed examination of the deformed microstructures revealed that the interior of the nanopillars underwent plastic deformation through dislocation mechanisms. In particular, dislocations were nucleated from grain boundary triple junctions, then rapidly propagated across a grain and absorbed by a grain boundary of the same grain (Fig. 2.13). The deformation behavior in the interior of the nanopillars resembled that observed in the bulk nanocrystalline samples. Near the free surface, however, the deformation was found to be dominated by grain boundary sliding, which led to the formation of small surface steps at some of the grain boundary/free surface intersections. No dislocation activity was seen in these grains up to the plastic yield strain (defined here as 1% plastic strain). The surface steps appeared prior to the nucleation of any dislocations in the nanopillar interior. Previously published models for the “smaller is weaker” transition in macroscopic samples may not be applicable to nanocrystalline materials because they attributed the size effect to differences in dislocation activity in surface and interior grains while dislocation activity in nanocrystalline materials may be limited.<sup>48,73,74</sup>

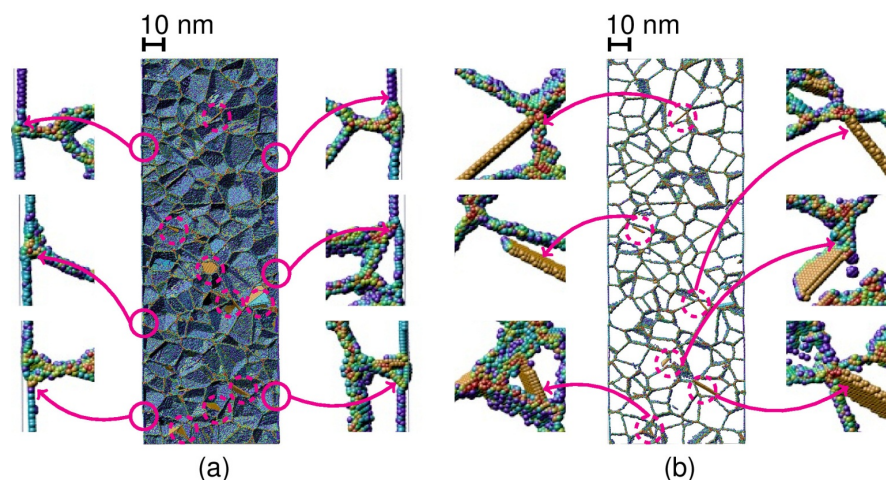


**Figure 2.13:** MD simulation of the nanopillar under compressive loading. (A) shows grain boundary sliding at the surface grains and (B) shows the partial dislocation nucleation at triple junctions and the resulting stacking faults as the partial dislocations propagate through the pillar interior.

## 2.6 Analysis

Direct observation of the detailed deformation mechanism during loading of the Pt nanopillars remains an experimental challenge. Hence, atomistic simulations represent an important tool for deducing the operative deformation mechanism, provided that key observations are shown to be consistent with the experimental data. In the present case, both simulations and experiment show (i) a trend of decreasing strength with decreasing nanocrystalline nanopillar diameter, (ii) the strength asymptotically approaches the bulk nanocrystalline material strength with increasing diameter, and (iii) a trend towards an increasingly oscillatory stress-strain curve with decreasing  $D/d$ . The simulations demonstrate that when the pillar diameter (and  $D/d$ ) was large, only a small fraction of the sample volume deformed via grain boundary sliding (at the boundaries intersecting or near the surface). In this case, the deformation was controlled by the flow properties of the pillar interior and hence the

yield strength of the pillar was similar to that of the bulk nanocrystal. Although the effective flow stress of the grains adjacent to the surface (in this case, flow associated with grain boundary sliding) is lower than those in the pillar interior (dislocation plasticity), the total load carried by the surface region is negligible since the grain diameter is much smaller than the pillar diameter. This also explains why the yield strength approaches its bulk value as the pillar diameter increases with fixed grain size. Since the dominant deformation mechanism near the surface is associated with grain boundary sliding, and the flow stress for grain boundary sliding is lower than that associated with bulk nanocrystal dislocation plasticity, it is expected that the transition between these two regimes is responsible for the emergence of a size effect.

For the simple case where the material is elastic-ideally plastic, we model the pillar as a core region with fractional cross-sectional area  $\frac{A_c}{A}$  and yield stress equal to that of the bulk,  $\sigma_y^{bulk}$ , and a surface region with thickness equal to  $d/2$ , fractional cross-sectional area  $\frac{A_s}{A}$  and yield stress  $\sigma_y^s$  where  $A$  is the total cross-sectional area of the pillar (Fig. 2.14).

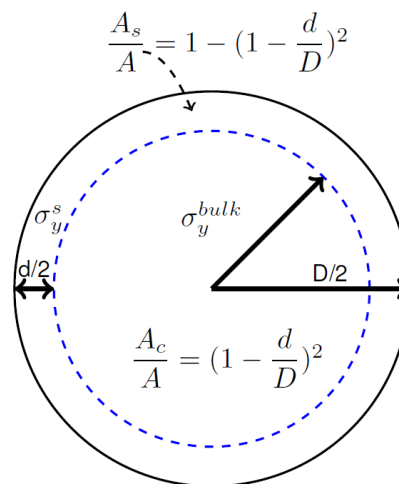


**Figure 2.14:** Schematic illustrating model for yield stress showing cross-section of cylindrical sample.

These quantities can be related to  $d$  and  $D$  in the following derivation for yield stress of the nanocrystalline pillar:

$$\sigma_y = \sigma_y^{\text{bulk}} \frac{A_c}{A} + \sigma_y^s \frac{A_s}{A} \quad (2.2)$$

$$\sigma_y = \sigma_y^{\text{bulk}} \frac{(D-2d)^2}{D^2} + \sigma_y^s \frac{D^2 - (D-2d)^2}{D^2} \quad (2.3)$$

$$\sigma_y = \sigma_y^{\text{bulk}} \left(1 - 2\frac{d}{D}\right)^2 + \sigma_y^s \left[1 - \left(1 - 2\frac{d}{D}\right)^2\right] \quad (2.4)$$

In the limit that the grain size is much smaller than the nanopillar diameter ( $d/D \rightarrow 0$ ), the yield strength tends to the bulk yield strength as  $\sigma_y = \sigma_y^{\text{bulk}} - 2\frac{d}{D}(\sigma_y^{\text{bulk}} - \sigma_y^s)$ . On the other hand, when the nanopillar diameter approaches the grain size,  $r = (D - d) \rightarrow 0$ , the yield strength tends towards the yield strength associated with grain boundary sliding as  $\sigma_y = \sigma_y^s + (\sigma_y^{\text{bulk}} - \sigma_y^s) \frac{r^2}{D^2} \approx \sigma_y^s$  to leading order in  $r/D$ . Nanocrystalline Pt nanopillar experimental and MD simulation data were fitted to Equation 2.3 (see Figs. 2.9 and 2.11a) and the value of  $\sigma_y^s/\sigma_y^{\text{bulk}}$  was found to be 0.54 and 0.72 for experiments and simulations, respectively (plotted on Fig. 2.10). This difference between experiment and simulation results may be due to previously discussed issues such as variability in microstructure and differences in strain rate.

Differing propensities for grain boundary sliding versus partial dislocation nucleation may be responsible for the observed differences in the size-dependence of the yield strength in Pt, Ni and Cu (Fig. 2.10). For example, grain boundary sliding resistance and flow properties of bulk nanocrystalline materials may depend, to different extents, on stacking fault energy. Another possible reason is the difference in the microstructures, for example when  $d$  is smaller than a critical dislocation half-loop radius, dislocation nucleation in the interior can only occur at large applied stresses; this leads to a dependence on the grain size as well as  $D/d$ . Additionally, when the average  $D/d$  is small, the variability in the local grain size (and hence  $D/d$ ) can be large

and yielding will occur by grain boundary sliding along the shortest grain boundary path across the pillar diameter.

## 2.7 Summary

In conclusion, a strong sample size dependence in the plastic response of uniaxially compressed Pt nanopillars with 12 nm sized grains was observed in both experiment and MD simulations. Both experiment and simulation also showed that stochastic, undulating plastic flow was observed for small pillar sizes and continuous, smooth flow at larger pillar sizes. A clear transition to a “smaller is weaker” regime occurred at a  $D/d \sim 5$ , with the smallest pillars 36% weaker in experiment and 10% weaker in MD simulation as compared to bulk nanocrystalline Pt. This transition was found to depend on the absolute grain size and the metal material properties (e.g., stacking fault energy or boundary sliding resistance), as well as the characteristic dimension ratio  $D/d$ . MD simulations revealed that the transition in behavior with nanopillar diameter results from the competition between accommodation of the applied load by grain boundary sliding at surface grains and nucleation and propagation of partial dislocations in the interior grains. Grain boundary sliding occurs at surface grains (and causes surface relief) at applied stresses too low for the nucleation of partial dislocations within the pillar interior. Thus, pillars with small  $D/d$  yield at a lower stress simply because the fraction of grains that is at the surface increases with decreasing  $D/d$ . The present combined experimental and simulation investigation of the mechanical deformation of nanocrystalline Pt nanocylinders provides clear evidence of the role of grain size, materials properties, and sample dimensions in the deformation of metallic nanostructures.

## Chapter 3. Mechanisms of Failure in Nanoscale

### Nanocrystalline Platinum

#### 3.1 Introduction

Hard biomaterials such as shell, bone and exoskeletons have exceedingly high strength and fracture toughness that are on par with the best manmade structural materials.<sup>75,76</sup> These biomaterials have a unifying feature; their internal structures are hierarchically arranged, with distinct features on length scales extending from the nano to the macro. Nanofabrication techniques have advanced to the point where it is now possible to emulate these hierarchical structures, for example using ultra-high strength nanoscale building blocks made of carbon and inorganic nanotubes (1D) and platelets (2D), and metals with nanoscale interfaces (3D) as the load-bearing components.<sup>19,77-81</sup> The high intrinsic strength of these nanomaterials is often difficult to maintain in large-scale composites because a macroscopic ensemble of these structures routinely contains structural and/or chemical features within individual constituents or at the interfaces, which are sources of failure-initiation.<sup>82,83</sup> Classical fracture mechanics dictates that susceptibility to fracture depends on sample and/or external flaw length scales. This implies that different behavior may occur at small sample sizes and that new fracture relations may be necessary to describe failure of nanoscale materials.<sup>13,84</sup>

Several theoretical and computational studies have been performed on fracture in pre-flawed nanoscale samples, often leading to conflicting interpretations. In the theoretical work of Gao *et al.*, scaling arguments based on linear elastic fracture mechanics (LEFM) were used to

define a critical length, 0.2-400 nm for typical brittle materials, below which the strength of a hard platelet becomes comparable to the theoretical strength of the material regardless of the presence of structural flaws.<sup>85</sup> This nanoscale flaw tolerance, or flaw insensitivity, has been proposed as an explanation for the extraordinary toughness found in experiments on nanostructured biomaterials like nacre and spider silk<sup>85,86</sup> and in atomistic simulations of nanocrystalline aluminum thin films and polycrystalline graphene sheets, which showed failure occurring away from the pre-fabricated hole.<sup>87,88</sup> Other studies reported a strong dependence of failure on the presence of flaws – for example, in graphene and carbon nanotubes, where intentionally introduced holes led to strengths that are well below theoretical predictions, but in good agreement with predictions based upon classical fracture mechanics.<sup>89</sup> Even very small holes in a carbon nanotube sidewalls consisting of 1-6 missing atoms were shown to reduce the nanotube strength by 26-33%.<sup>90</sup>

Few well-controlled experimental fracture tests have been attempted at the nanoscale. An *in-situ* TEM study of tensile-loaded nanocrystalline aluminum thin films, which contained FIB milled edge notches with a radius of ~50 nm, showed that failure occurred far from the notch.<sup>91</sup> In other studies, traditional fracture testing methodologies were extended to the micron-scale using FIB milled cantilever coupons (1-10  $\mu\text{m}$  in size) to investigate failure in single and bi-crystalline metals and alloys.<sup>92-94</sup> Results demonstrate that these micron-sized metals fractured as predicted by LEFM, with fracture strength and location controlled by the FIB-milled structural flaw.

These studies prompt several important questions about fracture at the nanoscale, including 1) Does fracture strength depend on the presence of flaws and on sample/flaw geometry? and 2) Can the initiation point of the crack that leads to failure be predicted based

upon the location of the flaw? We address these questions by conducting tensile fracture experiments and MD simulations on similar nano-sized samples with introduced surface flaws of known geometries. In this work, the term “flaw” refers to the external notches only. Nanocrystalline Pt, referred to as nc-Pt hereafter, nanocylinders with surface notches were fabricated through pulsed electroplating into poly-methyl-methacrylate templates and do not suffer from the FIB-induced damage common to many nanomechanical experiments. Typical Pt samples were  $\sim 120$  nm in diameter with an  $\sim 6$  nm grain size. Tensile experiments on unnotched nc-Pt nanocylinders revealed brittle failure; rendering this to be an appropriate material model system for testing fracture mechanics theories that assume limited plasticity. Sizes of surface notches in these nanostructures were of the same order of magnitude as internal microstructural features, i.e., grain size. We examine the competition between such pre-fabricated flaws and intrinsic microstructural features as preferred sites for crack initiation and discuss these findings using concepts from LEFM and atomistic simulations.

Material in this chapter was first published in Gu et al., *Nano Letters* (2013).<sup>95</sup> Molecular dynamics simulations were performed by Dr. Zhaoxuan Wu.

### **3.2 Fabrication, characterization and mechanical testing**

Nanocrystalline platinum cylinders with diameters of  $117 \pm 3$  nm and lengths of  $750 \pm 40$  nm were fabricated with one or more surface flaws using the template-assisted electroplating method described in Chapter 2.2. Nanoscale structural flaws were formed on the outer surface of the cylinder by ramping voltage from 0 V to 0.6 V at 85 mV/s, pausing the electroplating process for approximately five minutes, replacing the electroplating bath, and then applying two more

pulses at the same voltage and plating rate. Applying three electroplating pulses was appropriate for filling the PMMA pore, and forming a hemispherical “head” above the PMMA layer that can subsequently be used as a grip during tension testing. We postulate that this fabrication technique leads to surface flaws because the first electroplating pulse leads to the formation of a columnar cylinder with several grains exposed on the top surface of the cylinder. The second set of pulses leads to the nucleation of new grains at some but not all of the exposed grains on the top surface of some of the cylinders. The flaw is formed where nucleation fails to occur between sets of electroplating pulses.

The surface flaws had the shape of a rounded notch with circumferential length,  $b$ , and height,  $h$  (See Fig. 3.1a and b, and an unflawed nano-cylinder for comparison in Fig. 3.1c). The

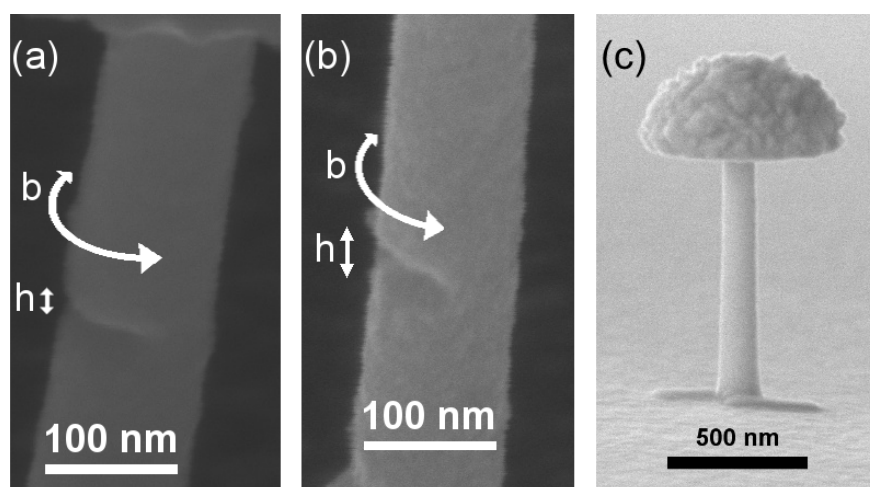


**Figure 3.1:** Nanocrystalline nanocylinders with intentionally introduced notches. SEM images taken from a  $52^\circ$  tilt of (a) a notch with circumferential length  $b = 84$  nm, and height  $h = 47$  nm ( $\bar{b} = 0.23$  and  $\bar{h} = 0.06$  when normalized by sample dimensions), and (b) a notch of  $b = 161$  nm and  $h = 24$  nm ( $\bar{b} = 0.54$  and  $\bar{h} = 0.03$ ). (c) SEM image of an unflawed cylinder.

geometry of each cylinder and its surface flaws was characterized thoroughly using SEM at a  $52^\circ$  tilt at  $0^\circ$  (in order to image the front face of the cylinder) and  $180^\circ$  (back face) rotation, and at  $86^\circ$  tilt at  $0^\circ$  rotation (front face). The notch depth,  $a$ , and radius,  $r$ , were estimated using this

method, but could not be determined precisely because SEM imaging cannot be performed at the necessary angles relative to the notch for complete characterization of  $a$  and  $r$ .

Notch geometries were grouped into two categories: (1) a straight notch or (2) a partial circumferential notch based on SEM images, with  $r$  equal to half of  $h$  (Fig. 3.2). Notch geometry was described in terms of the fraction of cylinder circumference,  $\bar{b} = \frac{b}{\pi D}$ , and fraction of the cylinder height,  $\bar{h} = \frac{h}{l}$ . Resulting unitless dimensions were  $\bar{b}=0.10-0.50$  (circumferential length of  $b=40-200$  nm) and  $\bar{h}=0.02-0.07$  (notch height  $h=15-50$  nm).

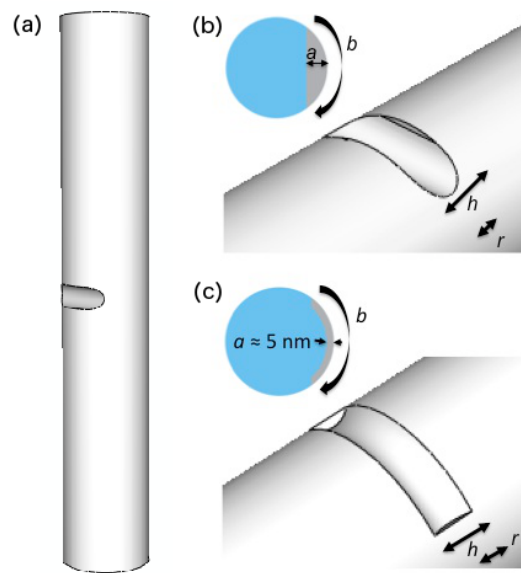


**Figure 3.2:** (a) Schematic of a cylinder with a rounded notch in the sidewall similar to those in electroplated nc-Pt samples. The experimental notches can be classified as (b) straight notch with a rounded tip that crosses the width of the cylinder (geometry A) and (c) a partial circumferential notch with a rounded tip (geometry B). Notches of both geometries are characterized using circumferential length  $b$ , crack height  $h$ , and notch radius  $r$ , where  $r$  is assumed to be equal to  $h/2$ . Notch depth,  $a$ , depends on  $b$  in geometry A, and is  $\sim 5$  nm in geometry B based on SEM observations.

Size and shape of nanoscale samples and flaws play an important role in failure processes, hence to compare fracture properties in a nanomaterial with those with macroscopic dimensions, it would be wise to follow a standard for nanomechanical testing. Existing American

Society for Testing and Materials (ASTM) fracture standards are designed for large samples and no standard exists for nanoscale samples.<sup>96</sup> This work serves as a step towards establishing this standard because it sheds light on fundamental physics of fracture mechanisms in nanomaterials in the presence of notches, which play a key role in failure of macroscopic samples. The sample geometry in this work is appropriate for nano-fracture testing because the surface flaws represent a major stress concentrator at which failure initiation would be expected in a typical macroscopic sample. The nc-Pt samples failed at ~3% strain and approximately 1% plastic strain with no observable bending at the flaw.

Sample preparation for TEM was performed by “plucking” a tension sample with the InSEM (Nanomechanics, Inc.), an *in-situ* SEM with an attached nanoindenter.<sup>43</sup> To do this, the tension sample was fed into a custom-milled tungsten tension grip used as the nanoindenter tip, which is used to lift the sample off the growth substrate. The grips were in contact with the sample on the underside of the tension head. The sample was then gently lowered onto a TEM grid using the tension grips, and then the tension grip was detached from the tension head. Carbon is applied to the base of the sample using e-beam deposition in order to glue the sample to the TEM grid. Transmission electron microscopy (TEM) revealed the grain size to be  $6 \pm 3$  nm with no significant variation across sample volumes (Fig. 3.3).

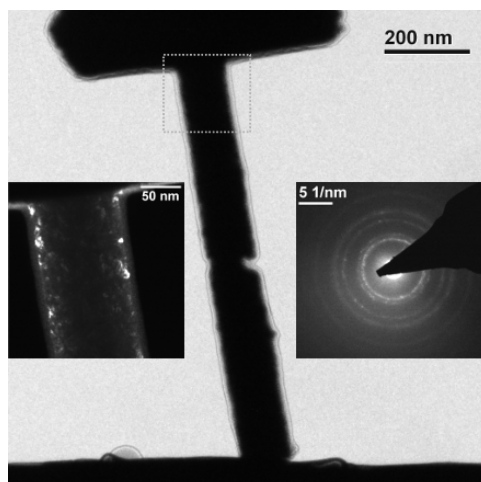


**Figure 3.3:** Bright-field TEM image of plucked cylinder, with boxed region represented in the dark-field image inset which shows nanocrystalline microstructure. The other inset shows the corresponding diffraction pattern.

Tension tests were performed in the InSEM using a custom-milled diamond tension grip.<sup>28</sup> Electroplated Pt cylinders show poor adhesion to the underlying Au substrate, so a small amount of W glue was applied to the base of the cylinder using the FEI Nova 200 dual beam system. Tension tests were conducted at a constant strain rate of  $0.01 \text{ s}^{-1}$ . SEM video was taken during tension testing, and instrument compliances and changes in sample dimensions and fracture locations were determined from the video. Measured load-displacement data was converted to true stress-strain curves, after accounting for instrument compliance. During *in-situ* SEM mechanical tests the samples were oriented such that the surface flaw was on the side, rather than the front or back faces, of the sample relative to the imaging electron beam in order to observe the initiation of failure.

### 3.3 Mechanical behavior in tension

We found that 8 of 12 samples broke at the surface flaw and the remaining 4 broke away from the flaw. Stress-strain data for each experiment suggested brittle failure, with limited plastic deformation and no noticeable necking (Fig. 3.4). The data showed no significant difference in ultimate tensile strengths (UTS) of samples that broke at the flaw (UTS of  $1.8 \pm 0.1$  GPa), ones that broke away from the flaw (UTS of  $1.8 \pm 0.2$  GPa), and the unnotched samples. This strength

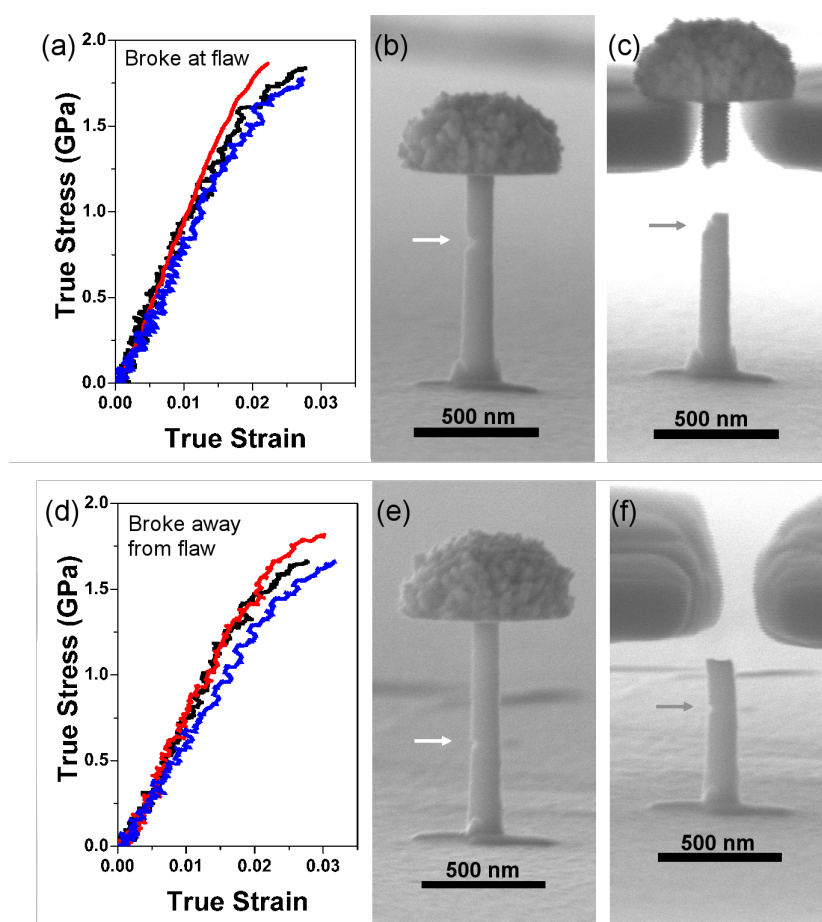


**Figure 3.4:** Samples that broke at the flaw: (a) representative true stress-true strain plots from uniaxial tension tests, (b) SEM image of a pre-flawed sample, and (c) SEM image of the same sample after fracturing at the flaw. Samples that broke away from the flaw: (d) representative true stress-true strain plots from uniaxial tensile tests, (e) SEM image of a pre-flawed sample, and (f) SEM image of the same sample after fracturing away from the flaw.

is 50% higher than that of similarly-fabricated Pt nanopillars tested in compression, which is likely due to the higher deformation strain rate ( $0.001 \text{ s}^{-1}$  for compression vs.  $0.01 \text{ s}^{-1}$  here) and the tension-compression asymmetry common to nanocrystalline metals.<sup>39,54</sup> Sample size-dependent weakening appears in nanocrystalline Pt nanostructure when the sample size to grain size ratio,  $D/d$ , falls below  $\sim 5$ .<sup>54</sup> Samples in this study have  $D/d$  of  $\sim 20$ ; hence, the measured strengths are independent of sample size.

SEM images revealed features with dimensions on the order of grain size that populated the fracture surfaces, reminiscent of typical dimpled fracture morphology of bulk nanocrystalline metals (3.5).<sup>6,61</sup> This suggests the occurrence of localized plasticity despite no evidence of global necking. The angle between the fracture surface relative to the loading axis and the curvature of the fracture surface across the width of the broken cylinder varied among the samples.

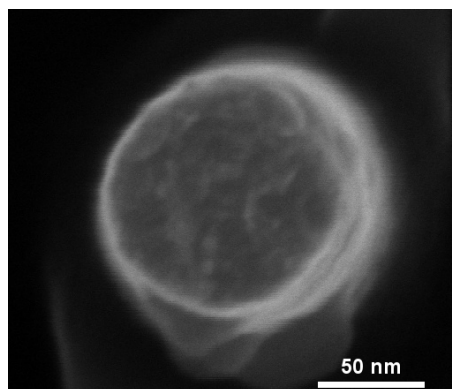


**Figure 3.5:** SEM image of a typical nanocylinder fracture surface.

### 3.5 Finite element modeling

The finding that 2/3 of the samples broke at the notch suggests sensitivity of failure initiation to flaws. Both sets of cylinders – ones that failed at the flaw and those that failed away from it – exhibited nearly identical fracture strengths, which implies flaw-insensitivity in

strength. To resolve this apparent contradiction, we performed finite element modeling of Pt samples with notch and sample geometries similar to those in the experiments in order to evaluate whether failure location and strength correlate with stress concentration at the notch as predicted by classical fracture mechanics. Finite element modeling (FEM) was performed using the ABAQUS/CAE software package in order to calculate the stress concentration at the notch on a cylinder. The sample was modeled as a linear elastic, isotropic, homogenous three-dimensional cylinder with the materials properties of platinum ( $E = 172$  GPa,  $\nu = 0.4$ ) (Fig. 3.6).

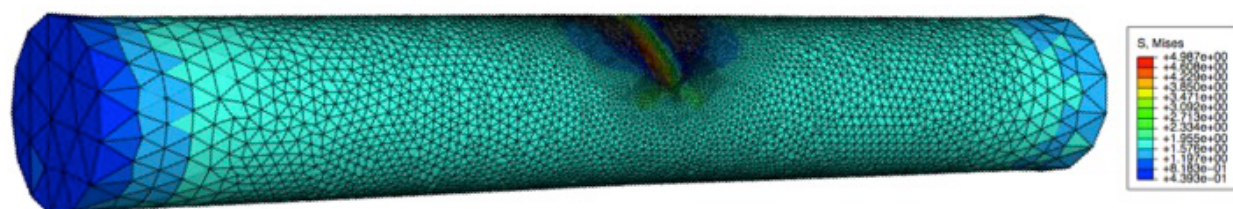


**Figure 3.6:** Simulated finite element nanocylinder with a notch on the side wall.

Eleven of the twelve experimental samples were modeled using ABAQUS, with notch dimensions consistent with SEM measurements (notch dimensions were not available for the remaining sample). FEM notches were modeled as geometry A, straight notch, or geometry B, partial circumferential notch, because precise information about notch depth and sharpness was not available (Fig. 3.7).

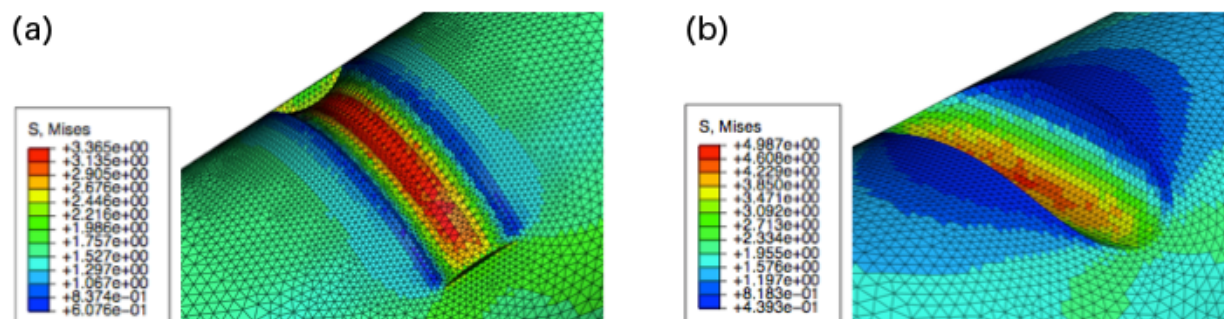


**Figure 3.7:** Stress contours at the notch for FEM simulated nc-Pt nanocylinders with (a) a partial circumferential notch (geometry A) and (b) a straight notch (geometry B).

The FEM sample was statically loaded, with a surface traction applied to one cylindrical base of the cylinder such that the sample was pulled in tension in the z-direction. The sample was fixed in the plane of this cylinder face (to model the constraint imposed by the tension grip). The other cylindrical base was fixed in all three dimensions to model a nc-Pt sample fixed to the substrate. A mesh with 192023 to 463638 tetragonal elements was generated, with the majority of elements concentrated at the notch. The mesh was refined such that the stress values converged to within 7%.

The von Mises stress was calculated at the notch because of the multiaxial stress state present at this location, and used to find the stress concentration at the notch. The stress concentration at the notch for each sample was plotted against ultimate tensile strength (UTS) in Figure 3.8. Figure 3.8 shows that samples that broke at the notch had higher stress concentrations at the notch than samples that broke away from the notch for all but one sample, and the distribution in UTS for these two types of failure.

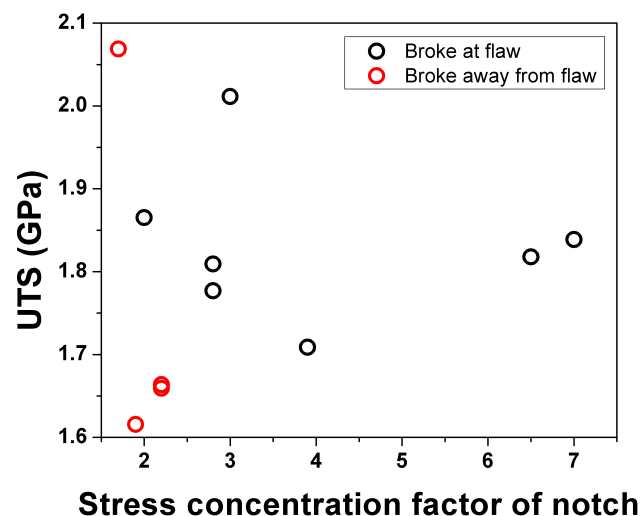


**Figure 3.8:** Experimentally measured ultimate tensile stress (UTS) versus stress concentration factor for each flaw geometry. Fracture occurs away from the flaw only at relatively small stress concentrations.

The calculations showed that the stress concentrations at the notches in the cylinders that broke at the notch to be higher than those for notched samples that broke elsewhere for all but one sample. This indicates that structural stress concentrations at the nanoscale behave as predicted by scale-free continuum theory. FEM simulations also revealed that elasticity-based structural stress concentrations were not correlated with the experimental UTS. We postulate that failure strength may instead be governed by microstructural stress concentrations, which cannot be captured in finite element simulations.

### 3.6 Molecular dynamics simulations

We performed molecular dynamics simulations of nc-Pt samples with notch and sample geometries similar to those in the experiments to reveal the microstructural, mechanistic origin of the experimentally observed deformation and failure. A notch-free nanocylinder (Fig. 3.9a) was created, and used as the starting structure for four nanocylinder samples with notches of very different geometries. Details of the construction of MD samples were provided in Chapter 2.5. Two samples had rounded notches ( $\bar{b} = 0.16$  and  $\bar{h} = 0.03$ , Fig. 3.9b;  $\bar{b} = 0.2$  and  $\bar{h} = 0.03$ , Fig. 3.9c) and two samples contained sharp notches ( $\bar{b} = 0.23$  and  $\bar{h} = 0.006$ , Fig. 3.9d;  $\bar{b} = 0.33$  and  $\bar{h} = 0.006$ , Fig. 3.9e). Following equilibration at room temperature, the nanocylinders were uniaxially stretched to failure.<sup>68</sup> Before creating the notch, we first identified the fracture location in the notch-free nanocylinder, and always placed the notches far away from this location.

Figure 3.9 shows the stress-strain data for all five nanocylinders (a-e), and post-deformation samples that break away from (3f) and at (3g) the notch. Simulations revealed that the samples shown in Fig. 3.9b and d broke away from the notch, in contrast to those in Fig. 3.9c

and e, which failed at the notch. Regardless of the location of failure initiation, all stress-strain curves were remarkably similar, reaching a UTS of  $\sim 3$  GPa, and then undergoing rapid strain softening even in the most extreme case in which the notch extended 1/3 of the way across the sample diameter (Fig. 3.9e). The nearly identical UTS in all five samples demonstrates that the UTS was insensitive to the presence of notches and the occurrence of failure both at and away from the notches suggests sensitivity of failure initiation to flaws, which corroborates the experiments.

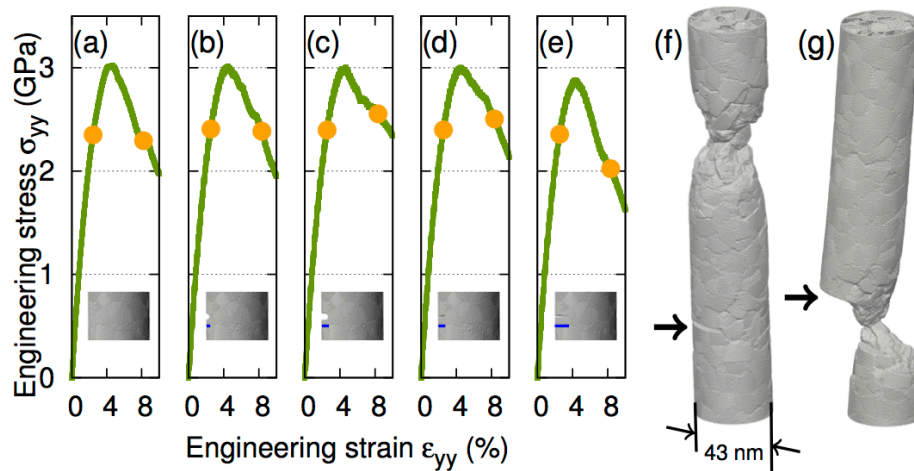


**Figure 3.9:** The stress-strain curves of five simulation samples for (a) notch-free, and notched samples with notch geometry with normalized circumferential width and height (b)  $\bar{b} = 0.16$  and  $\bar{h} = 0.03$  ( $b = 21$  nm and  $h = 5$  nm), (c)  $\bar{b} = 0.2$  and  $\bar{h} = 0.03$  ( $b = 30$  nm and  $h = 5$  nm), (d)  $\bar{b} = 0.23$  and  $\bar{h} = 0.006$  ( $b = 31$  nm and  $h = 1$  nm), and (e)  $\bar{b} = 0.33$  and  $\bar{h} = 0.006$  ( $b = 44$  nm and  $h = 1$  nm). In the stress-strain curves, the orange circles mark the 2.5% and 8% strains at which the atomic stresses in Fig. 2 were measured. The insets in (a-e) show magnified views near the notches and the blue lines indicate the notch depths. (f-g) show examples of pillar fracture away from the notch ( $\bar{b} = 0.23$ ;  $\bar{h} = 0.006$ ) and at the notch ( $\bar{b} = 0.33$  and  $\bar{h} = 0.006$ ), respectively.

These experimental and computational results present compelling evidence that the effects of flaws on deformation and failure of nanomaterials are significantly different from those in their coarse-grained and macroscopic counterparts. To gain further insight into what makes failure of nanomaterials different in response to external notches, we examined these processes at the atomic level. The atomic stresses were calculated based on the atomic *virial* stress in which the atomic

volume was set to the Voronoi volume associated with each atom. Figure 3.10 shows the spatial distribution of atomic-level (virial) tensile stresses ( $\sigma_{yy}$ ) near a rounded notch ( $\bar{b} = 0.2$  and  $\bar{h} = 0.03$ ) and near a sharp notch ( $\bar{b} = 0.23$  and  $\bar{h} = 0.006$ ) at a 2.5% applied strain. The stress distribution near both types of notches showed the presence of a strong stress concentration at the tip of the notch which is  $\sim 5$  times the average stress (Fig. 3.10a2-b2), and is sufficiently large to trigger highly localized plasticity at the notch. Partial dislocations were nucleated at the rounded notch root and propagated across the grain, leaving stacking faults in their wake (Fig. 3.10a3). Grain boundary sliding occurred in response to the local stress at the sharper notch, which led to surface offsets where grain boundaries intersected the outer surface (Fig. 3.10b3). The combination

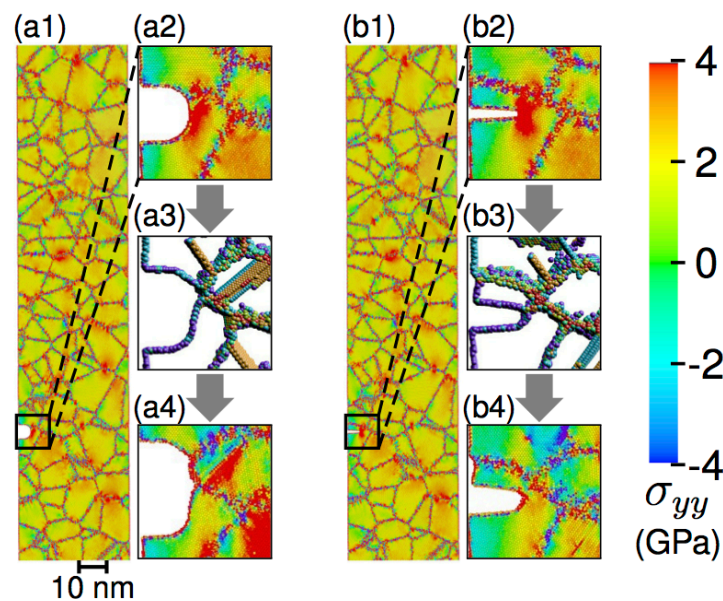


**Figure 3.10:** (a1-a2) Cross-sectional view of tensile stress ( $\sigma_{yy}$ ) at 2.5% applied strain in simulated samples with rounded notch geometry ( $\bar{b} = 0.2$  and  $\bar{h} = 0.03$ ) and sharper notch geometry ( $\bar{b} = 0.23$  and  $\bar{h} = 0.006$ ). (a2-b2) Magnification at notch showing stress concentration at notch tip. (a3-b3) Notch blunting by dislocation and grain boundary plasticity at 6.5% applied strain. (a4-b4) Stress contours show absence of stress concentrations near notches at 8% strain because of previously active plasticity mechanisms. In (a3-b3), atoms are shown only if their central symmetry parameters differ from that of the perfect fcc crystal; the colors indicate the local symmetry<sup>97</sup>. Atoms on twin boundaries, dislocations, intrinsic and extrinsic stacking faults are shown in light blue, dark blue or green (depending on dislocation type), orange and light blue, respectively.

of grain boundary sliding and partial dislocation nucleation and propagation represents the intrinsic deformation mechanism of nanocrystalline Pt nanostructures.<sup>54</sup> Grain boundary sliding generally occurs at a lower applied stress than does dislocation nucleation, but also depends on other factors such as the presence of neighboring grains with favorable orientations, and proximity to free surfaces. Thus, the specific plasticity mechanism active at the notch cannot be predicted from notch geometry alone, although notch geometry influences the local stress.

Surprisingly, the plastic activity near the notches was found to be sufficient to reduce the local stress almost to the background stress level as shown in Fig. 3.10a4-b4. These notches no longer served as “hot spots” with regard to elevated local stress. The notch roots became blunted, thereby shielding the material near the notch from further stress increase. Subsequent localized plasticity in the samples occurred at other stress concentrators in the samples, such as grain boundary triple junctions. This analysis shows that even a severe notch with a strong initial stress concentration may not dominate failure in a sample because plasticity mechanisms inherent to the nanocrystalline material can render the notch ineffective as a stress concentrator at later stages of deformation.

Figure 3.11 presents a compelling example of localized plasticity at the notch, which reduces the stress concentration by blunting, and exposes the intrinsic failure mechanism. Figure 3.11a1 shows an undeformed nanocrystalline slab geometry sample. Figure 3.11a2 shows the same sample under an applied load, in which the emission of dislocations and grain boundary sliding led to large localized deformation at the notch and significant blunting. In Figure 3.11a3, a crack formed along a grain boundary at the notch root and propagated unstably, which ultimately led to failure. Schematic illustrations (Fig. 3.11b1-b3) of the change in notch geometry during the deformation process shows the process of an initial, rounded notch elongating and blunting under

tension, and finally fracturing along a grain boundary by the formation of a crack-like defect with characteristic size equal to the grain size,  $d$ .

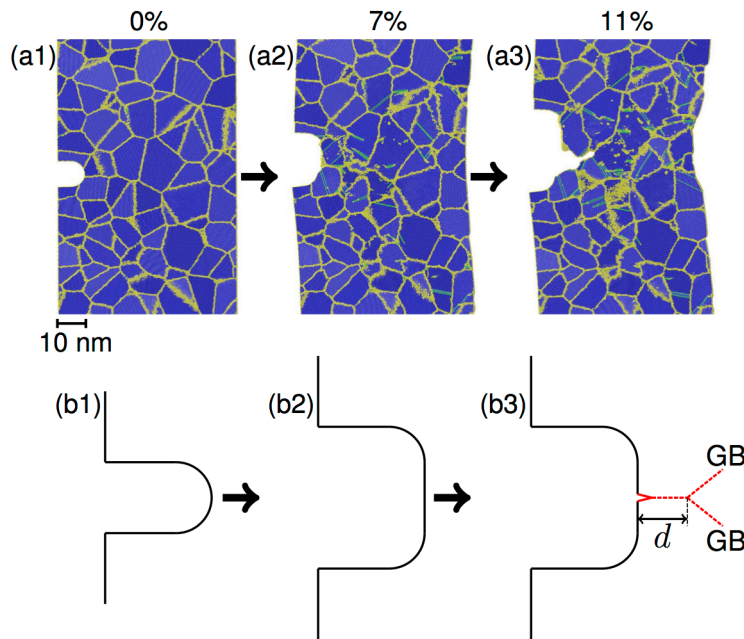


**Figure 3.11:** Cross-sectional view of intergranular fracture at the notch tip in a Pt polycrystalline film. (a1) the notch at 0% strain; (a2) at 7% strain where the notch is blunted by local plasticity emanating from the notch tip and (a3) 11% strain where intergranular fracture initiates at the notch. Atoms are colored based on their structural type as determined by common neighbor analysis; blue for atoms at lattice positions, green for atoms at stacking faults and yellow for atoms at grain boundaries.<sup>98</sup> (b1-b3) The corresponding schematics showing the undeformed notch geometry, notch blunting, and widening and intergranular fracture occurring at a grain boundary with characteristic size  $d$ .

The same failure mechanism can also lead to failure away from the notch and applies to the deformation and failure in the unnotched samples. This is because a crack-like defect can also form at an internal grain boundary (where the stress cannot be further relaxed due to the small crack size), which causes the adjacent grains to pull apart under tension. The intrinsic failure strength of such a crack-like defect can be estimated using the Griffith equation,  $\sigma_f = \sqrt{E\gamma\rho/4ar_0}$ , in which  $E$ ,  $\gamma$ ,  $\rho$ ,  $a$  and  $r_0$  are the elastic modulus, surface energy, crack radius, crack length and interatomic spacing, respectively. We assume that  $\rho = r_0$  for a sharp crack, and  $a \approx d$ , where  $d$  is grain size.

Using  $E=160$  GPa and  $\gamma=2$  J/m<sup>2</sup>, we estimate the Griffith fracture strength to be 3 GPa.<sup>67</sup> This is within a factor of two of the measured fracture strength from experiments and simulations with no adjustable parameters. While Griffith theory applies only to brittle materials, it is reasonable to use in the nanocrystalline samples studied here because no dislocations are generated near the grain-sized crack (which is much smaller than the external notch) to plastically relax the crack stress field and dissipate energy.

### 3.7 Summary

The fundamental picture of failure in nanocrystalline nanostructures with surface flaws that emerges from experiments and simulations is that the competition between stress concentrators due to external flaws and intrinsic microstructural features governs failure strength and location. The samples studied here contain a statistical distribution of internal stress concentrators associated with the microstructure, as well as an external stress concentration in the form of the notch. The dominant internal stress concentrators in these nanocrystalline samples are grain boundary triple junctions. Such features are ubiquitous within nanocrystalline samples with sample diameter large compared to the grain size. The strength of triple junctions as stress concentrators depends on the orientation of the sliding grain boundaries relative to the load as well as on the orientation of the slip systems within the grains for dislocation nucleation. This gives rise to a statistical distribution of stress concentrators associated with microstructural features. As the sample is loaded in tension, the internal or external feature with the highest stress concentration is activated and reaches a local stress at which it either relaxes plastically, or breaks. If relaxation occurs at this site, this sequence of events repeats at the site of the next

highest stress concentration. This process continues to cascade until the active site cannot relax, and fracture ensues.

Samples tend to fail at the external flaw because the surface notch is generally the site with either the highest or one of the highest initial stress concentrations. In samples where failure occurred at the flaw, the failure criteria was first met at the external notch, prior to any plasticity mechanism reducing the local stress at the external flaw to the level of the next weakest site. Grain boundary sliding occurs more easily at the flaw because of the initially high local stress at this location, which means that the intrinsic failure mechanism is more likely to operate at this location rather than elsewhere in the sample.

A direct consequence of such a failure mechanism is flaw insensitivity in strength because the same intrinsic failure mechanism leads to failure, regardless of whether failure occurs at or away from the notch. Since the fundamental failure mechanisms are the same in the presence or absence of notches, the UTS is insensitive to exactly where the failure process starts. The cascade of stress relaxation at stress concentrators via localized plastic deformation dictates that the stress concentration at these locations reaches similar levels, which gives rise to the narrow range of UTS measured in experiment and simulation. This phenomenon is unique to nanocrystalline, nano-scale solids because large stress concentrations can be plastically relaxed (via localized deformation), but those associated with the nano-scale microstructure features cannot be relaxed because they are too small for dislocation nucleation (and localized plasticity). In a macroscale nanocrystalline system, the UTS can be modulated by introduction of very large, sharp flaws that create plastic zones that are too large to be relaxed by local plastic deformation. In such cases, the ultimate failure mode is likely to be more ductile than in our experiments on nano-samples, which show brittle fracture.

Although the MD simulations demonstrate excellent qualitative agreements with experimental results, quantitative differences exist. MD simulations show a moderately ductile fracture on the scale of the grain size, while the experiments suggest a "brittle" fracture process. This discrepancy could be attributed to the differences in grain sizes (6 nm in experiments vs. 14 nm in simulations), the number and orientation of the grains across the cylinder diameter and ahead of notches, and from the much higher strain rates in the simulations. Nevertheless, the experiments and simulations unambiguously demonstrate that failure initiation in nanomaterials is determined by intrinsic microstructural failure mechanisms, and that the UTS is insensitive to the presence of notches.

The results presented here can be summarized as: 1) *flaw-insensitivity* in strength: strength does not depend on whether failure initiates at an external flaw or within the microstructure, and 2) *flaw-sensitivity* in fracture location: most nc-Pt nanocylinders broke at the pre-fabricated flaws regardless of fracture strength as long as the flaw was sufficiently large/sharp. These observations can be explained through competition between internal microstructural features and the external flaw. Brittle failure occurs at a constant stress, independent of the notch provided that the stress-field at the notch is small enough that ductile fracture does not occur and that the microstructural features (crack nucleation sites) are too small to emit dislocations (plastically relax). In classes of materials where plastic deformation cannot occur easily (e.g., ceramics), local plastic relaxation at the notch tip may not be possible and hence such nanomaterials may still fail at a notch-dependent ultimate stress. In the case of nanocrystalline Pt nanostructures, nucleating dislocations is fairly easy; in other nanomaterials, it is possible that non-dislocation plasticity could play a similar role – for example, polymer flow between ceramic units, as in many strong and tough biological materials.

The competition between stress concentrations within the sample naturally leads to flaw-sensitivity in failure initiation location, because incipient deformation and subsequent failure occur at the position of the stress concentration which first satisfies the failure criteria. The localized plasticity in the vicinity of stress concentrators, i.e. triple junctions or flaws, tends to reduce the initially present stress concentrations, which leads to a more effective competition of the multiple stress concentrators throughout the sample volume. This process results in similar fracture strengths for a wide range of flaw shapes and sizes, which is manifested as flaw-insensitivity in strength.

Major external flaws do not necessarily reduce the strength of nanoscale and nanostructured materials, yet may still serve as sites of failure initiation if the intrinsic failure criterion is reached because of the high local stress compared to stresses at internal, microstructural features. The high strength intrinsic to many nanostructures can be maintained while increasing fracture toughness, or resistance to failure at flaws, through microstructural toughening mechanisms. These findings shed light on failure processes in nanomaterials, which commonly show significant deviations from mechanical behavior expected from classical continuum theory. Microstructure and external size information must also be included when predicting failure in nanomaterials. The present results suggest that future nano-fracture testing be performed with careful consideration of microstructural effects as well as well-defined and characterized sample and notch geometries. Sample and notch geometries appropriate for application of classical continuum theories may not be accessible in nanostructures where internal, microstructural features also have important influence on failure.

## Chapter 4. Mechanisms of Failure in Nanoscale

### Metallic Glass

#### 4.1 Introduction

Many engineering materials show enhanced strength<sup>17,19</sup>, ductility (in intrinsically brittle materials)<sup>24,31</sup> and fracture toughness<sup>26</sup> when shrunk to the nanoscale. This leads to the possibility of designing strong and tough functional materials with nanostructured components. One class of promising nano-sized structural materials is metallic glass because of its high strength and enhanced ductility compared to the bulk.<sup>24,99,100</sup> The fracture behavior and toughness of nano-metallic glasses must also be evaluated; unpredictable catastrophic failure has been an outstanding issue that has prevented the widespread insertion of bulk metallic glasses into devices and composites.<sup>7,101,102</sup> Recent work suggests that the tensile strength of bulk and nanoscale metallic glasses may be insensitive to notches.<sup>103,104</sup> The observed notch insensitivity at the nanoscale may be related to the concept of nanoscale flaw tolerance, the continuum-based theory which suggests that the strength of intrinsically brittle materials approaches its theoretical limit and does not diminish due to the presence of flaws when the sample size is reduced to a critical length scale on the order of hundreds of nanometers (previously discussed in Chapter 3.1).<sup>85</sup> These observations provide the impetus for an in-depth investigation of local stresses at the notch root and the mechanisms of failure in nanoscale metallic glasses.

Chapter 3 described our work on fracture in ~100 nm nanocrystalline Pt nano-tensile samples with prefabricated flaws and revealed *flaw-insensitivity* in strength and *flaw-sensitivity*

of failure localization.<sup>95</sup> Experiments and MD simulations showed that these behaviors stem from the competition between stress concentrations at the structural flaw (external) and at discrete microstructural features such as grain boundaries (internal). Although structural flaws serve as strong stress concentrators and generally govern failure location, plasticity within the grains in nanocrystalline metals reduce the stress at the flaw to the level of the stress concentrators of microstructural origin within the structure. The fracture strengths of all nc-Pt samples were similar regardless of whether failure occurred at the structural flaw or within the microstructure. This fracture behavior arises from the combination of the discrete stress landscape within the nanocrystalline microstructure and the nanoscale sample size.<sup>95</sup>

Flaw-insensitivity in strength was observed when microstructural stress concentrations (e.g., grain boundaries and triple junctions) superseded the stress concentrations associated with structural flaws.<sup>88,91,95</sup> By this argument, strength should be sensitive to structural flaws in the absence of microstructural stress concentrations, such as in the case of the nano-sized metallic glass samples studied in this work. The intrinsic mechanical length scale in metallic glasses is associated with clusters of ~100 atoms (i.e., a few atomic diameters in size) that serve as shear transformation zones (STZs) upon deformation. Beyond this nearly atomic scale, metallic glasses exhibit a homogeneous internal energy landscape. This means that an external stress concentrator, such as a structural flaw, should determine failure location and strength when the length scale of the stress concentrator exceeds the size of this atomic-level, internal stress fluctuation. In this chapter, we focus on elucidating the mechanisms of failure in nano-scale metallic glass containing a structural flaw through experimental nanomechanical testing and molecular dynamics simulations.

This work has been submitted for publication in a peer-reviewed journal. Molecular dynamics simulations in this chapter were performed by Dr. Mehdi Jafari-Zadeh and Dr. Zhaoxuan Wu.

### 3.2 Fabrication, characterization and mechanical testing

Ni-P metallic glass nanostructures were electroplated into a PMMA thin film that was patterned with an array of 70-75 nm-diameter holes using e-beam lithography (Fig. 4.1) as described in Chapter 2.2.<sup>55</sup> A 75 at. % Ni – 25 at. % P metallic glass was plated by applying a 80 mA/cm<sup>2</sup> current between the Au-PMMA electrode and a Ni counter electrode in a nickel sulfamate-based aqueous bath as described in Chen *et al.*<sup>99</sup> Cylindrical nanocylinders were formed by plating continuously for 35 s. Notched metallic glass nanocylinders were formed by first plating into a template continuously for 15 s, followed by four successive 5 s periods interrupted by ~10 minute pauses.<sup>95</sup> The plating was continued until the metallic glass nanocylinders began to overgrow the PMMA thin film surface.

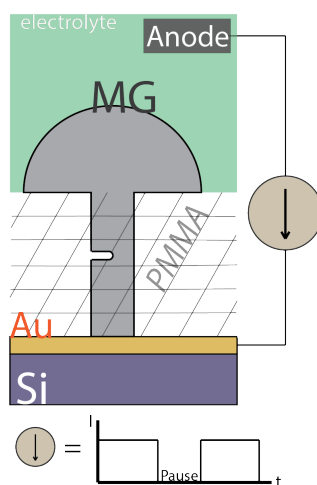


**Figure 4.1:** Schematic of templated electroplating of notched Ni-P nanocylinders using a “paused” electroplating method.

The sample and notch geometries were characterized using scanning electron microscopy (SEM) (FEI Quanta). The notched cylindrical samples had diameters of  $69 \pm 2$  nm and lengths of  $851 \pm 11$  nm. The notches appear as thin lines when imaged in SEM at 20 kV, so the resolution of these observations were limited to features above  $\sim 10$  nm. Despite this limited resolution, small variations in notch length and height were observed qualitatively. The imaging conditions resulted in an electron beam penetration depth that was a significant fraction of the cylinder diameter and images of the notch include information both from the surface and from within the cylinder. All notched samples were fabricated using a paused electroplating methodology and contained a notch  $768 \pm 10$  nm from the base of the cylinder. Three of the seven nanocylinders that were tested contained an additional notch at  $638 \pm 12$  nm from the base of the cylinder. Unnotched nanocylinders with diameters of  $74 \pm 3$  nm and lengths of  $434 \pm 10$  nm were also fabricated. The difference in the dimensions of the notched and unnotched samples was caused by variations in the e-beam lithographed templates used to create these samples.

TEM was used to obtain higher resolution images of the notches and to analyze the microstructure of the nanocylinder. TEM samples of notched and unnotched metallic glass nanocylinders were prepared through a FIB-free process that resulted in minimal damage to the nanostructures. Nanocylinders with poor adhesion to the growth substrate were attached using Van der Waals forces to a custom-fabricated tungsten needle attached to the indenter tip in the InSEM, an *in-situ* SEM nanomechanical testing instrument (Nanomechanics, Inc.). The W needle was used as a micromanipulator. Efforts were made to contact the W needle to the portion of the pillar between the lowest notch and the substrate, so that the notches would not be deformed during TEM preparation. The W needle carrying the pillar was then moved to the Cu TEM grid, and the pillar was glued to the TEM grid using carbon deposition using the SEM

electron beam. The W needle was then removed from the pillar. A small amount of W was applied to the cap of the pillar, far from the notches in the gauge section, using deposition by electron beam (FEI Nova 200 Dual Beam) in order to secure the pillar to the TEM grid.

Bright and dark field TEM images and electron diffraction patterns confirmed that the nanoscale metallic glass samples were amorphous (Figs. 4.2a and b).<sup>99</sup> A small amount of ordering was observed and is likely associated with crystallinity within the e-beam deposited C and W layers on the surface of the Ni-P nanocylinder. The spots visible in the upper left corner of the diffraction pattern in Fig. 4.2b are associated with the Cu TEM grid supporting the nanocylinders. The notch shown in Fig. 4.2a has a height of 10 nm and a rounded notch root similar to that shown schematically in Fig. 4.1. The width and depth of the notch could not be accurately measured using the TEM because of difficulties distinguishing between surface features and those within the nanostructure. Qualitatively, the TEM images revealed that the

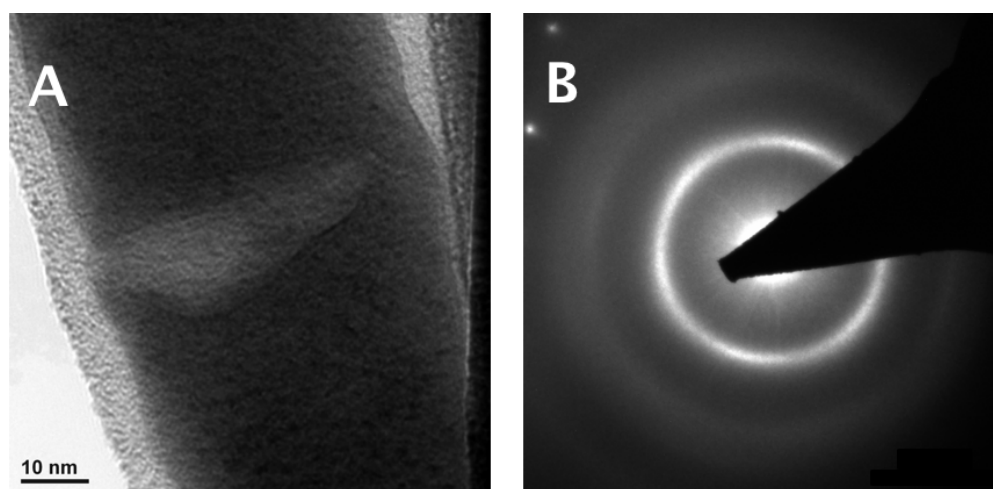


**Figure 4.2:** (A) Bright field TEM image of the notched region in a Ni-P nanocylinder. (B) Corresponding electron diffraction pattern showing the amorphous nature of the nanocylinder. Single crystal diffraction peaks are due to the Cu TEM grid supporting the nanocylinder.

notch extends a significant distance across the diameter of the sample and that the structure is thinner at the notch than at surrounding areas based on diffraction contrast. No change in the amorphous structure between the notch region and rest of the structure was observed.

*In-situ* SEM uniaxial tension tests were performed at a nominal strain rate of  $0.001 \text{ s}^{-1}$  on notched and unnotched Ni-P nanocylinders using the InSEM system.<sup>28</sup> Unnotched Ni-P samples were glued to the substrate using a small amount of e-beam deposited W (Nova 200, FEI). It was not necessary to glue notched Ni-P samples because they always broke within the cylindrical gauge length at stresses lower than the interfacial strength between the sample and the underlying substrate.

### 4.3 Mechanical behavior in tension

Unnotched,  $\sim 75 \text{ nm}$  diameter Ni-P nanocylinders showed  $\sim 3\%$  post-elastic deformation in tension in contrast with the brittle failure observed in wider Ni-P metallic glass samples of the same composition (Fig. 4.3a).<sup>99</sup> The ultimate tensile strength (UTS) of the eight tested unnotched cylinders was  $1.9 \pm 0.1 \text{ GPa}$ , consistent with previously reported strengths of thicker,  $105 \text{ nm}$ -diameter Ni-P metallic glass nanocylinders.<sup>99</sup> Failure in the unnotched samples occurred through necking, followed by shear banding resulting in an angled fracture surface (Fig. 4.3b). The fracture planes were inclined, on average, by  $\sim 25^\circ$  relative to the loading axis but showed variation in the  $5^\circ - 42^\circ$  range, as measured from the SEM images. We note that because the fracture surface was not always aligned with the viewing direction, the values reported here should be considered lower bounds on the fracture angle for each sample.

The notched Ni-P nanocylinders always broke at the notch. Their average failure stress,  $1.2 \pm 0.4$  GPa, was significantly lower than that of the unnotched nanocylinders. Six of the seven tested notched samples broke at an UTS lower than that of the unnotched pillars. One notched pillar broke at an UTS of 1.9 GPa. Notched samples that failed at  $\sim 1.2$  GPa exhibited limited plastic strain, 0.3%, as compared to 3% plastic strain in the unnotched nanocylinders (Fig. 4.3e). This is a clear demonstration that the stress concentration at the notch plays a key role in the deformation mode. Nanoscale metallic glasses have previously been shown to exhibit increased ductility, but no increases in strength when reduced below  $\sim 100$  nm in size.<sup>24,25</sup> If the only role of the notch was to decrease the effective diameter and the cross-sectional area of the nanocylinder, then increasing the notch size should lead to higher ductility. Figure 4.3f proves that the Ni-P samples are in a size-independent regime with regards to strength, because decreasing the unnotched sample diameter from  $\sim 105$  nm to  $\sim 75$  nm does not change the UTS ( $\sim 1.9$  GPa in both cases). The decrease in UTS observed in the notched  $\sim 70$  nm samples ( $\sim 1.2$  GPa) must be due to the effect of the notch rather than due to a reduction in the sample diameter.

The fracture surface in the notched samples was inclined  $4^\circ$  relative to the loading axis on average, with all samples breaking at angles within the  $0^\circ$ - $10^\circ$  range (Fig. 4.3d). Part of the observed “fracture surface” may, in fact, be the surface of the notch; this is difficult to quantify because the notch sizes could not be precisely determined.

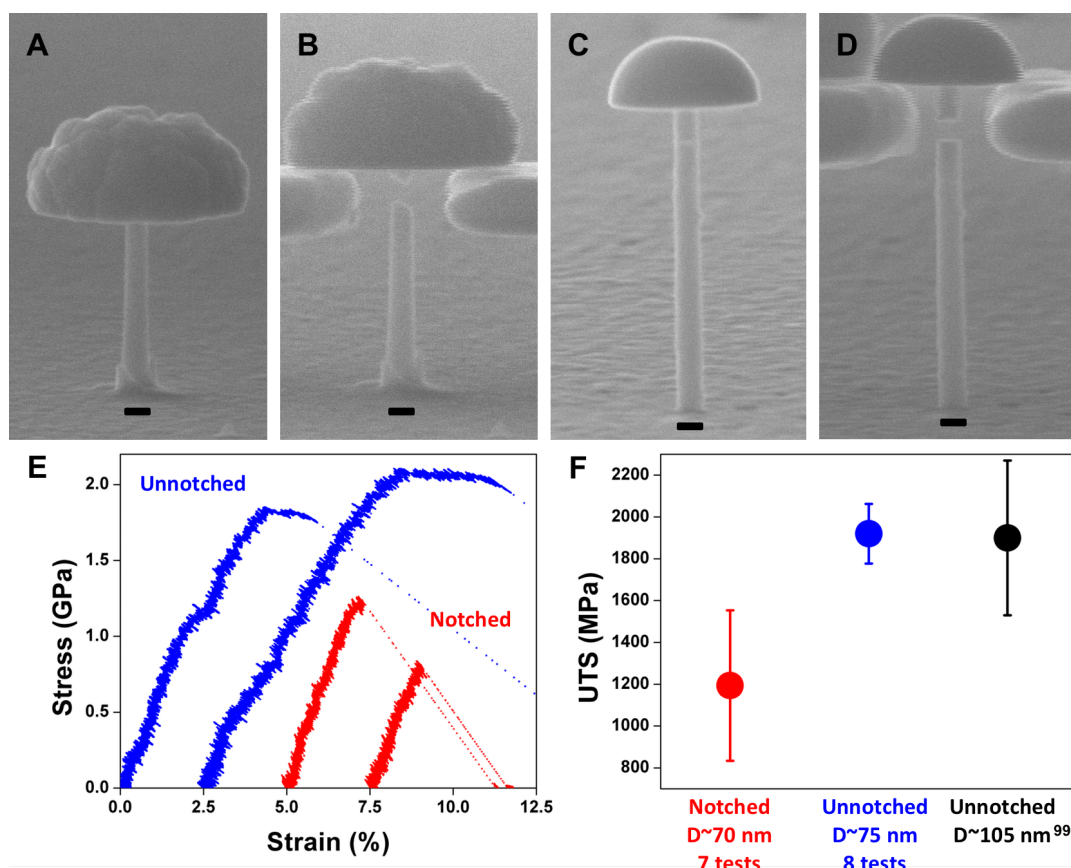


**Figure 4.3:** SEM images of an unnotched Ni-P nanocylinder (A) before and (B) after tensile testing and a notched Ni-P nanocylinder (C) before and (D) after tensile testing. (E) Characteristic stress-strain curves for notched (red) and unnotched Ni-P nanocylinders (blue). (F) Comparison of the UTS of notched and unnotched Ni-P nanocylinders with  $\sim 70$  nm diameters, and unnotched Ni-P nanocylinders with  $\sim 105$  nm diameters.<sup>99</sup>

#### 4.4 Molecular dynamics simulations

To elucidate the physical origin of the effect of the notch on failure, we performed large-scale molecular dynamics (MD) simulations on notched and unnotched  $\text{Fe}_{75}\text{P}_{25}$  metallic glass nanocylinders. The atomic interactions within the Fe-P metallic glass were modeled using the embedded atom method (EAM) potential parameterized by Ackland *et al.*<sup>105</sup> We focus on Fe-P metallic glasses rather than Ni-P glasses here because no Ni-P potentials that have been validated against measured mechanical properties of Ni-P are available, while one does exist for Fe-P. Iron

and nickel have similar electronegativity, both are Group VIII transition metals from the same row of the periodic table, and the bonding in  $\text{Fe}_{75}\text{P}_{25}$  and  $\text{Ni}_{75}\text{P}_{25}$  is very similar. On this basis, we expect that Fe-P is a reasonable surrogate for Ni-P for MD simulations. However, as for MD simulations based upon any types of empirical potentials, the details of the predictions should be viewed with some skepticism. Here, we focus on major mechanistic features and trends in behavior.

Simulations were performed using the Large-Scale Atomic/Molecular Massively Parallel Simulator (LAMMPS).<sup>66</sup> The simulation samples were prepared from a melting-and-quenching simulation of a randomly substituted  $\text{Fe}_{75}\text{P}_{25}$  solid solution whereby a  $\text{Fe}_{75}\text{P}_{25}$  rectangular prism with periodic boundary conditions (PBC) in all directions was melted at 2000 K and equilibrated for 1 ns. Then, the sample was quenched to 1 K at a cooling rate of  $0.5 \text{ Kps}^{-1}$ . The time step for the melting-and-quenching was chosen to be 0.002 ps, and the isothermal-isobaric ensemble (NPT) was employed to maintain the pressure of the system at zero. The Verlet algorithm<sup>106</sup> and the Nose-Hoover thermostat/barostat<sup>107,108</sup> were used to integrate the equations of motion. After quenching, cylindrical nanocylinders were cut from the quenched bulk metallic glass. The samples were relaxed using the conjugate gradient (CG) minimization technique<sup>109</sup> as implemented in LAMMPS. The nanocylinders were then equilibrated at the temperature of the tensile test (1 K) and zero pressure for 0.5 ns using the NPT ensemble. Uniaxial tensile loading was applied to the nanocylinders by rescaling the simulation box and applying a time step of 0.001 ps. During tensile loading, the PBC was applied just along the loading direction, and the temperature of the system was maintained at 1 K, which reduces the thermal fluctuation effects and facilitates the analyses of atomic quantities.<sup>110</sup>

The simulated unnotched samples were constructed as cylinders with a diameter of 40 nm and a length of 120 nm (Fig. 4.4a). The notched sample was formed by cutting a rounded notch with length of 5.7 nm and height of 3.4 nm out of the unnotched sample (Fig. 4.4e). Deformation and failure of the simulation samples were analyzed in terms of the local atomic von Mises shear strain,  $\epsilon^{vM}$ <sup>111,112</sup>. Visualization of  $\epsilon^{vM}$  has been widely used to investigate shear band (SB) formation in metallic glasses.<sup>111</sup> Figures 3A-H show  $\epsilon^{vM}$  for a central cross section of representative unnotched and notched nanocylinders at different applied strains,  $\epsilon$ . Figures 4.4a-d show that the distribution of  $\epsilon^{vM}$  in the unnotched sample is uniform up to the UTS, which corresponds to  $\epsilon_{unnotched}^{UTS} \sim 10.8\%$ . Beyond the UTS, a shear band forms, which leads to failure at an oblique angle ( $\sim 45^\circ$ ) relative to the loading direction. The notched nanocylinder does not fail through shear banding, but instead fails by crack initiation and propagation from the notch root after reaching the UTS (Fig. 4.4e-h). The crack propagates from the notch in a direction orthogonal to the applied load. The engineering stress-strain data for both the unnotched and notched nanocylinders are shown in Fig. 3I. The UTS for the unnotched and notched samples is attained at applied strains of  $\epsilon_{unnotched}^{UTS} \sim 10.8\%$  and  $\epsilon_{notched}^{UTS} \sim 5.8\%$ , respectively. The UTS of the notched sample was  $\sim 25\%$  lower than that of the unnotched sample.

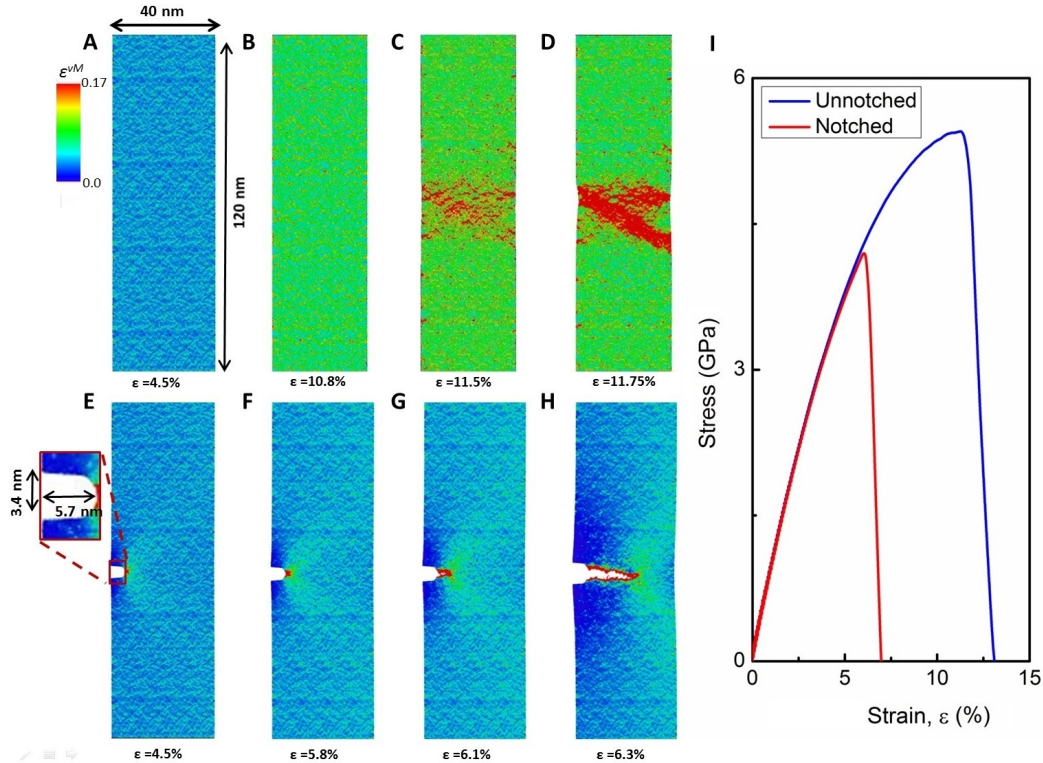


**Figure 4.4:** MD simulation results with the atoms shaded according to their von Mises strain  $\epsilon^{vM}$  in a cross-section of the unnotched sample at (A)  $\epsilon=4.5\%$  (uniform  $\epsilon^{vM}$ ), (B)  $\epsilon=10.8\%$  (strain at ultimate tensile stress), (C)  $\epsilon=11.5\%$  (at the inception of shear band), and (D)  $\epsilon=11.75\%$  (well developed shear band). For comparison,  $\epsilon^{vM}$  is plotted for the notched sample at (E)  $\epsilon=4.5\%$  (elevated local strain at the notch), (F)  $\epsilon=5.8\%$  (strain at the ultimate tensile stress and beginning of crack formation), (G)  $\epsilon=6.1\%$  (crack propagates horizontally), and (H)  $\epsilon=6.3\%$  (failure via crack propagation). (I) Stress-strain curves corresponding to the simulated tensile tests of unnotched and notched amorphous samples.

The MD simulations appear to be in excellent agreement with the experimental observations and unambiguously demonstrate that the notch governs the failure mode and mechanism in nanoscale metallic glasses. Both simulations and experiments show that the unnotched nanocylinders failed in a ductile fashion via shear banding, with the fracture surface oriented at an oblique angle with respect to the loading axis. The notched nanocylinders failed in a brittle manner via crack propagation from near the notch root, horizontally across the sample. The tensile strength of the notched sample was significantly smaller than that of the unnotched sample in both experiments (36% reduction) and simulations (25% reduction).

MD simulations were previously performed on Cu-Zr nanoscale metallic glasses in which failure always initiated from rounded flaws.<sup>104</sup> Our results agree with these simulations in fracture location but not in failure strength. The load at fracture was normalized by the cross-sectional area at the flaw to obtain a normalized UTS in the Cu-Zr metallic glass nanoscale sample. This normalized failure strength was found to be independent of notch size. The notch in the Fe-P metallic glass nanocylinders reduces the cross-sectional area of the cylindrical sample by 9%, but reduces its strength by 25%, which indicates notch-sensitivity at the nanoscale in this material. This difference in behavior is indicative of a difference in the underlying mechanism of failure between notched Cu-Zr and notched Fe-P glasses.<sup>110</sup>

Figures 4.5a-e show several close-up views of the notch root region at different stages of loading. Microscopic voids were nucleated in front of the notch root at an applied strain of  $\epsilon=5.93\%$ , a value slightly above  $\epsilon_{notched}^{UTS} \sim 5.8\%$ , and subsequently grew while additional small voids emerged (Figs. 4.5a-c). The coalescence of these voids and their linkup with the dominant crack led to crack propagation (see Figs. 4.5d, e) and eventually caused fracture and the

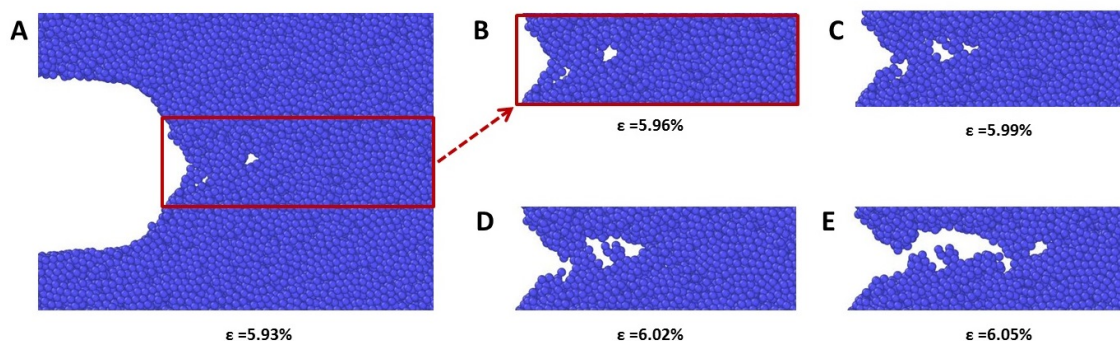


**Figure 4.5:** Detailed view of the deformation in the notched sample showing (A) formation of atom-scale voids ( $\epsilon=5.93\%$ ), (B) growth of voids ( $\epsilon=5.96\%$ ), continued growth of voids and formation of additional voids at (C)  $\epsilon=5.99\%$  and (D)  $\epsilon=6.02\%$ , and (E) coalescence of voids ( $\epsilon=6.05\%$ ). Images show a cross-section of the simulation nanocylinder.

formation of a horizontal fracture surface. Although fracture is microscopically ductile (because it occurs through void nucleation, growth and coalescence), the overall failure process can be viewed as brittle crack propagation because the total amount of plastic deformation is very small.

## 4.5 Stress triaxiality at structural flaw

We postulate that the observed cavitation was caused by the substantial stress triaxiality ahead of the notch. The atomic stress triaxiality is defined as  $\eta = Tr(\boldsymbol{\sigma})/3\sigma^{vM}$ , where  $\boldsymbol{\sigma}$  is the atomic stress tensor. When  $\eta$  is large, hydrostatic stress dominates, leading to void nucleation and growth. When  $\eta$  is small, shear deformation dominates and shear banding is expected.<sup>113,114</sup> We calculated  $\eta$  in both the notch root region (red region in the inset of Fig. 4.6a), as well as for the whole sample excluding the notch root area (blue region in Fig. 4.6a). Figure 4.6a shows  $P(\eta)$ , the stress triaxiality distribution in the notch root area (red curve) in comparison with that for the remainder of the sample (blue curve) at an applied strain of  $\varepsilon=4.5\%$ . It is seen that  $\eta$  at the notch root is shifted toward more positive values and its average increased by almost 300% to 0.38 (red dash line) from  $\eta = 0.13$  as compared with the rest of the sample (blue dashed line). Figure 4.6b shows the normalized value of average stress triaxiality,  $\eta_{notch-root}/\eta_{remainder}$ , as a function of applied strain,  $\varepsilon$ . This figure indicates that during the uniaxial tensile test, there is a much greater degree of volumetric expansion at the notch root as compared with rest of the sample, which drives the nucleation and growth of the voids. Figures 4.6c-d show the spatial distribution of  $\eta$  in the cross-section of the notched nanocylinder at the UTS (corresponding to  $\varepsilon=5.8\%$ ). Much higher values of  $\eta$  are observed in front of the notch root. Voids are nucleated in these regions of large  $\eta$  near the notch root at a very small increment in the applied strain (to 5.9%), as seen in Fig. 4.6e.

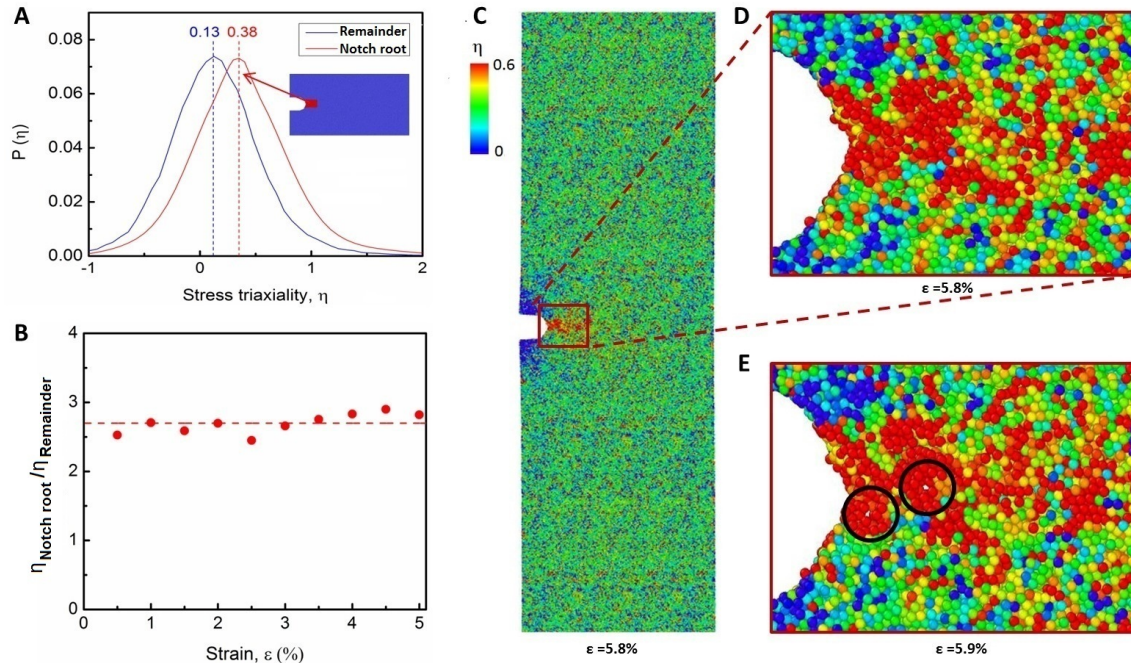


**Figure 4.6:** (A) Plot of the probability density of the stress triaxiality,  $P(\eta)$ , at the notch root (red curve) in comparison with the  $P(\eta)$  for the remainder of the sample (blue curve) at an applied strain of  $\epsilon = 4.5\%$ .  $P(\eta)$  is calculated for a 2 nm thick slice through the cylindrical sample. The  $P(\eta)$  at the notch root is calculated for the region located in front of the notch root (red area in the inset). The data for the remainder of the sample is calculated for all other atoms in the sample (blue region in inset). (B) The normalized value of average stress triaxiality,  $\eta_{\text{notch-root}}/\eta_{\text{remainder}}$ , as a function of applied strain,  $\epsilon$ . The spatial distribution of  $\eta$  in (C) the cross section of the notched nanocylinder at the strain corresponding to the UTS, (D) near the notch at the UTS, and (E) near the notch at a slightly higher strain  $\epsilon = 5.9\%$ . Voids nucleate at the notch root due to high localized  $\eta$  (indicated by the black circles).

## 4.6 Summary

Our results indicate that flaws are critical to the failure strength and failure mechanism in this nanoscale metallic glass. Recent theory suggests the emergence of flaw tolerance in solids at very small length scales, which applies directly to brittle materials.<sup>85</sup> The amorphous system examined here shows non-trivial localized plasticity through either shear banding or voiding. The present observations demonstrate that the effects of flaws are consistent with classical analyses and that these are remarkably robust - applicable down to the scale of the smallest man-made

mechanical structures. While our earlier work showed that nanocrystalline metals can be flaw-tolerant in terms of strength<sup>95</sup>, this work conveys that the flaw tolerance is associated with the specific discrete microstructure rather than with the nanoscale sample size. The absence of a discrete microstructure, as is the case for the amorphous metallic glasses in this work, implies no flaw-tolerance in nanoscale materials that exhibit localized plasticity.

In summary, we explored the deformation mechanism and failure modes of notched and unnotched amorphous metallic glass nanostructures under uniaxial tension in experiment and atomistic simulation. Structural flaws reduce sample failure strength and are critical to the failure location and failure mode. In the unnotched nanocylinders, shear band formation led to failure at an oblique angle with respect to the loading direction. The notched nano-cylinders showed virtually no ductility and failed via crack initiation and propagation along the extension of the notch root. We found that the nominally brittle propagation of cracks in the notched samples was a consequence of void nucleation, growth, and coalescence in response to the large stress triaxiality at the notch root. This work unambiguously demonstrates that the deformation mode and failure strength of nanostructures depends sensitively on the presence of structural flaws, even in the absence of discrete microstructural features. These findings demonstrate that flaw-insensitivity is not a general feature of nanoscale mechanical systems; classical models that describe the effects of flaws on failure can be applied at the nanoscale provided that localized plasticity can readily occur. An important caveat is that even when localized plasticity is possible, discrete microstructural features in nanocrystalline materials can lead to internal stress concentrations that make material strength flaw-insensitive.

# Chapter 5. Strong and Light Architected Cu Meso-lattices

## 5.1 Introduction

A decade of intense study has shown the universality of the “smaller is stronger” size effect in single crystalline metals with sub-micron dimensions subjected to uniaxial deformation.<sup>16,17</sup> Single crystalline metallic samples with micro- to nanoscale dimensions often have strengths enhanced by orders of magnitude relative to the equivalent bulk-scale materials because plasticity is carried out via nucleation of dislocations from single-arm sources and/or surfaces rather than by dislocation multiplication alone.<sup>20,22</sup> Cylindrical micro- and nanopillars have served as the typical geometry for studying plasticity in nanocrystals because they experience a well-defined stress state upon uniaxial loading. Fewer efforts have been dedicated to exploring the “smaller is stronger” paradigm under complex structural geometries or stress states.

We show that size-dependent strengthening can be used in a hierarchical structural material by designing and building a porous meso-lattice out of microscale structural elements such that a high free surface to volume ratio is preserved and lattice beams behave essentially like interconnected single crystalline micropillars.<sup>115,116</sup> The use of this materials size effect has been previously demonstrated in nanoporous foams, in which structural strength is determined by ligament size, in addition to relative density and material properties.<sup>30,117</sup> Although porous foams are appropriate for many low density structural applications, the topologies of ordered

architected cellular solids can be designed to optimize properties like strength, stiffness, and fracture toughness per density at every relevant scale – from microstructural features to individual truss members to unit cells to the overall structure.<sup>118,119</sup> The use of nanoscale beams in cellular solids enables utilizing the material size effect to enhance the mechanical strength of the structure by providing another tunable parameter, characteristic lattice member size, in addition to geometrical attributes. In this paradigm of bulk-material processing, the mechanical properties can surpass those attainable by the existing processing routes because it enables independent optimization of structural topology, material chemistry and microstructure.

Ordered architected structures are ideal for lightweight structural applications because they have a superior strength per weight ratio compared with disordered porous foams.<sup>115,118</sup> In particular, the octet structure, a lattice with a face-centered cubic arrangement of nodes, is predicted to have a yield strength that scales linearly with relative density,  $\bar{\rho}$ , because structural deformation is accommodated by stretching of the lattice members.<sup>120</sup> Open-cell foams whose beams deform by bending have strengths that scale as  $\bar{\rho}^{3/2}$ , which means that the octet-truss and other stretching-dominated geometries are a better choice for lightweight structural applications. Such stretching-dominated 3D ordered architectures have been notoriously challenging to fabricate, especially on the microscale, where sample size-effects are expected to emerge. Mechanically robust 3D metallic lattices and sandwich structures have been formed at the macroscale through investment casting, weaving metal fibers and by folding and welding stacks of 2D metal lattices.<sup>121,122</sup> Hollow Ni and NiP micro-lattices with features like the tube wall thickness, lattice beam length, and sample dimensions extending from the nano- to the millimeter scale were formed by the electroless plating of metal onto a 3D photolithographed polymer scaffold which was subsequently removed.<sup>123,124</sup> The structural topology of these micro-trusses is

limited by the polymer waveguide fabrication technique to produce bending-dominated geometries only. Hollow metallic and ceramic nano-lattices have also been fabricated through atomic layer deposition and RF sputtering onto a solid polymer lattice fabricated by 2-photon lithography.<sup>125-127</sup> These hollow nanostructured lattices are extremely mechanically robust considering their lightweight nature, but are limited in their stiffness and strength compared to lattices with solid beams.

In this chapter, we describe fabrication and mechanical compression experiments on solid Cu lattices with octet structural topology and micron-sized beam thicknesses, in which lattice members deform similarly to single crystalline micropillars. The contents of this chapter have been submitted for publication in a peer-reviewed journal.

## **5.2 Fabrication and characterization**

Solid metallic meso-lattices were fabricated by electroplating Cu into a polymer template with pores defined via direct laser writing (Fig. 5.1). We developed this process by extending the method of Gansel et al. to 3D interconnected architectures.<sup>128</sup> A 60-nm thick layer of indium-tin oxide (ITO) is first sputtered onto a glass cover slip to provide a conductive surface for electroplating. Positive photoresist (AZ4620, Microchem) with a thickness of 20 to 30  $\mu\text{m}$  is subsequently spincoated onto the ITO-covered glass. 3D direct laser writing (DLW) using 2-photon lithography (Nanoscribe, GmbH) was used to expose the photoresist in the shape of the desired 3D structure. Following development of the photoresist, potentiostatic electrodeposition was used to infiltrate the pores in the polymer template using a three-electrode electrochemical cell with a Pt counter electrode and an Ag/AgCl reference electrode. Cu meso-lattices were

plated at 2 V in a Cu bath containing 125 g/l  $\text{CuSO}_4 \cdot 5\text{H}_2\text{O}$  and 50 g/l  $\text{H}_2\text{SO}_4$ . The undeveloped photoresist was removed by soaking in N-methylpyrrolidone after the metallic meso-lattices were formed inside the mold.

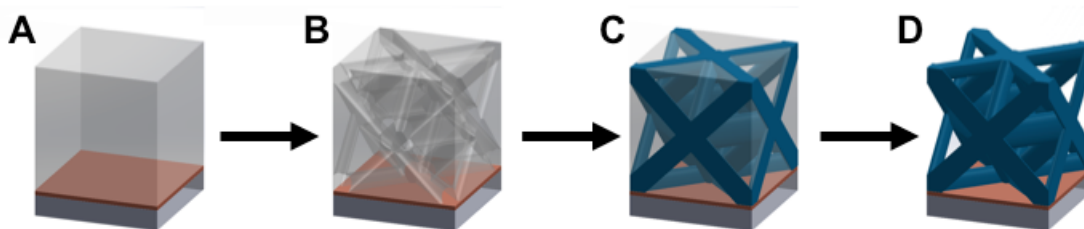


**Figure 5.1:** Solid mesostructured lattices are fabricated by a) spincoating positive photoresist onto an ITO-covered glass cover slip, b) direct laser writing of 3D pattern into the photoresist, which is subsequently chemically developed leaving a 3D network of pores in the photoresist, c) electroplating of solid 3D lattice into pores, and d) stripping of photoresist to leave freestanding lattice structure.

We chose the octet-truss geometry for the meso-lattices because of the superior strength per weight ratio of this structural topology. Cu octet meso-lattices were created with 6  $\mu\text{m}$  and 8  $\mu\text{m}$ -wide unit cells. Samples had square bases with side lengths of between 25 to 26  $\mu\text{m}$ , and heights of 20 to 23  $\mu\text{m}$ , as shown in Figure 5.2a. Meso-lattices were formed of solid elliptical beams joined at solid nodes (Fig. 5.2b). The minor axis of the elliptical beam,  $d$ , ranged from 950 nm to 1.5  $\mu\text{m}$  depending on the laser power used during the DLW process. The ratio between major and minor axis was 1.4 to 1.8. The resulting structures had relative densities,  $\bar{\rho}$ , ranging from 0.3 to 0.8, calculated using a Solidworks model of the solid octet that accurately represents the geometry within the nodes and of the individual elliptical beam members.

TEM was used to identify the microstructure of the Cu within the meso-lattice (FEI, TF-30). A micromanipulator (FEI EZ-Lift) inside a SEM/FIB Dualbeam (FEI Versa) was used to transfer a Cu meso-lattice from its growth substrate to a Cu TEM grid. A sharp W probe at the end of the micromanipulator was attached to the meso-lattice using e-beam deposited Pt glue.

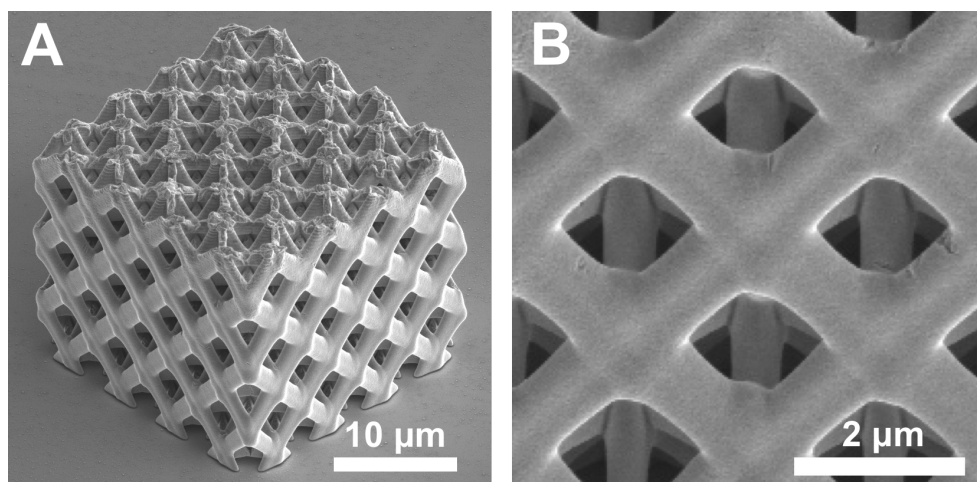


**Figure 5.2:** (A,B) SEM images of Cu meso-lattice with octet geometry taken at 52° tilt.

The meso-lattice was then carried by the micromanipulator to a Cu TEM grid, attached to the TEM grid with W glue, and detached from the W probe using FIB milling. Sections of the transferred meso-lattice were thinned using FIB milling at 30 kV voltage and progressively lower currents to prevent FIB damage to the sample. A final current of 10 pA was used to thin the sample to approximately 60 nm. Bright field/dark field TEM images, and the corresponding diffraction patterns, on three different thinned sections revealed that the micron-wide lattice beams contained a complex microstructure, which consisted mostly of micron-sized grains that spanned the entire beam width, as well as regions of nanocrystalline and nanotwinned grains (representative TEM images are shown in Figure 5.3). The TEM analysis of microstructure is limited because the FIB-preparation of meso-lattice TEM samples can only make “thinned” sections of the TEM sample up to a micron or two in width and height. Larger FIB-milled sections tend to fold over, develop holes or otherwise fail mechanically. The thinned regions are likely to have microstructures typical of the entire meso-lattice because the meso-lattice was fabricated in a single potentiostatic electroplating step.

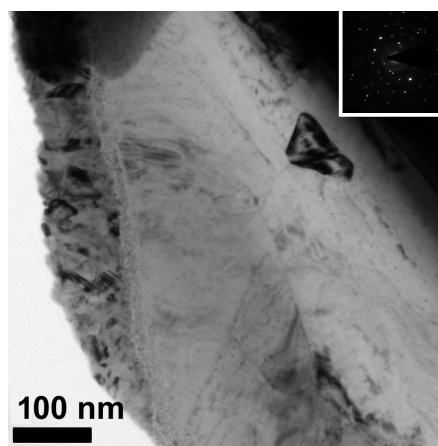


**Figure 5.3:** Bright field transmission electron microscope (TEM) image of focus ion beam (FIB) thinned meso-lattice beam. Inset shows corresponding diffraction pattern.

A more holistic view of meso-lattice microstructure was obtained through ion channeling of FIB milled cross-sections of a 10- $\mu\text{m}$  thick Cu thin film electroplated at conditions identical to those used to make the meso-lattices (Fig. 5.4). These cross-sections were large enough to encompass entire grains, unlike the FIB-thinned TEM samples. We found the grain size in the film to be  $2 \pm 1 \mu\text{m}$ . 9% of grains, by volume, contained nanotwins. The  $2 \mu\text{m}$  average grain size in lattice members with minor axis lengths  $d = 900\text{-}1.5 \mu\text{m}$  indicates that substantial regions within the meso-lattices consisted of single crystals which span the entire lattice member.

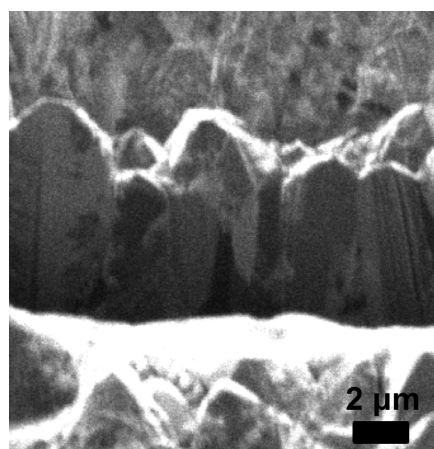


**Figure 5.4:** Ion channeling of FIB milled cross-section of Cu thin film electroplated at identical conditions to the meso-lattices.

### 5.3 Uniaxial compression

Uniaxial compression experiments were carried out in the G200 XP Nanoindenter (Agilent) using a 120  $\mu\text{m}$ -diameter diamond flat punch tip at a prescribed strain rate of  $0.0025 \text{ s}^{-1}$ . Load-displacement data from compression experiments were converted to engineering stress-strain curves by normalizing by sample height and cross-sectional area. The stress-strain plots obtained from compression tests have features typical of cellular solids compression such as linear-elastic, plateau, and densification regions (Fig. 5.5).<sup>119</sup> Strain bursts occurred immediately

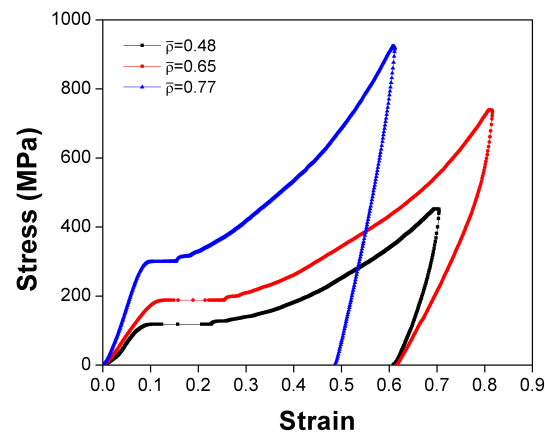


**Figure 5.5:** Stress-strain response from uniaxial compression of meso-lattices with a 6  $\mu\text{m}$  unit cell.

after plastic yielding in the plateau region for  $\bar{\rho}$  below 0.69. The loading moduli of the meso-lattices were obtained by calculating the slope of the initial linear rise in stress during compression and ranged from 600 to 3600 MPa for  $\bar{\rho}$  of  $\sim 0.4$  to 0.8 and increased with increasing  $\bar{\rho}$  (Fig. 5.6). The loading modulus corresponds to the elastic modulus under ideal testing conditions but is likely convoluted by surface roughness and imperfect alignment between sample and flat punch indenter in micro-compression experiments.

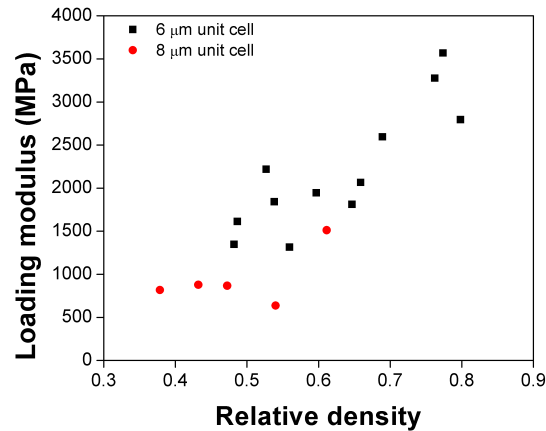


**Figure 5.6:** Loading moduli for Cu meso-lattices as a function of relative density.

Meso-lattices were deformed to various strains past the point of yielding and examined with SEM. Parallel crystallographic slip offsets were observed in several lattice members in an 8  $\mu\text{m}$  unit cell meso-lattice with  $\bar{\rho} = 0.47$  compressed to 28% strain (Fig. 5.7a). These features are characteristic of plastic shear in single crystals deformed along a low-symmetry orientation.<sup>16,129</sup> Wavy lines also appeared across some lattice members, which may indicate grain boundaries along which grain offsets occurred during plastic deformation. Fracture and twisting of individual lattice members at nodes took place near the base of the meso-lattice. It is likely that the strain bursts present in the compressive stress-strain data for meso-lattices with  $\bar{\rho} < 0.69$  correspond to these fracture events because the average extent of the the strain bursts,  $\sim 1.5 \mu\text{m}$ , roughly matches the amount of deformation observed at fracture locations. The displacement during strain bursts is too large to be attributed solely to formation of slip bands across single crystalline regions, but the strain bursts also likely stem from the initiation and release of dislocation avalanches within the single crystalline regions of the truss members, akin to micro-pillar deformation.<sup>16</sup> A post-deformation SEM image for a meso-lattice with a 6  $\mu\text{m}$  unit cell and  $\bar{\rho} = 0.49$  that was compressed to 45% strain is shown in Figure 5.7b. This level of strain

corresponds to the densification region in the stress-strain curve, at which point extensive plastic deformation and fracture events have already occurred. We observed several cracks that extended across multiple nodes in the meso-lattice and a flattened base region. The top face of the meso-lattice retained its original square shape after compression.

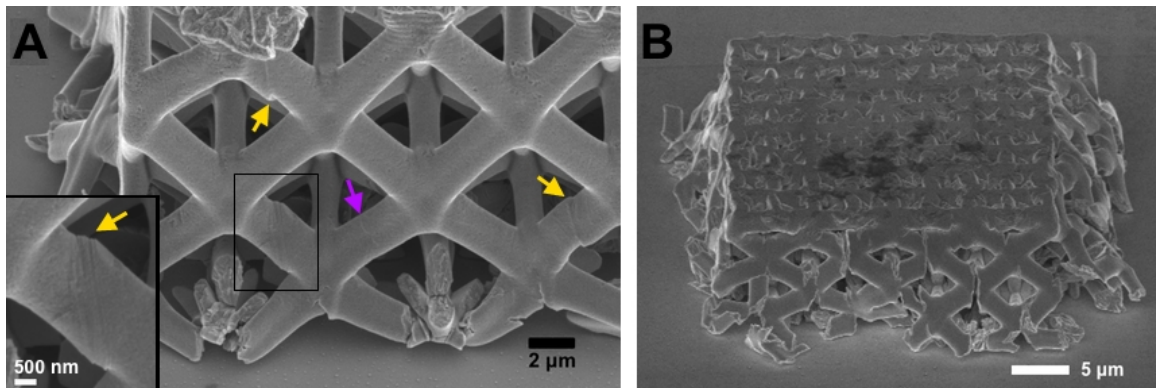


**Figure 5.7:** (A) SEM image of meso-lattice with 8  $\mu\text{m}$  unit cell and relative density of 0.47 compressed to 28% strain. Slip planes in single crystals (yellow arrows), offsets at grain boundaries (purple arrow), and fracture at nodes are visible signs of plastic deformation. Inset shows magnified image of slip planes. (B) SEM image of meso-lattice with 6  $\mu\text{m}$  unit cell and relative density of 0.49 compressed to 47% strain.

The yield point was determined using a 0.2% strain offset from the linear elastic loading region. Yield strengths of the meso-lattices are plotted as a function of relative density in Figure 5.8 and range from 110 to 330 MPa for  $\bar{\rho}$  of  $\sim 0.5$  to 0.8 for a unit cell size of 6  $\mu\text{m}$ , and 50 to 100 MPa for  $\bar{\rho}$  of  $\sim 0.4$  to 0.6 for a unit cell size of 8  $\mu\text{m}$ . Size-dependent strengthening was revealed by comparing meso-lattice yield strength against bulk yield strength. The bulk hardness,  $H$ , was measured to be  $400 \pm 250$  MPa through nanoindentation into the 10  $\mu\text{m}$ -thick Cu thin film electroplated at identical conditions to the Cu meso-lattices.<sup>58</sup> The yield strength of the bulk Cu,  $\sigma_{ys}$ , was estimated by applying the Tabor relation to the nanoindentation hardness,  $H$ , of the Cu thin film:<sup>130</sup>

$$H = 3\sigma_{ys} \quad (5.1)$$

Bulk yield strength was calculated to be  $133 \pm 83$  MPa. The yield strength for Cu with 2  $\mu\text{m}$ -sized grains was calculated to be 102 MPa using the Hall-Petch equation.<sup>3</sup> It is reasonable that the measured yield strength is slightly higher than the calculated Hall-Petch yield strength because 9% of the electroplated Cu thin film consists of grains with nano-twinned microstructure, which have higher strengths than conventional polycrystalline grains.<sup>4,81</sup>

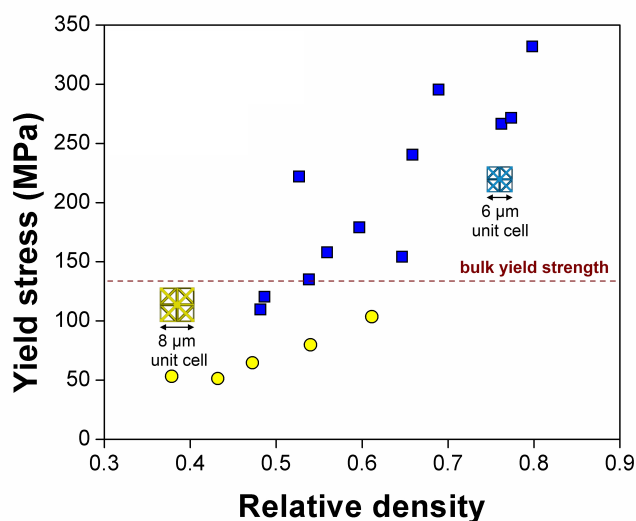


**Figure 5.8:** Yield strength of meso-lattices as a function of relative density compared against bulk yield strength (dashed line) obtained from nanoindentation onto a Cu thin film electroplated at the same conditions as the meso-lattices. Blue square data points correspond to an 8  $\mu\text{m}$  unit cell structure, and yellow circle data points correspond to a 6  $\mu\text{m}$  unit cell structure, as shown schematically in the plot.

Comparison of the yield strengths of the meso-lattices and of the electroplated Cu thin film revealed that meso-lattices with  $\bar{\rho} > 0.5$  and 6  $\mu\text{m}$  unit cell size were *stronger* than the bulk yield strength, with the densest structures ( $\bar{\rho} \sim 0.8$ ) having a strength 1.8 times higher than the strength of bulk Cu (Fig. 5.8). This finding is remarkable because introducing porosity into a bulk material should lower its strength, because less material within the same volume supports the same load in the case of the porous material. Microstructural analysis and SEM images of the post-compression samples showing single crystalline-like slip lines indicate that plastic

deformation at the yield point largely occurred within the grains that span the entire width of lattice beams. We postulate that it is the size-dependent strengthening within the micron-scale single-crystalline regions of the lattice beams that elevates the strength of the mesolattice far above that of the bulk material. Another manifestation of this size effect is that for a given range of relative densities, the meso-lattices with 6  $\mu\text{m}$  unit cells are stronger than the meso-lattices with 8  $\mu\text{m}$  unit cells (Fig. 5.8). The lattice beams in the 6  $\mu\text{m}$  unit cell must be narrower than those in the 8  $\mu\text{m}$  unit cell to achieve the same relative density, so the size-dependent strength enhancement is greater for a smaller unit cell at a given relative density. For example, a  $\bar{\rho}$  of 0.54 corresponds to  $d = 1.6 \mu\text{m}$  in the 8  $\mu\text{m}$  unit cell and  $d = 1 \mu\text{m}$  in the 6  $\mu\text{m}$  unit cell where  $d$  is the width of the minor axis of the elliptical lattice beam.

Grain and twin boundaries present in the meso-lattices should also influence meso-lattice strength. Polycrystals with only a few grains across sample dimensions exhibit “smaller is weaker” behavior, which is caused by easier deformation along grain boundaries near surfaces in nano-sized grains<sup>39,54</sup>, and differing propensities for dislocation activity in surface vs. internal grains in micron-sized grains.<sup>48,73</sup> This “smaller is weaker” effect may be active near the grain boundaries in the meso-lattice and may be occurring simultaneously with the “smaller is stronger” effect in single crystalline regions. The amount of weakening in size-constrained polycrystals strongly depends on factors like the shape and orientation of the grains, stacking fault energy of the material and nature of the grain boundaries.<sup>36,54,131</sup> Similarly, strength and ductility of nano-twinned grains depends critically on spacing of the nanotwins and orientation of twinned planes relative to loading axis.<sup>38,81</sup> The effect of these microstructural features cannot be adequately predicted in the case of the meso-lattices without more precise knowledge of meso-lattice microstructure.

## 5.4 Structural vs. material size effects

A natural question arises: How much of the mechanical behavior in Cu meso-lattices can be attributed to the sample-size effect in micron-sized single crystalline metals and how much of it is due to structural topology? The sample size effect in single crystalline Cu with nonzero initial dislocation density has been thoroughly characterized in the nanoscale regime by Jennings et al.<sup>32,132</sup> and in the microscale range by Kiener et al.<sup>129,133</sup> These studies showed that shear strength resolved on the  $\langle 110 \rangle / \{111\}$  slip system,  $\tau$ , scaled logarithmically with sample size,  $D$ . The scaling law to quantify size effect in single crystalline fcc metals has been commonly expressed as:<sup>17</sup>

$$\frac{\tau}{\mu} = A \left( \frac{D}{b} \right)^m \quad (5.2)$$

where  $\mu$  is the shear modulus,  $b$  is the Burgers vector,  $A$  is 0.57 and  $m$  is -0.63 when the scaling law is fitted to nano-mechanical tests on Cu, Au, Ni and Al.  $A$  and  $m$  can vary slightly depending on experimental testing parameters such as sample fabrication methodologies, sample aspect ratios, and initial dislocation densities. Using this universal scaling law, the yield strength of a 1  $\mu\text{m}$ -sized Cu single crystal is found to be 512 MPa, which agrees well with the strengths reported from Cu micro-compression experiments<sup>133</sup> and is significantly higher than the shear stress of single crystal bulk Cu, 9.8 MPa.<sup>134</sup> Nanotwinned grains, which make up 9% by volume of the material, also contribute to the overall strength of the meso-lattices. A reasonable line of thinking would be to represent the bulk yield strength of the meso-lattices as the composite behavior of size-strengthened single crystalline and nanotwinned regions. We obtain the yield strength of nanotwinned regions by using the rule of mixtures to represent the yield strength of bulk Cu with a microstructure identical to that of the Cu meso-lattices as:

$$\sigma_{ys} = v_c \sigma_{c,ys} + v_{nt} \sigma_{nt,ys} \quad (5.3)$$

where  $\sigma_{ys}$  is the measured yield strength of the bulk Cu as obtained from thin film indentation (134 MPa),  $v_c$  is the volume fraction of crystalline grains,  $\sigma_{c,ys}$  is the yield strength of 2  $\mu\text{m}$  sized crystalline grains calculated using the Hall-Petch relation (101 MPa),  $v_{nt}$  is the volume fraction of nano-twinned regions, and  $\sigma_{nt,ys}$  is the yield strength of nano-twinned regions. Ion beam channeling images of the cross-section of the Cu thin film revealed that  $v_{ncnt}=0.09$ . Using Eq. 3,  $\sigma_{nt,ys}$  is calculated to be 458 MPa. This value is  $\sim 30\%$  higher than the yield strength previously measured by Jang et al. in 500 nm sized electroplated Cu nano-cylinders consisting of nanotwinned grains. This discrepancy is reasonable because the strength depends on twin spacing, orientation of twinned planes relative to the loading axis, and grain size to sample size ratio.<sup>38</sup>

Following this line of reasoning based on the rule of mixtures, a model for meso-lattice yield strength can be formulated. It is reasonable to assume that the individual beams that comprise the meso-lattices contain similar relative fractions of crystalline and nanotwinned regions as the Cu thin film. The relative fraction of the pore volume within the meso-lattices is  $1 - \bar{\rho}$ . The crystalline regions now show size-dependence because they mostly consist of single crystalline grains that span the width of the lattice. Size effect in strength manifests itself through the yield strength of the single crystalline regions within the lattice beams, which is assumed to scale with the minor axis length,  $d$ , of the elliptical lattice beam cross-sections (Eq. 5.2). The proximity of free surfaces to grain boundaries and twin boundaries and the resulting effect on meso-lattice strength is not taken into account in this analysis. The meso-lattice yield strength can then be represented as:

$$\sigma_{y,lat} = \bar{\rho}(v_c \sigma(d)_{c,ys} + v_{nt} \sigma_{nt,ys}) \quad (5.4)$$

$$\sigma_{y,lat} = \bar{\rho}(v_c \left( \frac{\mu A}{M} \left( \frac{d}{b} \right)^m \right) + v_{nt} \sigma_{nt,ys}) \quad (5.5)$$

Axial stress,  $\sigma$ , is related to shear stress,  $\tau$ , (Eq. 5.2) by the Schmid factor,  $M$ , which resolves the applied stress onto the slip planes for the fcc crystal.<sup>2</sup> The value of  $M$  used in Eq. 5 is taken to be that of the common fcc  $\langle 110 \rangle / \{111\}$  slip system.

An additional level of sophistication can be added to this model by considering structural effects on yield strength. Deshpande et al. derived the scaling relationship between yield strength and relative density for the octet structural geometry that deforms by plastic buckling.<sup>120</sup> We add the size-dependent strength in micro- and nanoscale lattice beams described in Eq. 5.5 to the octet yield strength equation:

$$\sigma_{y,oct} \approx 0.3 \bar{\rho} \sigma(d)_{ys} \quad (5.6)$$

$$\sigma_{y,oct} = 0.3 \bar{\rho} \left( v_c \left( \frac{\mu A}{M} \left( \frac{d}{b} \right)^m \right) + v_{nt} \sigma_{nt,ys} \right) \quad (5.7)$$

This relationship is plotted in Figure 5.9 for octet meso-lattices with 6  $\mu\text{m}$  and 8  $\mu\text{m}$  unit cells. This plot demonstrates two opposing effects on the overall strength of the lattices: (1) the yield strength of single crystalline region,  $\sigma(d)_{c,ys}$ , increases with decreasing relative density,  $\bar{\rho}$ , because lower  $\bar{\rho}$  corresponds to a lower  $d$  (i.e. narrower lattice beams) and (2) the size-independent yield strength of the octet structure,  $\sigma_{y,oct}$ , decreases linearly with  $\bar{\rho}$ . The yield strengths predicted by this model are lower for the structures with the 8  $\mu\text{m}$  unit cells than for the ones with 6  $\mu\text{m}$  unit cells over the same range of relative densities. This is consistent with the model because the smaller  $d$  at a given relative density leads to greater size-dependent strengthening in the 6  $\mu\text{m}$  unit cell structures.

Theoretical strengths obtained from Equations 5.5 (rule-of-mixtures) and 5.7 (octet lattice) are plotted together with the meso-lattice yield strengths in Figure 5.9 and appear to predict the correct order of magnitude for the yield stress, but otherwise do not describe the observed data particularly well. The octet lattice strength prediction (Eq. 5.7) matches more closely with the strengths of lower relative density meso-lattices, and the rule-of-mixtures formulation (Eq. 5.5) agrees more closely with higher relative density meso-lattices. These discrepancies may stem from the assumptions that are used in the formulation of each theory. The octet scaling relationship was derived for slender Timoshenko beams with large aspect ratios (small  $d/l$ ) connected at pin-jointed nodes. This scaling relationship was validated using experiment and finite element for circular beams for  $\bar{\rho}$  up to 0.5, but is inappropriate for high-relative density structures.<sup>120</sup> The meso-lattices are formed of elliptical beams with large  $d/l$  of 0.3 to 0.8 joined at rigid, solid nodes where significant local plasticity is observed during compression, which renders the assumptions of Timoshenko beams and pin-jointed nodes unrealistic. The observed deviation of experimental results from theory is exacerbated in high-relative density structures that contain lower aspect ratio lattice beams, which leads to a greater volume fraction of the lattice occupied by nodes. The nodes may have a different characteristic size than the lattice beams and may subsequently have a different size-dependent yield strength. The predicted scaling for the size-dependent octet structure with the 8  $\mu\text{m}$  unit cell matches experiment for lower relative densities,  $\bar{\rho} < 0.45$ , which is expected because these structures have the lowest volume fraction of nodes and the smallest  $d/l$ .

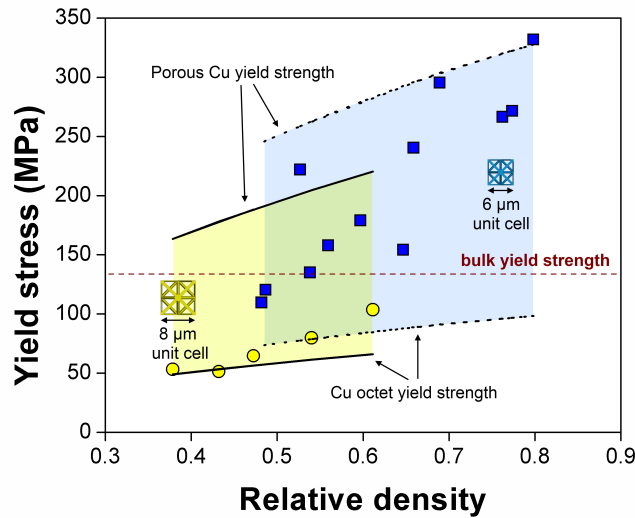


**Figure 5.9:** Yield strengths of meso-lattices (data points) compared to theoretically predicted yield strengths using the rule-of-mixtures scaling relationship for porous Cu (Equation 5.5) and the Cu octet scaling relationship (Equation 5.7). Blue square data points and shaded blue area bounded by dashed black lines correspond to an 8  $\mu\text{m}$  unit cell structure, and red circle data points and shaded red area bounded by solid black lines correspond to a 6  $\mu\text{m}$  unit cell structure, as shown schematically in the plot. Horizontal dashed line shows bulk yield strength.

The yield strength predicted by the rule of mixtures (Eq. 5.5) provides an upper bound for the meso-lattice yield strength. The predicted rule-of-mixtures yield strength for the 6  $\mu\text{m}$  unit cell approaches that of experiment at high relative density,  $\bar{\rho} = 0.8$ . Neither the rule-of-mixtures model nor the octet structural theory for yield strength considers the transition from porous to monolithic morphology, which corresponds to the conditions of high relative densities, marginal porosities, and wide lattice beams. Experimental exploration of a larger range of relative densities is necessary to fully populate the parameter space in the scaling of strength with relative density for the meso-porous solids. The analysis presented here is largely based on continuum theories and empirical findings and is not capable of quantifying and capturing the role of microstructural features like grain boundaries and defects, and their interaction with twin boundaries and free surfaces.

## 5.5 Ni meso-lattices

Ni octet meso-lattices were fabricated using the methods described in Chapter 5.2, with the exception of the use of an electroplating bath containing 240 g/l  $\text{NiSO}_4 \cdot \text{H}_2\text{O}$ , 45 g/l  $\text{NiCl}_2 \cdot 6\text{H}_2\text{O}$ , and 40 g/l  $\text{H}_3\text{BO}_3 \cdot 2\text{H}_2\text{O}$ . Ni meso-lattices were created with either 6  $\mu\text{m}$  or 8  $\mu\text{m}$ -wide unit cells, with side lengths of 24 to 24  $\mu\text{m}$  and heights of 17 to 20  $\mu\text{m}$  (Fig. 5.10). The minor axis of the elliptical lattice beam,  $d$ , ranged from 860 nm to 1.5  $\mu\text{m}$ .

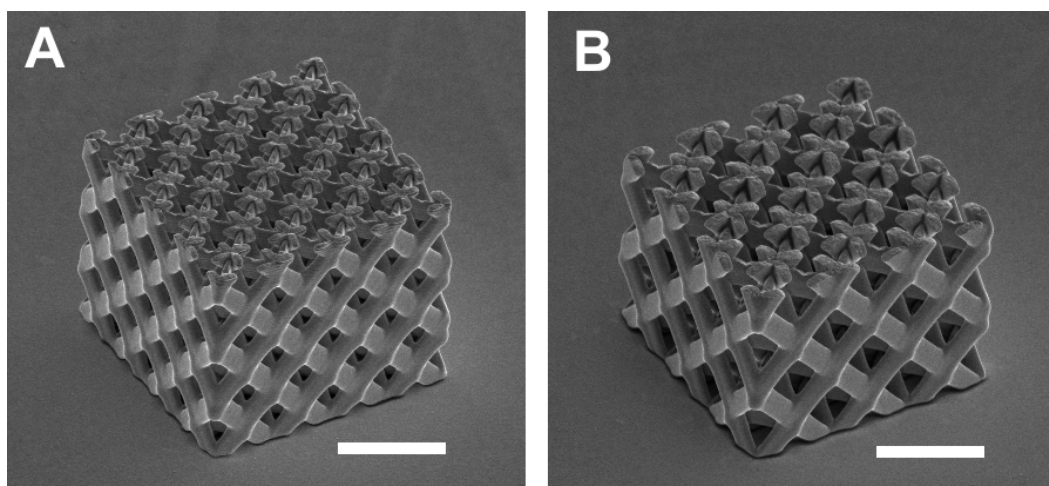


**Figure 5.10:** SEM images of Ni meso-lattices with (A) 6  $\mu\text{m}$  unit cell and (B) 8  $\mu\text{m}$  unit cell. Scale bars are 10  $\mu\text{m}$  in size.

Ni meso-lattice TEM samples were prepared according to the methods in Chapter 5.2. A protective layer of Pt was deposited on the meso-lattice using a scanning electron beam (FEI, Nova 600) prior to thinning lattice beams using focused ion beam. TEM microstructural analysis of 22 grains in two lattice beams revealed the average grain size in the Ni meso-lattices to be  $119 \pm 74$  nm, but sample thickness and interference between the magnetic field of the Ni sample and the transmission electron beam obscured some microstructural details (Fig. 5.11). Further TEM investigation is warranted to obtain a more accurate measurement of grain size.

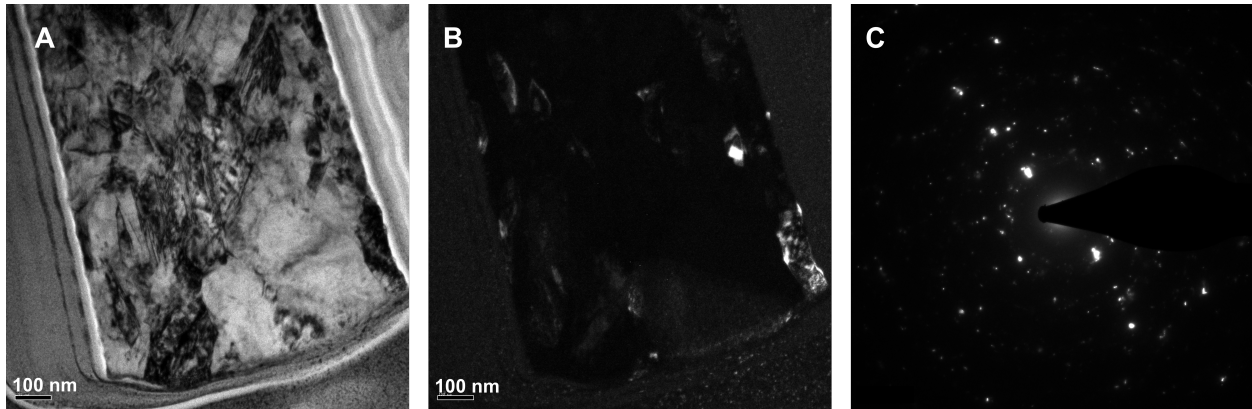


**Figure 5.11:** TEM images of Ni meso-lattice beam in (A) bright field mode, (B) dark field mode and (C) the corresponding diffraction pattern.

Uniaxial compression experiments were carried out on the Ni meso-lattices using the methods described in Chapter 5.2. One obstacle to obtaining meaningful Ni meso-lattice mechanical data was that the load limit of the nanoindenter used for micro-compressions was reached before the yield point of the meso-lattices for higher relative density lattices, as is shown in Figure 5.12a. Figure 5.12b shows the stress-strain response for meso-lattices with 8  $\mu\text{m}$  unit cell size and  $\bar{\rho}$  of 0.41 and 0.42, which had yield stresses of 412 and 436 MPa respectively.

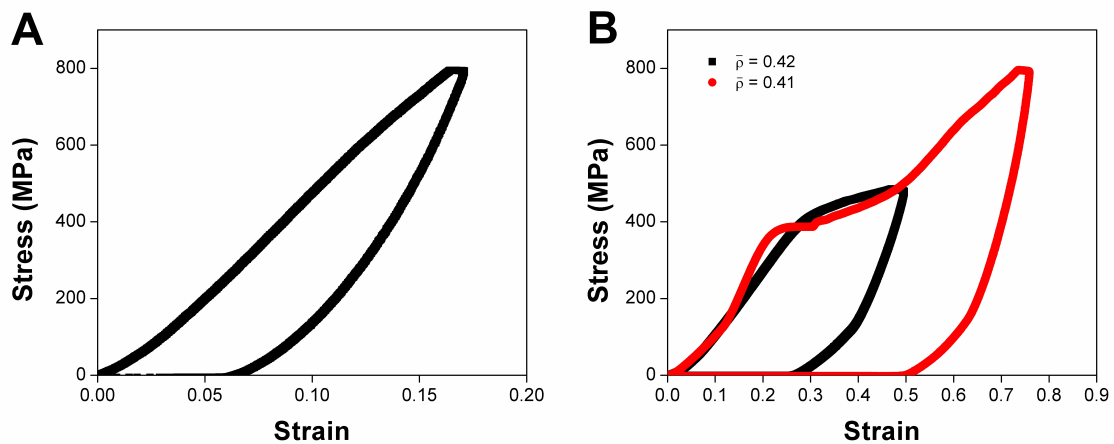


**Figure 5.12:** Stress-strain response of Ni meso-lattices with (A) 6  $\mu\text{m}$  unit cell and  $\bar{\rho} = 0.53$  (linear elastic loading and unloading only) and (B) 8  $\mu\text{m}$  unit cell size and  $\bar{\rho}$  of 0.41 and 0.42.

The yield strength of bulk electroplated Ni with similarly sized ( $\sim 100$  nm diameter) grains was found to be  $\sim 600$  MPa by Ebrahimi et al.<sup>135</sup> This bulk yield strength is higher than the measured Ni meso-lattice yield strengths shown in Figure 5.12b, but more meso-lattice mechanical data must be obtained for a larger range of  $\bar{\rho}$  and unit cell size before conclusions are drawn about dependence of Ni meso-lattice strength on structural geometry or microstructure.

## 5.6 Summary

We developed a fabrication process for monolithic 3D Cu lattices with structural (unit cell size) and microstructural (grain size) features on the micron-scale. Compression experiments on meso-lattices with  $\bar{\rho} > 0.5$  and  $6 \mu\text{m}$  unit cell size revealed strengths that were 1.8 times higher than that of monolithic bulk Cu. We deduce that the single crystalline regions in the lattice beams exhibit the “smaller is stronger” size effect which elevates the overall structural strength of the meso-lattice. These findings may have significant implications for the processing of engineering metals and alloys for structural purposes. For example, Cu meso-lattices have similar densities ( $\sim 4.5 \text{ kg/m}^3$ ) and strengths ( $\sim 350$  MPa) as lightweight Ti-based alloys but maintain the intrinsic material properties of Cu, such as electrical and thermal conductivity.<sup>115</sup> Porous metallic nanostructures are also of great interest in catalysis, as battery electrodes, and in photonic devices.<sup>136-138</sup> Some of these applications require mechanical stability for prolonged operation during chemical, electrochemical or mechanical cycling, which could be aided by using principles from cellular solids in combination with size-dependent strengthening. This work demonstrates that removing material from a monolithic metal block and architecting it into

a 3D meta-material with microscale features, while maintaining a well-defined microstructure, provides a pathway to attaining high strength, low-density structural materials.

The meso-lattice fabrication process is versatile enough to accommodate many metals, which we show by fabricating Ni meso-lattices with similar geometry to the Cu meso-lattices. The Ni meso-lattices have an average grain size of 119 nm, which means that lattice beams are likely to be spanned by many grains, unlike in the case of the Cu meso-lattices. Preliminary mechanical results showed that Ni mesolattices with 8  $\mu\text{m}$  unit cell size and  $\bar{\rho}$  of 0.41 and 0.42 had yield strengths that are 30% lower than the bulk yield strength of electroplated Ni with similar microstructure. It is of interest to compare the behavior of the Ni and Cu meso-lattices in order to gauge the effect of materials chemistry and microstructure. For example, the Ni meso-lattice is not expected to exhibit the “smaller is stronger” size effect because its microstructure does not consist of grains large enough to span the lattice beams. Scaling of Ni meso-lattice strength with  $\bar{\rho}$  is expected to follow the size-independent octet scaling law more closely (assuming Ni meso-lattice microstructure is the same for different  $\bar{\rho}$ ), and can be contrasted with Cu meso-lattice strength scaling in order to separate the effects of structural topology and materials size effects. More mechanical tests must be performed on Ni meso-lattices before meaningful conclusions can be made.

## Chapter 6. *In-situ* SEM Lithiation of 3D Architected

### Si Nano-Electrodes

#### 6.1 Introduction

Li-ion batteries are among the most important portable energy sources today, because of their high energy density, longevity and ability to be recharged. Li-ion batteries are used in a majority of consumer electronics, and are a popular proposed alternative to fossil fuels for powering vehicles but do not yet meet the low cost, high energy density and safety requirements for widespread application in the transportation sector. Silicon is of great interest as an anode material for Li-ion batteries because it has the highest known storage capacity for Li (up to 4200 mAh/g).<sup>139</sup> For comparison, commercially available Li-ion batteries use a graphitic carbon anode with a capacity of 370 mAh/g. A major obstacle to use of Si in Li-ion batteries is the mechanical degradation experienced by Si during battery operation. Si can experience a volumetric change of up to ~400% during battery cycling which leads to capacity fade because of large stresses and fracture within the electrode, or delamination at the interface of the Si electrode and current collector (typically Cu) in the case of thin film electrodes.<sup>139-142</sup>

A proven strategy for improving the mechanical reliability of Si electrodes has been to reduce electrode dimensions to the nanoscale. One early approach using this technique was to consolidate Si nanoparticles into a thin film electrode, which resulted in high reversible capacities (2000 mAh/g) for tens of cycles.<sup>143</sup> Nanoscale Si in the form of ~100 nm wide CVD-grown Si nanowires was shown to undergo ductile deformation during lithiation and delithiation,

instead of the brittle fracture typical of macroscale Si.<sup>31,144</sup> This nanoscale brittle-to-ductile size effect can be used in combination with hierarchical assembly of nanoscale electrode materials for further improvement in electrode performance. For instance, Ni-Si inverse opal lattices and C-Si porous nanocomposites have excellent cycleability because open spaces within the structures are used to accommodate Si volume change.<sup>145,146</sup> These porous nanocomposites have high rate capabilities because of close contact between Si, a conductive scaffold current collector and the Li-transporting electrolyte, and short diffusion distances within these components. Besides mechanical degradation, a major issue that reduces capacity in many Si electrodes for Li-ion batteries is that parasitic chemical reactions on the electrode surface lead to the formation of an insulating solid electrolyte interface (SEI).<sup>139</sup> This chemical reactivity problem has also been addressed using hierarchical structures by creating nanoparticles in which a Si core is free to expand within a protective hollow C shell such that a SEI layer is not formed on the Si.<sup>147</sup>

Further improvements to electrode mechanical and electrochemical performance could be obtained through use of structural architecture, in addition to the previously described appropriate choices of materials chemistry and length scales. Architecture in solid lattices and foams is commonly used to control mechanical strength and fracture<sup>115,118,119</sup>, and even volume expansion such as in the cases of auxetic (negative Poisson ratio) and zero thermal expansivity lattices.<sup>148,149</sup> It is possible that both volume expansion in Si electrodes and transport of electrolyte through the electrode could be controlled through careful choice of structural architecture. Electrode structures have typically been limited to simple geometries such as thin films, wires or spherical particles connected by a conductive binder, or geometries dictated by self-assembled templates (e.g. inverse opal structure). Here, we demonstrate the use of solid metallic meso-lattices coated in Si as electrodes for Li-ion batteries. The fabrication method used

to make the meso-lattices allows structural control at length scales from microstructural to structural, and the exploration of the relationship between electrode structure and electrochemical performance.

An *in-situ* SEM lithiation stage was developed to observe nanoscale changes in electrode structural morphology during battery cycling and correlate these changes to electrochemical behavior. This technique is analogous to the use of *in-situ* TEM electrochemical cells, which have been used to observe microstructural changes during lithiation in SnO<sub>2</sub> wires<sup>150</sup> and Si wires and spheres.<sup>151-153</sup> Compared to *in-situ* TEM, *in-situ* SEM lithiation lacks the ability to directly image electrode microstructure, but has a larger field of view and the ability to differentiate volume changes into and out of the direction of the e-beam. *In-situ* SEM has been successfully used by other research groups to observe morphological changes in Li-ion battery anodes with disordered structures<sup>154,155</sup>, and the growth of Li dendrites against a solid polymer electrolyte.<sup>156</sup>

## 6.2 Fabrication, characterization and electrochemical testing

Si nano-electrodes consist of a 3D architected Ni octet meso-lattice coated with Si using room temperature RF magnetron sputtering (Fig. 6.1a). Ni meso-lattices are fabricated on top of an ITO-covered glass slide using the method described in Chapter 5.2, and serve as a mechanically robust and electrically conductive scaffold for Si. The ITO is used as the current collector for the Si electrode during electrochemical testing. SEM imaging of the lattices before and after Si sputtering was used to estimate the Si thickness to be around 500 nm (Fig. 6.1b,c).

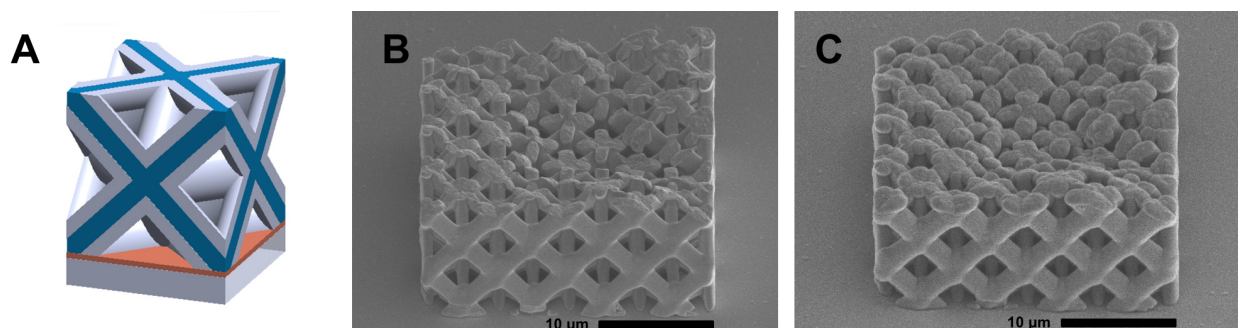


**Figure 6.1** (A) Schematic of Ni meso-lattice unit cell (blue) coated in Si (silver) fabricated on an ITO thin film on glass. SEM images of electroplated Ni meso-lattice (B) before and (C) after Si sputtering.

An electrochemical cell was built inside a SEM to enable observation of morphological changes in the Si electrode during electrochemical cycling versus a Li electrode (Figure 6.2). This Li metal serves as both the reference and counter electrode, and is mounted on a telescoping mechanical arm that extends into the SEM vacuum chamber. The Si electrode was placed on the sample stage, and oriented such that the scanning electron beam is aimed at one sidewall of the Si electrode. A layer of  $\text{Li}_x\text{O}_x\text{N}_x$  is formed spontaneously on the Li electrode when the Li electrode is transported from an argon environment through air into the SEM (exposure to air is less than 3 minutes). This oxide layer serves as a solid electrolyte. Electrochemical testing was conducted by contacting the  $\text{Li}_x\text{O}_x\text{N}_x$  to the Si electrode, and applying a -4V potential to induce lithiation and a +4V potential to cause delithiation. We ensured that the Si electrode is not penetrating the  $\text{Li}_x\text{O}_x\text{N}_x$  layer and directly contacting the Li metal by checking that lithiation does not occur spontaneously when the Li/ $\text{Li}_x\text{O}_x\text{N}_x$ /Si stack is formed, but requires an applied potential to proceed.

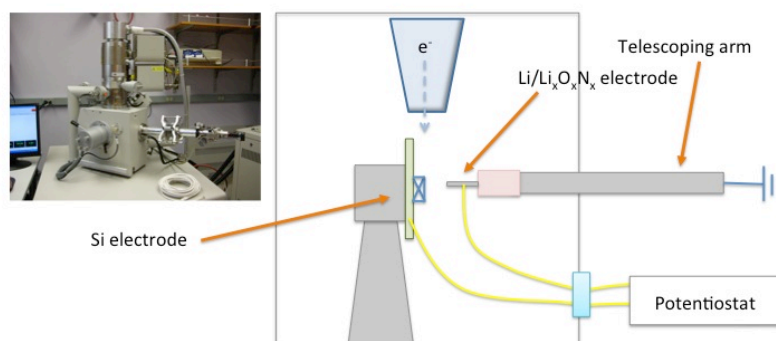


**Figure 6.2** Photo of SEM with telescoping mechanical arm and schematic of the SEM chamber with the lithiation stage assembled. The Si electrode is mounted on the SEM stage opposite the Li electrodes and solid electrolyte. The Li electrode/electrolyte is brought into contact with the Si electrode, and a bias is applied between the two electrodes to perform electrochemical testing.

Accurate measurement of electrical potential across the cell proved impossible when using the  $\text{Li}_x\text{O}_x\text{N}_x$  electrolyte. Other researchers have encountered this issue when using ultra-thin solid electrolytes such as  $\text{Li}_x\text{O}_x\text{N}_x$  and LIPON in nanobatteries.<sup>151,153,157</sup> It is not clear why this problem occurs, but the thin solid electrolyte is typically poorly characterized, and may change compositionally or structurally during electrochemical cycling. Electrochemical cycling was also performed using an ionic liquid electrolyte in place of the solid oxide electrolyte in order to obtain accurate battery cycling data on the Ni-Si meso-lattices (Fig. 6.3). The ionic liquid electrolyte consists of 10 wt% lithium bis(trifluoromethylsulfonyl) imide (LiTFSI) in 1-butyl-1-methylpyrrolidinium bis(trifluoromethylsulfonyl) imide ( $\text{P}_{14}\text{TFSI}$ ).<sup>152</sup> Capillary action draws the ionic liquid electrolyte into the Si meso-lattice such that the liquid contacts every surface of the meso-lattice. It may be possible to observe morphological changes in the Si electrode during electrochemical cycling using the ionic liquid electrolyte, but the ionic liquid sometimes obscures features of the Si electrode by forming a droplet around the Si electrode.

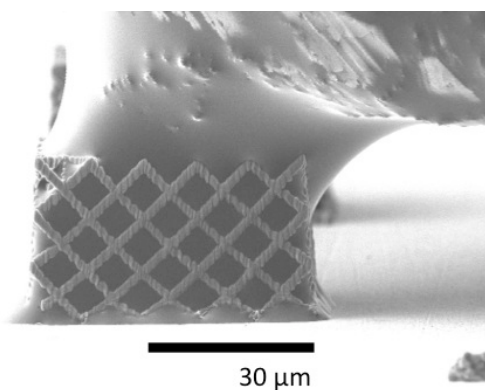


**Figure 6.3** SEM image of Si electrode in contact with ionic liquid electrolyte, which is in contact with the Li electrode (top right in image).

### 6.3 Results

The Ni-Si meso-lattice electrode was lithiated galvanostatically for 6.5 hours using the solid electrolyte (Fig. 6.4). The main observations from this electrochemical test were that fracture occurs at the top surface of the meso-lattice, bulging occurs at nodes in the structure, and volume expansion occurs into the pores in the meso-lattice rather than significantly changing the overall volume of the structure. Careful analysis of the electrode shown in Figure 6.4 showed that the overall structure expanded by 3% in width and 13% in height during lithiation. A significant amount of the increase in height is due to a large amount of expansion at the top surface of the meso-lattice, where mushroom cap-like shapes form and subsequently fracture. It was found that ionic transport of Li through the Si electrode is kinetically limiting at the applied current because the top row of lattice beams in the meso-lattice (marked by red box in Figure 6.4) expands in volume more than does the bottom row (blue box in Figure 6.4). The top row of beams increases by a Si layer thickness of 180 nm which corresponds to a 73% increase in volume, and the bottom row of beams increases by 90 nm which corresponds to a 56% increase in volume.

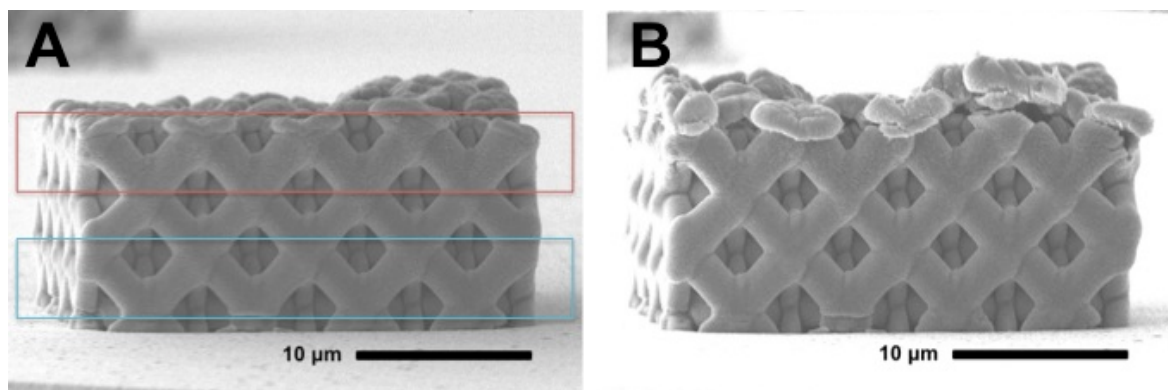


**Figure 6.4** SEM images of Ni-Si meso-lattice electrode (A) before and (B) after galvanostatic lithiation for 6.5 hours. Red box demarcates volume in which Si expanded by 73% and blue box demarcates volume in which Si expanded by 56%.

The feasibility of *in-situ* SEM cyclic lithiation using the ionic liquid electrolyte was evaluated by performing cyclic voltammetry of the ionic liquid on a sputtered Si thin film versus the Li metal electrode. Cyclic voltammetry was used to identify the electrochemical stability window of the ionic liquid (0V to 5V), and ensure that lithiation and delithiation repeatedly occur at the expected potentials. Figure 6.5 shows a cyclic voltammogram (CV) performed at 10 mV/s on a Si thin film in which the onset of lithiation occurs at  $\sim 0.3$  V and delithiation starts at  $\sim 0.3$  V on the reverse sweep. The shape of the CV matches that reported in the literature for cyclic voltammetry of Li versus Si in a Li-transporting electrolyte.<sup>158</sup>

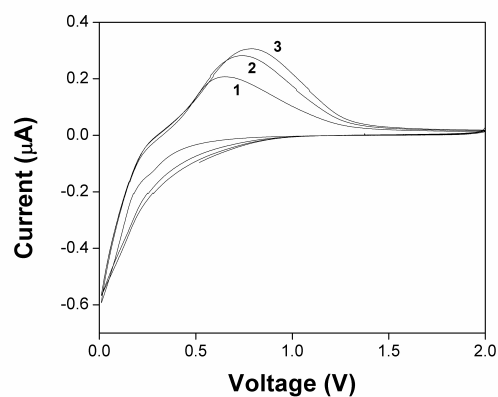


**Figure 6.5** Cyclic voltammogram of Si thin film versus Li metal in ionic liquid electrolyte. Sweep rate is 50 mV/s. Three cycles were performed and are labeled on the plot.

## 6.4 Ongoing work

Cyclic lithiation of Si meso-lattice electrodes using both the solid electrolyte and liquid electrolyte must be completed before useful conclusions can be drawn about the influence of structural geometry on electrode performance. Towards this end, we are working on optimizing the Si meso-lattice fabrication process for effective electrochemical cycling. Plasma-enhanced chemical vapor deposition (PECVD) is being used to deposit a conformal layer of Si on the metallic meso-lattice. RF magnetron sputtering is ideal for depositing thin films on flat substrates because sputtering is considered to be a line-of-sight technique in which sputtered ions travel in from the target to land on the substrate. Sputtering on a substrate with a complex geometry tends to result in thicker deposits on the sides of the substrate facing the target and thinner or no deposit on the parts of the substrate facing away from the target. Conformal sputtering of a metal with thickness of  $\sim 90$  nm has been demonstrated on low density 3D polymer nano-lattices<sup>127</sup>, but sputtering Si with thickness of hundreds of nanometers on similar polymer nano-lattices has resulted in coatings with tapered thicknesses in which the top edges of lattice beams have more deposited material than do the bottom edges (Fig. 6.6a). PECVD has the additional benefit of being able to deposit on 3D structures with dense features or small pore sizes; dense features will be required for the Si meso-lattices to achieve high energy density. PECVD conditions of 1 Torr of SiH<sub>4</sub>/Ar gas deposited at 200°C at a nominal rate of 25 nm/min were used to achieve the Si deposition shown in Figure 6.6b. TEM will be used to identify the microstructure of the Si as crystalline or amorphous.

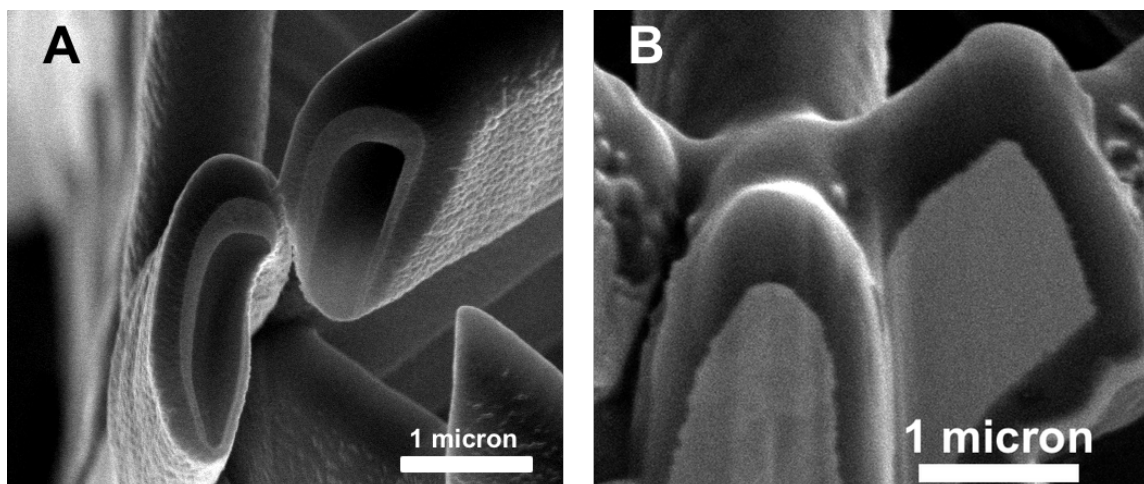


**Figure 6.6** SEM images of (A) sputtered deposited Si on Cu coating on polymer nano-lattice and (B) PECVD deposited Si coated on solid Cu meso-lattice.

A second area of ongoing research involves the computational modeling and optimization of Si meso-lattice electrodes. Finite element modeling (FEM) is being used to guide the design of the Si meso-lattice electrodes and simulate the stress state within the electrodes. One goal of FEM is to identify the stress level and state-of-charge at which the Si coating will separate from the underlying metallic structure because the coating is expanding in volume but the metal is not expanding. Another goal of FEM is to computationally explore different structural geometries and identify ones which are mechanically robust during electrochemical cycling, and which have high energy density. FEM is being performed in collaboration with Professor Michael Ortiz and Sarah Mitchell.

## Bibliography

- (1) Hirth, J. P.; Lothe, J. *Theory of Dislocations*; Krieger Publishing Co., 1992.
- (2) Hull, D.; Bacon, D. J. *Introduction to Dislocations*; Fourth ed.; Butterworth Heinemann: Boston, 2001.
- (3) Courtney, T. H. *Mechanical Behavior of Materials*; Waveland Pr Inc., 2005.
- (4) Kumar, K. S.; Van Swygenhoven, H.; Suresh, S. *Acta Mater.* **2003**, *51*, 5743.
- (5) Bobylev, S. V.; Ovid'ko, I. A. *Phys. Rev. Lett.* **2012**, *109*.
- (6) Hasnaoui, A.; Van Swygenhoven, H.; Derlet, P. M. *Science* **2003**, *300*, 1550.
- (7) Schuh, C. A.; Hufnagel, T. C.; Ramamurty, U. *Acta Mater.* **2007**, *55*, 4067.
- (8) Argon, A. S.; Kuo, H. Y. *Materials Science and Engineering* **1979**, *39*, 101.
- (9) Spaepen, F. *Acta Metallurgica* **1977**, *25*, 407.
- (10) Conner, R. D.; Johnson, W. L.; Paton, N. E.; Nix, W. D. *J. Appl. Phys.* **2003**, *94*, 904.
- (11) Conner, R. D.; Li, Y.; Nix, W. D.; Johnson, W. L. *Acta Mater.* **2004**, *52*, 2429.
- (12) Griffith, A. A. *Philosophical Transactions of the Royal Society of London* **1920**, *221*, 163.
- (13) Hertzberg, R. W. *Deformation and Fracture Mechanics of Engineering Materials*; Wiley, 1995.
- (14) Hall, E. O. *Proceedings of the Physical Society of London Section B* **1951**, *64*, 747.
- (15) Petch, N. J. *Journal of the Iron and Steel Institute* **1953**, *174*, 25.
- (16) Uchic, M. D.; Shade, P. A.; Dimiduk, D. M. In *Annual Review of Materials Research*; Annual Reviews: Palo Alto, 2009; Vol. 39, p 361.
- (17) Greer, J. R.; De Hosson, J. T. M. *Prog. Mater. Sci.* **2011**, *56*, 654.
- (18) Brenner, S. S. *J. Appl. Phys.* **1956**, *27*, 1484.
- (19) Uchic, M. D.; Dimiduk, D. M.; Florando, J. N.; Nix, W. D. *Science* **2004**, *305*, 986.
- (20) Greer, J. R.; Oliver, W. C.; Nix, W. D. *Acta Mater.* **2005**, *53*, 1821.
- (21) Dimiduk, D. M.; Woodward, C.; LeSar, R.; Uchic, M. D. *Science* **2006**, *312*, 1188.
- (22) Rao, S. I.; Dimiduk, D. M.; Parthasarathy, T. A.; Uchic, M. D.; Tang, M.; Woodward, C. *Acta Mater.* **2008**, *56*, 3245.
- (23) Lai, A.; Du, Z. H.; Gan, C. L.; Schuh, C. A. *Science* **2013**, *341*, 1505.
- (24) Jang, D. C.; Greer, J. R. *Nat Mater* **2010**, *9*, 215.
- (25) Volkert, C. A.; Donohue, A.; Spaepen, F. *J. Appl. Phys.* **2008**, *103*.
- (26) Beaber, A. R.; Nowak, J. D.; Ugurlu, O.; Mook, W. M.; Girshick, S. L.; Ballarini, R.; Gerberich, W. W. *Philosophical Magazine* **2011**, *91*, 1179.
- (27) Schwiedrzik, J.; Raghavan, R.; Burki, A.; LeNader, V.; Wolfram, U.; Michler, J.; Zysset, P. *Nat Mater* **2014**, *13*.
- (28) Kim, J. Y.; Jang, D. C.; Greer, J. R. *Scr. Mater.* **2009**, *61*, 300.
- (29) Lilleodden, E. *Scr. Mater.* **2010**, *62*, 532.
- (30) Biener, J.; Hodge, A. M.; Hayes, J. R.; Volkert, C. A.; Zepeda-Ruiz, L. A.; Hamza, A. V.; Abraham, F. F. *Nano Lett* **2006**, *6*, 2379.
- (31) Chan, C. K.; Peng, H. L.; Liu, G.; McIlwrath, K.; Zhang, X. F.; Huggins, R. A.; Cui, Y. *Nat. Nanotechnol.* **2008**, *3*, 31.
- (32) Jennings, A. T.; Burek, M. J.; Greer, J. R. *Phys. Rev. Lett.* **2010**, *104*, 135503.
- (33) Buzzi, S.; Dietiker, M.; Kunze, K.; Spolenak, R.; Loffler, J. F. *Philosophical Magazine* **2009**, *89*, 869.

- (34) Diao, J. K.; Gall, K.; Dunn, M. L.; Zimmerman, J. A. *Acta Mater.* **2006**, *54*, 643.
- (35) Schuster, B. E.; Wei, Q.; Zhang, H.; Ramesh, K. T. *Appl. Phys. Lett.* **2006**, *88*, 103112.
- (36) Kunz, A.; Pathak, S.; Greer, J. R. *Acta Mater.* **2011**, *59*, 4416.
- (37) Guo, Q.; Greer, J. R. *Scr. Mater.* **2012**, *66*, 272.
- (38) Jang, D. C.; Cai, C.; Greer, J. R. *Nano Lett* **2011**, *11*, 1743.
- (39) Jang, D. C.; Greer, J. R. *Scr. Mater.* **2011**, *64*, 77.
- (40) Rinaldi, A.; Peralta, P.; Friesen, C.; Sieradzki, K. *Acta Mater.* **2008**, *56*, 511.
- (41) Jahed, Z.; Jin, S. M.; Burek, M. J.; Tsui, T. Y. *Mater. Sci. Eng. A-Struct. Mater. Prop. Microstruct. Process.* **2012**, *542*, 40.
- (42) Mara, N. A.; Bhattacharyya, D.; Dickerson, P.; Hoagland, R. G.; Misra, A. *Appl. Phys. Lett.* **2008**, *92*, 231901.
- (43) Jang, D.; Li, X.; Gao, H.; Greer, J. R. *Nat Nanotechnol* **2012**, *7*, 594.
- (44) Lian, J.; Jang, D.; Valdevit, L.; Schaedler, T. A.; Jacobsen, A. J.; Carter, W. B.; Greer, J. R. *Nano Lett* **2011**, *11*, 4118.
- (45) Hansen, N. *Acta Metallurgica* **1977**, *25*, 863.
- (46) Miyazaki, S.; Shibata, K.; Fujita, H. *Acta Metallurgica* **1979**, *27*, 855.
- (47) Janssen, P. J. M.; de Keijser, T. H.; Geers, M. G. D. *Mater. Sci. Eng. A-Struct. Mater. Prop. Microstruct. Process.* **2006**, *419*, 238.
- (48) Yang, B.; Motz, C.; Rester, M.; Dehm, G. *Philosophical Magazine* **2012**, *92*, 3243.
- (49) Rupert, T. J.; Gianola, D. S.; Gan, Y.; Hemker, K. J. *Science* **2009**, *326*, 1686.
- (50) Shan, Z. W.; Stach, E. A.; Wieszorek, J. M. K.; Knapp, J. A.; Follstaedt, D. M.; Mao, S. X. *Science* **2004**, *305*, 654.
- (51) Asaro, R. J.; Krysl, P.; Kad, B. *Philos. Mag. Lett.* **2003**, *83*, 733.
- (52) Van Swygenhoven, H.; Derlet, P. A. *Phys. Rev. B* **2001**, *64*, 224105.
- (53) Tian, N.; Zhou, Z. Y.; Sun, S. G.; Ding, Y.; Wang, Z. L. *Science* **2007**, *316*, 732.
- (54) Gu, X. W.; Loynachan, C. N.; Wu, Z. X.; Zhang, Y. W.; Srolovitz, D. J.; Greer, J. R. *Nano Lett* **2012**, *12*, 6385.
- (55) Burek, M. J.; Greer, J. R. *Nano Lett* **2010**, *10*, 69.
- (56) Yarden, T. S.; Joselevich, E. *Nano Lett* **2010**, *10*, 4742.
- (57) Penner, R. M.; Martin, C. R. *Anal. Chem.* **1987**, *59*, 2625.
- (58) Oliver, W. C.; Pharr, G. M. *J. Mater. Res.* **1992**, *7*, 1564.
- (59) Nix, W. D., Private communication.
- (60) Zhang, H.; Schuster, B. E.; Wei, Q.; Ramesh, K. T. *Scr. Mater.* **2006**, *54*, 181.
- (61) Dalla Torre, F.; Van Swygenhoven, H.; Victoria, M. *Acta Mater.* **2002**, *50*, 3957.
- (62) Sanders, P. G.; Eastman, J. A.; Weertman, J. R. *Acta Mater.* **1997**, *45*, 4019.
- (63) Jonnalagadda, K. N.; Chasiotis, I.; Yagnamurthy, S.; Lambios, J.; Pulskamp, J.; Polcawich, R.; Dubey, M. *Proc. Soc. Exp. Mech.* **2010**, *67*, 25.
- (64) Trelewicz, J. R.; Schuh, C. A. *Acta Mater.* **2007**, *55*, 5948.
- (65) Wu, Z. X.; Zhang, Y. W.; Srolovitz, D. J. *Acta Mater.* **2011**, *59*, 6890.
- (66) Plimpton, S. J. *Comput. Phys.* **1995**, *117*, 1.
- (67) Sheng, H. W.; Kramer, M. J.; Cadien, A.; Fujita, T.; Chen, M. W. *Phys. Rev. B* **2011**, *83*, 134118.
- (68) Wu, Z. X.; Zhang, Y. W.; Jhon, M. H.; Gao, H. J.; Srolovitz, D. J. *Nano Lett* **2012**, *12*, 910.
- (69) Nose, S. *J. Chem. Phys.* **1984**, *81*, 511.
- (70) Nose, S. *Mol. Phys.* **1984**, *52*, 255.

- (71) Hoover, W. G. *Phys. Rev. A* **1986**, *34*, 2499.
- (72) Melchionna, S.; Ciccotti, G.; Holian, B. L. *Mol. Phys.* **1993**, *78*, 533.
- (73) Molotnikov, A.; Lapovok, R.; Davies, C. H. J.; Cao, W.; Estrin, Y. *Scr. Mater.* **2008**, *59*, 1182.
- (74) Malygin, G. A. *Phys. Solid State* **2012**, *54*, 559.
- (75) Currey, J. D. *Proceedings of the Royal Society B-Biological Sciences* **1977**, *196*, 443.
- (76) Fratzl, P.; Weinkamer, R. *Prog. Mater. Sci.* **2007**, *52*, 1263.
- (77) Yu, M. F. L., O.; Dyer, M. J.; Moloni, K.; Kelly, T. F.; Ruoff, R. S. *Science* **2000**, 287, 637.
- (78) Lee, C.; Wei, X. D.; Kysar, J. W.; Hone, J. *Science* **2008**, *321*, 385.
- (79) Garel, J. L.; Levin, I.; Zhi, C. Y.; Nagapriya, K. S.; Popovitz-Biro, R.; Golberg, D.; Bando, Y.; Hod, O.; Joselevich, E. *Nano Lett* **2012**, *12*, 6347.
- (80) Bertolazzi, S.; Brivio, J.; Kis, A. *ACS Nano* **2011**, *5*, 9703.
- (81) Lu, L.; Chen, X.; Huang, X.; Lu, K. *Science* **2009**, 323, 607.
- (82) Vigolo, B.; Penicaud, A.; Coulon, C.; Sauder, C.; Pailler, R.; Journet, C.; Bernier, P.; Poulin, P. *Science* **2000**, *290*, 1331.
- (83) Hao, S.; Cui, L.; Jiang, D.; Han, X.; Ren, Y.; Jiang, J.; Liu, Y.; Liu, Z.; Mao, S.; Wang, Y.; Li, Y.; Ren, X.; Ding, X.; Wang, S.; Yu, C.; Shi, X.; Du, M.; Yang, F.; Zheng, Y.; Zhang, Z.; Li, X.; Brown, D. E.; Li, J. *Science (New York, N.Y.)* **2013**, 339, 1191.
- (84) Dugdale, D. S. *J. Mech. Phys. Solids* **1960**, *8*, 100.
- (85) Gao, H. J.; Ji, B. H.; Jager, I. L.; Arzt, E.; Fratzl, P. *Proc. Natl. Acad. Sci. U. S. A.* **2003**, *100*, 5597.
- (86) Giesa, T.; Pugno, N. M.; Buehler, M. J. *Physical Review E* **2012**, *86*, 041902.
- (87) Kumar, S.; Li, X. Y.; Haque, A.; Gao, H. J. *Nano Lett* **2011**, *11*, 2510.
- (88) Zhang, T.; Li, X. Y.; Kadkhodaei, S.; Gao, H. J. *Nano Lett* **2012**, *12*, 4605.
- (89) Khare, R.; Mielke, S. L.; Paci, J. T.; Zhang, S. L.; Ballarini, R.; Schatz, G. C.; Belytschko, T. *Phys. Rev. B* **2007**, *75*, 075412.
- (90) Mielke, S. L.; Troya, D.; Zhang, S.; Li, J. L.; Xiao, S. P.; Car, R.; Ruoff, R. S.; Schatz, G. C.; Belytschko, T. *Chem. Phys. Lett.* **2004**, *390*, 413.
- (91) Kumar, S.; Haque, M. A.; Gao, H. *Appl. Phys. Lett.* **2009**, *94*, 253104
- (92) Wurster, S.; Motz, C.; Pippan, R. *Philosophical Magazine* **2012**, *92*, 1803.
- (93) Iqbal, F.; Ast, J.; Goken, M.; Durst, K. *Acta Mater.* **2012**, *60*, 1193.
- (94) Kupka, D.; Lilleodden, E. T. *Experimental Mechanics* **2012**, *52*, 649.
- (95) Gu, X. W.; Wu, Z. X.; Zhang, Y. W.; Srolovitz, D. J.; Greer, J. R. *Nano Lett* **2013**, *13*, 5703.
- (96) Wilson, C. D.; Landes, J. D. *Fracture toughness testing with notched round bars*; ASTM STP 1360, 2000; Vol. 30.
- (97) Kelchner, C. L.; Plimpton, S. J.; Hamilton, J. C. *Phys. Rev. B* **1998**, *58*, 11085.
- (98) Faken, D.; Jonsson, H. *Computational Materials Science* **1994**, *2*, 279.
- (99) Chen, D. Z.; Jang, D.; Guan, K. M.; An, Q.; Goddard, W. A., 3rd; Greer, J. R. *Nano Lett* **2013**, *13*.
- (100) Magagnosc, D. J.; Ehrbar, R.; Kumar, G.; He, M. R.; Schroers, J.; Gianola, D. S. *Scientific Reports* **2013**, *3*.
- (101) Hofmann, D. C.; Suh, J. Y.; Wiest, A.; Duan, G.; Lind, M. L.; Demetriou, M. D.; Johnson, W. L. *Nature* **2008**, *451*, 1085.
- (102) Ritchie, R. O. *Nat Mater* **2011**, *10*, 817.

- (103) Qu, R. T.; Calin, M.; Eckert, J.; Zhang, Z. F. *Scr. Mater.* **2012**, *66*, 733.
- (104) Sha, Z. D.; Pei, Q. X.; Sorkin, V.; Branicio, P. S.; Zhang, Y. W.; Gao, H. J. *Appl. Phys. Lett.* **2013**, *103*.
- (105) Ackland, G.; Mendeleev, M.; Srolovitz, D.; Han, S.; Barashev, A. *Journal of Physics: Condensed Matter* **2004**, *16*, S2629.
- (106) Verlet, L. *Phys. Rev.* **1967**, *159*, 98.
- (107) Nosé, S. *The Journal of Chemical Physics* **1984**, *81*, 511.
- (108) Hoover, W. G. *Phys. Rev. A* **1985**, *31*, 1695.
- (109) Štich, I.; Car, R.; Parrinello, M.; Baroni, S. *Phys. Rev. B* **1989**, *39*, 4997.
- (110) Murali, P.; Guo, T. F.; Zhang, Y. W.; Narasimhan, R.; Li, Y.; Gao, H. J. *Phys. Rev. Lett.* **2011**, *107*, 215501.
- (111) Shimizu, F.; Ogata, S.; Li, J. *Materials transactions* **2007**, *48*, 2923.
- (112) Stukowski, A. *Modell. Simul. Mater. Sci. Eng.* **2010**, *18*, 015012.
- (113) Needleman, A. *J. Appl. Mech.-Trans. ASME* **1987**, *54*, 525.
- (114) Seppala, E. T.; Belak, J.; Rudd, R. E. *Phys. Rev. B* **2004**, *69*.
- (115) Fleck, N. A.; Deshpande, V. S.; Ashby, M. F. *Proceedings of the Royal Society a-Mathematical Physical and Engineering Sciences* **2010**, *466*, 2495.
- (116) Hao, S. J.; Cui, L. S.; Jiang, D. Q.; Han, X. D.; Ren, Y.; Jiang, J.; Liu, Y. N.; Liu, Z. Y.; Mao, S. C.; Wang, Y. D.; Li, Y.; Ren, X. B.; Ding, X. D.; Wang, S.; Yu, C.; Shi, X. B.; Du, M. S.; Yang, F.; Zheng, Y. J.; Zhang, Z.; Li, X. D.; Brown, D. E.; Li, J. *Science* **2013**, *339*, 1191.
- (117) Wang, K.; Weissmuller, J. *Adv. Mater.* **2013**, *25*, 1280.
- (118) Evans, A. G.; Hutchinson, J. W.; Fleck, N. A.; Ashby, M. F.; Wadley, H. N. G. *Prog. Mater. Sci.* **2001**, *46*, 309.
- (119) Gibson, L. J.; Ashby, M. F. *Cellular Solids: Structure and Properties*; 2nd ed.; Cambridge University Press: Cambridge, 1999.
- (120) Deshpande, V. S.; Fleck, N. A.; Ashby, M. F. *J. Mech. Phys. Solids* **2001**, *49*, 1747.
- (121) Wadley, H. N. G.; Fleck, N. A.; Evans, A. G. *Composites Science and Technology* **2003**, *63*, 2331.
- (122) Brittain, S. T.; Sugimura, Y.; Schueller, O. J. A.; Evans, A. G.; Whitesides, G. M. *Journal of Microelectromechanical Systems* **2001**, *10*, 113.
- (123) Schaedler, T. A.; Jacobsen, A. J.; Torrents, A.; Sorensen, A. E.; Lian, J.; Greer, J. R.; Valdevit, L.; Carter, W. B. *Science* **2011**, *334*, 962.
- (124) Rys, J.; Valdevit, L.; Schaedler, T. A.; Jacobsen, A. J.; Carter, W. B.; Greer, J. R. *Advanced Engineering Materials* **2014**.
- (125) Bauer, J.; Hengsbach, S.; Tesari, I.; Schwaiger, R.; Kraft, O. *Proc. Natl. Acad. Sci. U. S. A.* **2014**, *111*, 2453.
- (126) Jang, D. C.; Meza, L. R.; Greer, F.; Greer, J. R. *Nat Mater* **2013**, *12*, 893.
- (127) Montemayor, L. C.; Meza, L. R.; Greer, J. R. *Advanced Engineering Materials* **2013**.
- (128) Gansel, J. K.; Thiel, M.; Rill, M. S.; Decker, M.; Bade, K.; Saile, V.; von Freymann, G.; Linden, S.; Wegener, M. *Science* **2009**, *325*, 1513.
- (129) Kiener, D.; Grosinger, W.; Dehm, G.; Pippan, R. *Acta Mater.* **2008**, *56*, 580.
- (130) Tabor, D. *Review of Physics in Technology* **1970**, *1*, 145.
- (131) Aitken, Z. H.; Jang, D. C.; Weinberger, C. R.; Greer, J. R. *Small* **2014**, *10*, 100.
- (132) Jennings, A. T.; Greer, J. R. *Philosophical Magazine* **2011**, *91*, 1108.

- (133) Kiener, D.; Motz, C.; Schoberl, T.; Jenko, M.; Dehm, G. *Advanced Engineering Materials* **2006**, *8*, 1119.
- (134) Blewitt, T. H. *Physical Review* **1953**, *91*, 1115.
- (135) Ebrahimi, F.; Bourne, G. R.; Kelly, M. S.; Matthews, T. E. *Nanostructured Materials* **1999**, *11*, 343.
- (136) Tappan, B. C.; Steiner, S. A.; Luther, E. P. *Angew. Chem.-Int. Edit.* **2010**, *49*, 4544.
- (137) Peng, Z. Q.; Freunberger, S. A.; Chen, Y. H.; Bruce, P. G. *Science* **2012**, *337*, 563.
- (138) Braun, P. V. *Chem Mater* **2014**, *26*, 277.
- (139) Kasavajjula, U.; Wang, C. S.; Appleby, A. J. *Journal of Power Sources* **2007**, *163*, 1003.
- (140) Gao, Y. F.; Cho, M.; Zhou, M. *Journal of Mechanical Science and Technology* **2013**, *27*, 1205.
- (141) Maranchi, J. P.; Hepp, A. F.; Evans, A. G.; Nuhfer, N. T.; Kumta, P. N. *J. Electrochem. Soc.* **2006**, *153*, A1246.
- (142) Pharr, M.; Suo, Z. G.; Vlassak, J. J. *Nano Lett* **2013**, *13*, 5570.
- (143) Graetz, J.; Ahn, C. C.; Yazami, R.; Fultz, B. *Electrochemical and Solid State Letters* **2003**, *6*, A194.
- (144) Lee, S. W.; McDowell, M. T.; Berla, L. A.; Nix, W. D.; Cui, Y. *Proc. Natl. Acad. Sci. U. S. A.* **2012**, *109*, 4080.
- (145) Zhang, H. G.; Braun, P. V. *Nano Lett* **2012**, *12*, 2778.
- (146) Magasinski, A.; Dixon, P.; Hertzberg, B.; Kvit, A.; Ayala, J.; Yushin, G. *Nat Mater* **2010**, *9*, 353.
- (147) Liu, N.; Wu, H.; McDowell, M. T.; Yao, Y.; Wang, C. M.; Cui, Y. *Nano Lett* **2012**, *12*, 3315.
- (148) Lakes, R. *Science* **1987**, *235*, 1038.
- (149) Steeves, C. A.; Lucato, S.; He, M.; Antinucci, E.; Hutchinson, J. W.; Evans, A. G. *J. Mech. Phys. Solids* **2007**, *55*, 1803.
- (150) Huang, J. Y.; Zhong, L.; Wang, C. M.; Sullivan, J. P.; Xu, W.; Zhang, L. Q.; Mao, S. X.; Hudak, N. S.; Liu, X. H.; Subramanian, A.; Fan, H. Y.; Qi, L. A.; Kushima, A.; Li, J. *Science* **2010**, *330*, 1515.
- (151) Liu, X. H.; Zheng, H.; Zhong, L.; Huan, S.; Karki, K.; Zhang, L. Q.; Liu, Y.; Kushima, A.; Liang, W. T.; Wang, J. W.; Cho, J. H.; Epstein, E.; Dayeh, S. A.; Picraux, S. T.; Zhu, T.; Li, J.; Sullivan, J. P.; Cumings, J.; Wang, C. S.; Mao, S. X.; Ye, Z. Z.; Zhang, S. L.; Huang, J. Y. *Nano Lett* **2011**, *11*, 3312.
- (152) McDowell, M. T.; Ryu, I.; Lee, S. W.; Wang, C. M.; Nix, W. D.; Cui, Y. *Adv. Mater.* **2012**, *24*, 6034.
- (153) McDowell, M. T.; Lee, S. W.; Harris, J. T.; Korgel, B. A.; Wang, C. M.; Nix, W. D.; Cui, Y. *Nano Lett* **2013**, *13*, 758.
- (154) Guerfi, A.; Charest, P.; Dontigny, M.; Trottier, J.; Lagace, M.; Hovington, P.; Vijh, A.; Zaghbi, K. *Journal of Power Sources* **2011**, *196*, 5667.
- (155) Zaghbi, K.; Armand, M.; Gauthier, M. *J. Electrochem. Soc.* **1998**, *145*, 3135.
- (156) Dolle, M.; Sannier, L.; Beaudoin, B.; Trentin, M.; Tarascon, J. M. *Electrochemical and Solid State Letters* **2002**, *5*, A286.
- (157) Santhanagopalan, D.; Qian, D.; McGilvray, T.; Wang, Z. Y.; Wang, F.; Camino, F.; Graetz, J.; Dudney, N.; Meng, Y. S. *Journal of Physical Chemistry Letters* **2014**, *5*, 298.
- (158) Green, M.; Fielder, E.; Scrosati, B.; Wachtler, M.; Serra Moreno, J. *Electrochemical and Solid State Letters* **2003**, *6*, A75.

